Manufacturing and Analysis of Wave-shaped Wires for Stress-reduced Interconnection of Silicon Solar Cells

Dissertation

zur Erlangung des Grades
des Doktors der Ingenieurwissenschaften (Dr.-Ing.)
der Naturwissenschaftlich-Technischen Fakultät
der Universität des Saarlandes

vorgelegt von

Li Carlos Rendler

Saarbrücken

2021

Tag des Kolloquiums:	15. März 2022
Dekan:	Prof. Dr. Jörn E. Walter
Berichterstatter:	Prof. Dr.-Ing. Steffen Wiese
	Prof. Dr.-Ing. Matthias Nienhaus
	Prof. Dr.-Ing. Bernhard Wunderle
Akad. Mitglied:	Dr.-Ing. Christian Bur
Vorsitz:	Prof. Dr.-Ing. Stefan Diebels

Kurzbeschreibung

Der Standardprozess für die Verschaltung von Siliziumsolarzellen ist Löten. Unterschiedliche thermische Ausdehnungskoeffizienten der eingesetzten Materialien erzeugen thermomechanische Spannungen nach dem Lötvorgang. Diese können zu Defekten führen, welche die Ausgangsleistung photovoltaischer Module verringern.

In dieser Arbeit wurden thermomechanische Spannungen aufgrund des Lötvorgangs mittels der Finite Elemente Methode analysiert. Die Ergebnisse ermöglichen eine Optimierung des Kontaktmetallisierungslayouts von Solarzellen, sodass Spannungsmaxima reduziert werden können. Außerdem beeinflussen die mechanischen Eigenschaften von zur Verschaltung eingesetzten Kupferzellverbindern thermomechanische Spannungen wesentlich. Deshalb wurden gewellte Drähte eingeführt und deren physikalische Eigenschaften analysiert. Mittels neu entwickelter Umformmethoden wurde eine Reduktion der Pseudo-Dehngrenze von bis zu $-88,5\%$ erreicht. Dies zeigt das Potential gewellter Drähte thermomechanische Spannungen deutlich zu reduzieren. Berechnungen zeigen außerdem, dass durch eine Verschaltung mit gewellten Drähten eine Erhöhung der Modulleistung um bis zu 2,1% möglich ist. Zudem wird das Löten auf Kleinstkontakten ermöglicht und die Biegeverformung bei einseitiger Verschaltung von hocheffizienten Rückkontaktsolarzellen maßgeblich reduziert. Thermische Zyklentests zeigen eine Leistungsdegradation kleiner -3% nach 200 Zyklen und damit vergleichbare Ergebnisse wie Standardverschaltungsansätze.

Abstract

Soldering of copper interconnectors is the standard process for the interconnection of silicon solar cells. Different coefficients of thermal expansion of the used materials cause thermomechanical stress after the soldering process. Thermomechanical stress may induce defects that result in power degradation of photovoltaic modules.

In this work, thermomechanical stress caused by the soldering process is examined by finite element analyses. The results reveal how to optimize the metallization layout for reduced stress maxima. In addition, the mechanical properties of copper ribbons or wires used for the interconnection significantly affect thermomechanical stress. For this reason, wave-shaped wires were introduced and their physical properties were analyzed. Using newly developed reshaping methods a pseudo yield limit reduced by up to -88.5% is possible. This indicates the potential of wave-shaped wires for significant stress reduction. Simulations show a maximum power increase of 2.1% when interconnecting solar cells with wave-shaped wires. In addition, wave-shaped wires enable soldering on smallest contacts and the bending deformation of high-efficiency back-contact solar cells is significantly reduced. Furthermore, temperature cycling shows a power degradation below -3% after 200 cycles, which is comparable to standard interconnection approaches.

Danksagung

Diese Arbeit ist in der Abteilung Modultechnologie am Fraunhofer Institut für Solare Energiesysteme ISE entstanden und wurde von Prof. Dr.-Ing Steffen Wiese vom Lehrstuhl für Mikrointegration und Zuverlässigkeit an der Universität des Saarlands betreut. Mein besonderer Dank gilt dir Steffen, für die Zeit, die du dir genommen hast, mich bei diesem Vorhaben bestmöglich zu unterstützen. Ich möchte außerdem den beiden Gutachtern Prof. Dr.-Ing. Matthias Nienhaus und Prof. Dr.-Ing. Bernhard Wunderle meinen Dank aussprechen.

Bei der Bearbeitung der Themen waren mir viele Menschen eine große Hilfe. Besonders danken möchte ich Dr. Ulrich Eitner, der mich immer sehr unterstützt hat, besonders in schwierigeren Arbeitsphasen. Für die weitere Unterstützung danke ich Dr. Achim Kraft, Dr. Holger Neuhaus sowie allen Kollegen und ehemalige Kollegen am Fraunhofer ISE, die mich ein Stück auf meinem Weg begleitet und die wesentlich zum erfolgreichen Gelingen beigetragen haben.

Herzlicher Dank gebührt auch meiner Familie, allen voran meinen Eltern Karin und Olaf, die mich mein ganzes Leben hindurch gefördert und bestmöglich unterstützt haben. Außerdem danke ich meinen Geschwistern Hannah und Nicolas, die für mich auch sehr gute Freunde sind. Meiner Partnerin Eva möchte ich ganz besonders danken für ihr Verständnis und die großartige Unterstützung, die ich von ihr bekommen habe seit wir uns kennen. Weiterhin geht ein Dank an alle meine Freunde, die mein Leben um so viele wunderbaren Aspekte reicher machen.

Freiburg im Breisgau, 2022

Li Carlos Rendler

Contents

Abbreviations

3BB	three busbar
5BB	five busbar
aTC	accelerated temperature cycling
BB	busbar
BC	back contact
CAD	computer aided design
CTE	coefficient of thermal expansion
CTM	cell-to-module
ECA	electrically conductive adhesive
EL	electroluminescence
EVA	ethylen-vinyl acetate
EW	effective width
FE	finite element
FEM	finite element method
Fraunhofer ISE	Fraunhofer Institute for Solar Energy Systems
IBC	interdigitated back contact
IEA	International Energy Agency
IEC	International Electrotechnical Comission
IMEC	Interuniversity Microelectronics Centre
IR	infrared
ISC Konstanz	International Solar Energy Research Center Konstanz
IV	current and voltage
MBB	Multi Busbar
MWT	metal wrap through

NASA	National Aeronautics and Space Administration
PV	photovoltaic
RoHS	Restriction of the use of certain hazardous substances in electrical and electronic equipment
SEM	scanning electron microscope
SHJ	silicon heterojunction
STC	standard test conditions
SWCT	SmartWire Connection Technology
TC	temperature cycling

Nomenclature

A_1	cross-sectional area of a wave-shaped wire
ε	strain
$\varepsilon_{\mathrm{Eng}}$	engineering strain
$\varepsilon_{\mathrm{True}}$	true strain
η	photo conversion efficiency
f_{D}	relative change of the electrical resistance induced by damaging due to reshaping
FF	fill factor
f_{L}	relative change of the length due to reshaping
$F_{\mathrm{p0.2}}$	0.2% yield force
f_{W}	relative change of the electrical resistance due to reshaping
I_{MPP}	current at maximum power point
I_{SC}	short-circuit current
l_1	length between two markers of an initially straight wire
l_2	length between two markers of a wave-shaped wire
P_{MPP}	power at the maximum power point
R_1	electrical resistance between two markers of an initially straight wire
R_2	electrical resistance between two markers of a wave-shaped wire
ρ	specific electrical resistance
R_{Straight}	electrical resistance of a straight wire
R_{Wave}	electrical resistance of a wave-shaped wire
σ_{I}	first principal stress

σ_{Eng}	engineering stress
σ_{True}	true stress
σ_{XX}	transversal stress
σ_{YY}	longitudinal stress
V_{OC}	open-circuit voltage
E	Young's modulus

1 Introduction

1.1 Motivation and background

The main objective of this work was the reduction of thermomechanical stress in photovoltaic (PV) modules caused by the interconnection process of solar cells. First, thermomechanical stress in solar cells was analyzed by simulations and experiments. Second, a novel interconnection approach based on compliant wave-shaped wire interconnectors was developed and analyzed in detail.

The Paris Climate Agreement within the United Nations Framework Convention on Climate Change aims to limit the increase of the average temperature on earth below 2 °C above the pre-industrial level [1, 2]. The use of fossil fuels has been causing emission of large amounts of greenhouse gases, which are seen as the main reason for global warming [3, 4]. According to the International Energy Agency (IEA), about 65% of the global emission of greenhouse gases is dissipated due to the production and use of energy [5]. The contribution of renewable energy sources to the global energy consumption has been constantly raised over the past decades [6]. However, one renewable energy source can not be sufficient to satisfy world's energy needs. A mixture of different energy sources, such as wind, water, biomass, solar power, et cetera, is required to fulfill the constantly rising power demands [5, 7–9]. PV energy is one part of a mixture of different renewable energies sources, and its share has been increased substantially in the last years [6, 10]. According to Philipps *et al.*, the compound annual growth rate of worldwide photovoltaic installations was 36.8% between 2010 and 2018 [11].

Over the past decades, costs for PV systems were constantly reduced aiming to compete with other energy sources. Costs are mainly given by the investment costs for the PV system, the systems efficiency, and the long-term stability. In 2018, the PV modules accounted for approximately 50% of the total costs of typical PV systems [12]. PV module costs are constantly decreasing, over the last years mainly driven by reduced silicon wafer costs and by increasing the amount of automation in solar cell and PV module production. In addition, a shift to Asian

countries and a considerable increase of the worldwide solar cell and PV module production capacity further reduced the costs. Furthermore, the efficiency of silicon solar cells and PV modules has been increased over the last years [13]. According to Philipps *et al.*, the average efficiency of commercial wafer-based PV modules has been increased from 12% to 17% between 2009 and 2019 [11]. Additionally, most PV module manufacturers extended the warranty times for their modules (typically less than -20% power degradation after 20 to 35 years operating time), which indicates a notable improvement of the long-term stability over the years.

In the manufacturing process of PV modules first defects may occur which significantly influences the long-term stability [14]. For example, different coefficients of thermal expansion (CTEs) of the involved materials cause thermomechanical stress when the temperature changes, which may cause initial defects [15, 16]. In addition, manufacturing processes or materials of PV modules are sometimes changed or modified to reduce costs or to increase efficiency. These process or material modifications may significantly impact the long-term stability of PV modules.

Especially during their lifetime, several factors cause degradation of PV modules [17, 18]. After the production process, a number of tests specified by the International Electrotechnical Comission (IEC) test standard for PV modules (IEC 61215) are currently conducted to check the quality of PV modules [19]. However, reliability testing in the laboratory, as well as field tests are necessary to examine the long-term stability for PV modules [20]. Standard tests include for example increased humidity, hail impact, mechanical loading, or temperature changes [21]. Mechanical stress caused by temperature changes, snow loads, wind loads, et cetera adds up to residual thermomechanical stress from the manufacturing process and is one major factor that causes defects in PV modules [22–24].

Comprehensive analyses with experiments and calculations targeting mechanical stress in PV modules were first performed by scientists of the National Aeronautics and Space Administration (NASA) in the seventies [25, 26]. To determine whether thermomechanical stress in a solar cell exceeds critical stress levels, simulations, for example finite element (FE) analyses, were performed in several studies. Eitner *et al.* focused on thermomechanical stress caused by the lamination process and temperature cycling [27]. Beinert *et al.* analyzed mechanical stress in the solar cells of framed,

as well as non-framed PV modules caused by mechanical loads [28, 29]. Other studies focused on the influence of interconnectors and their solder coating [30–37], mechanical properties [38–40], and the geometry [26, 41–44] on thermomechanical stress in silicon solar cells.

1.2 Research focus

Focus of this work was to reduce thermomechanical stress caused by the soldering step in the manufacturing process of PV modules. For this reason, thermomechanical stress was analyzed and several influence factors were determined by simulation and experiments. Key factors are the properties of the commonly screen-printed contact metallization [45], as well as of the usually copper-based and solder-coated interconnectors [16, 38]. The mechanical stability of the contact metallization is primarily influenced by the solar cell surface, the paste material composition, the screen-printing, and the contact firing process [46, 47]. However, an analysis of solar cell properties or the formation of the contact metallization were no objectives of this work. Nevertheless, it is important to mention that the layout of the contact metallization may significantly affect the long-term stability of the interface between wafer surface and metallization in PV modules. Hence, parameter variations were conducted to determine layout guidelines for the metallization of silicon solar cells. More importantly, the mechanical properties of the interconnectors influence the long-term stability of the interconnection between interconnector and silicon wafer [16, 48]. For this reason, as an alternative to standard ribbon or wire interconnectors, wave-shaped wires were introduced. Main goals of this work were the development and comparison of different manufacturing processes for wave-shaped wires, and to determine physical properties of wave-shaped wires with different geometrical characteristics. An additional intention was to find out whether wave-shaped wires enable soldering on very small contacts, which is a technological trend for the solar cell metallization to reduce material consumption, recombination losses, and shading losses. Furthermore, single side soldering of wave-shaped wires on back contact (BC) solar cells, which currently reach highest efficiencies [13, 49], was tested.

1.3 Structure of the work

In Chapter 2 the state of science and technology is described. Chapter 3 addresses the different reasons for thermomechanical stress in PV modules. The results of FE analyses help to gain a deeper understanding of thermomechanical stress in solar cells due to the interconnection process. The results reveal critical areas with stress maxima and deliver guidelines how to reduce thermomechanical stress in PV modules. In Chapter 4, as a new type of interconnector, wave-shaped wires are introduced, aiming to reduce thermomechanical stress significantly. Chapter 5 describes different manufacturing methods for wave-shaped wires. Furthermore, experiments indicate how the physical properties of round wires are affected by the wave-shaping process. Chapter 6 addresses the interconnection process for solar cells by wave-shaped wires. Semi-automatic soldering of wave-shaped wires on the finger grid of standard solar cells is analyzed. Furthermore, the results of pilot experiments targeting the interconnection of BC solar cells by wave-shaped wires are described. In Chapter 7 the calculation of the potential output power of PV modules including solar cells interconnected by soldering wave-shaped wires directly on the finger grid is analyzed. In Chapter 8 the findings are discussed and compared with the state of science and technology. In addition a brief outlook is given. Chapter 9 summarizes the major findings and results.

2 State of science and technology

2.1 Solar cells and photovoltaic modules

Most solar cells are made from silicon wafer material. There are other technologies such as thin film or organic PV, but this work focuses on silicon wafer based PV exclusively. Several process steps are required when manufacturing silicon solar cells, such as doping, etching, texturing, and formation of electrical contacts. Common solar cells consist of a pre-doped silicon wafer with a full area vertical pn-junction caused by doping of one surface. However, there are solar cell types that have pn-junctions on the rear side due to partial doping on the rear side.

The electrical contacts are commonly applied by screen-printing metallization paste and subsequent contact firing. The silver-based metallization paste material, its interface to the silicon wafer, and its layout are crucial for the interconnection of solar cells. Common monofacial silicon solar cells have contact fingers and busbars (BBs) on the front side, as well as contact pads and a full area aluminum metallization on the rear side. Bifacial solar cells are able to transform light from both sides and have a busbar contact layout on both sides. In the last years, solar cell manufacturers introduced different contact metallization designs to solar cell production to reduce costs by saving silver paste. Examples are tapered or segmented busbars [50–52], using rows of small pads instead of busbars [53, 54], or even omitting busbars or pad rows by directly connecting the finger grid [55, 56]. Figure 2.1 shows both sides of a typical (monofacial) silicon solar cell with a five busbar (5BB) layout on the front side and contact pads on the rear side. Figure 2.2 outlines the most common types of solar cells. Focus of this work are solar cells of the technologies highlighted in orange color.

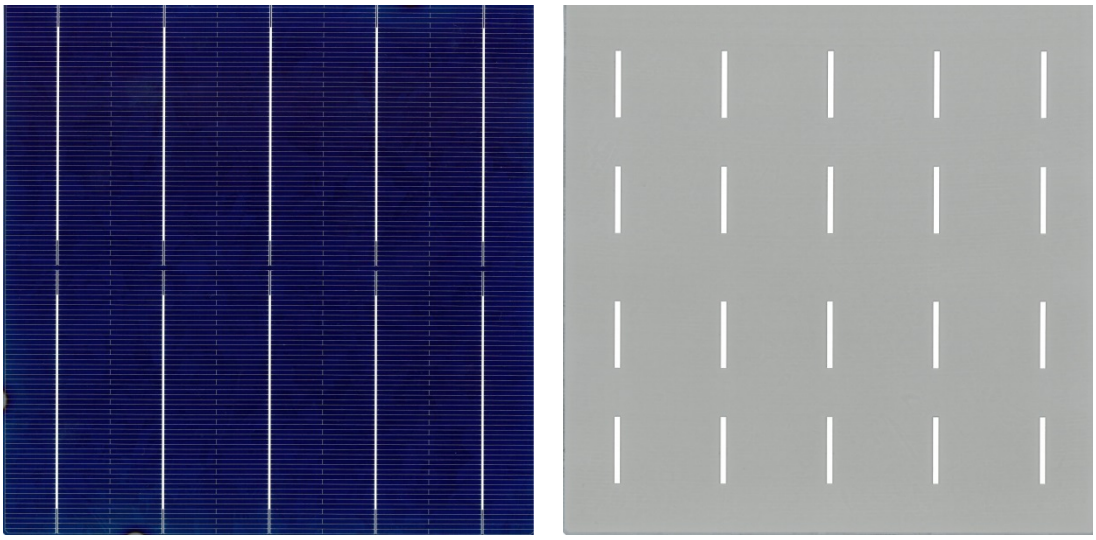

(a) (b)

Figure 2.1: (a) Front side with busbars and (b) rear side with contact pads of a typical 5BB solar cell (monofacial, size: 156 mm × 156 mm). The interruption in the middle of the busbar on the front side enables solar cell cutting resulting in half solar cells.

A PV module is a structural element which includes a number of interconnected solar cells that enable a direct transformation of sunlight into electrical energy [57]. In crystalline silicon photovoltaics, which nowadays has a market share of more than 90% [12, 58], a PV module includes a number of typically 60 or 72 solar cells, or 120 or 144 half solar cells respectively. There are two key process steps in PV module production. Figure 2.3 illustrates the major steps of the manufacturing process of PV modules (starting with solar cells).

After solar cell assessment and sorting, the first principal production step is the electrical (and mechanical) interconnection of the solar cells forming the so-called solar cell matrix. Most commonly, the solar cells are interconnected by copper based ribbons with a rectangular shape and a SnPb solder coating. Many PV module manufacturers use strings of half-cut solar cells delivering approximately half the current and double the voltage in order to reduce losses caused by the electrical resistance of the interconnection [59] and to increase the output power due to optical improvements. Figure 2.4 explains the most common interconnection technologies

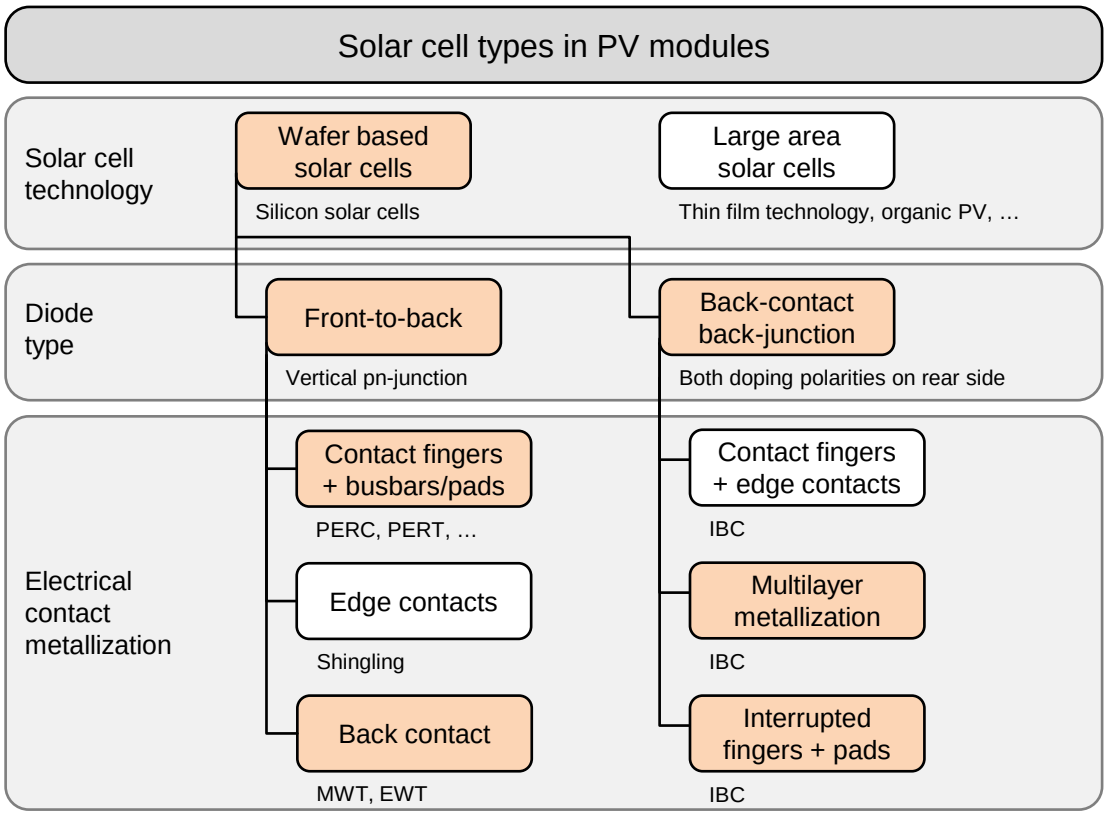

Figure 2.2: Different solar cell types categorized by the cell technology, the diode type, and the electrical contact metallization. Highlighted in orange color are the most important solar cell technologies for this work.

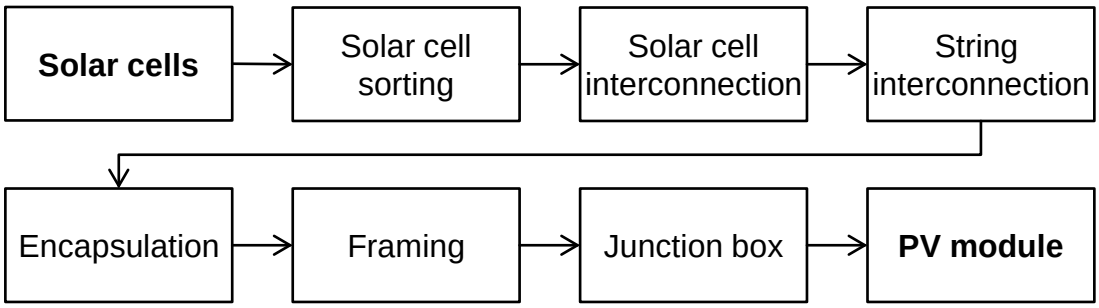

Figure 2.3: Main process steps in the manufacturing process of PV modules.

for silicon solar cells, categorized by the interconnector core material, its shape, the interconnection process (soldering or adhesive bonding), and the used solder alloy. Focus of this work is the interconnection of different types of solar cells (highlighted in Figure 2.2) by soldering copper based wire interconnectors with a round cross-section and a SnPb based solder coating, which is highlighted in orange color.

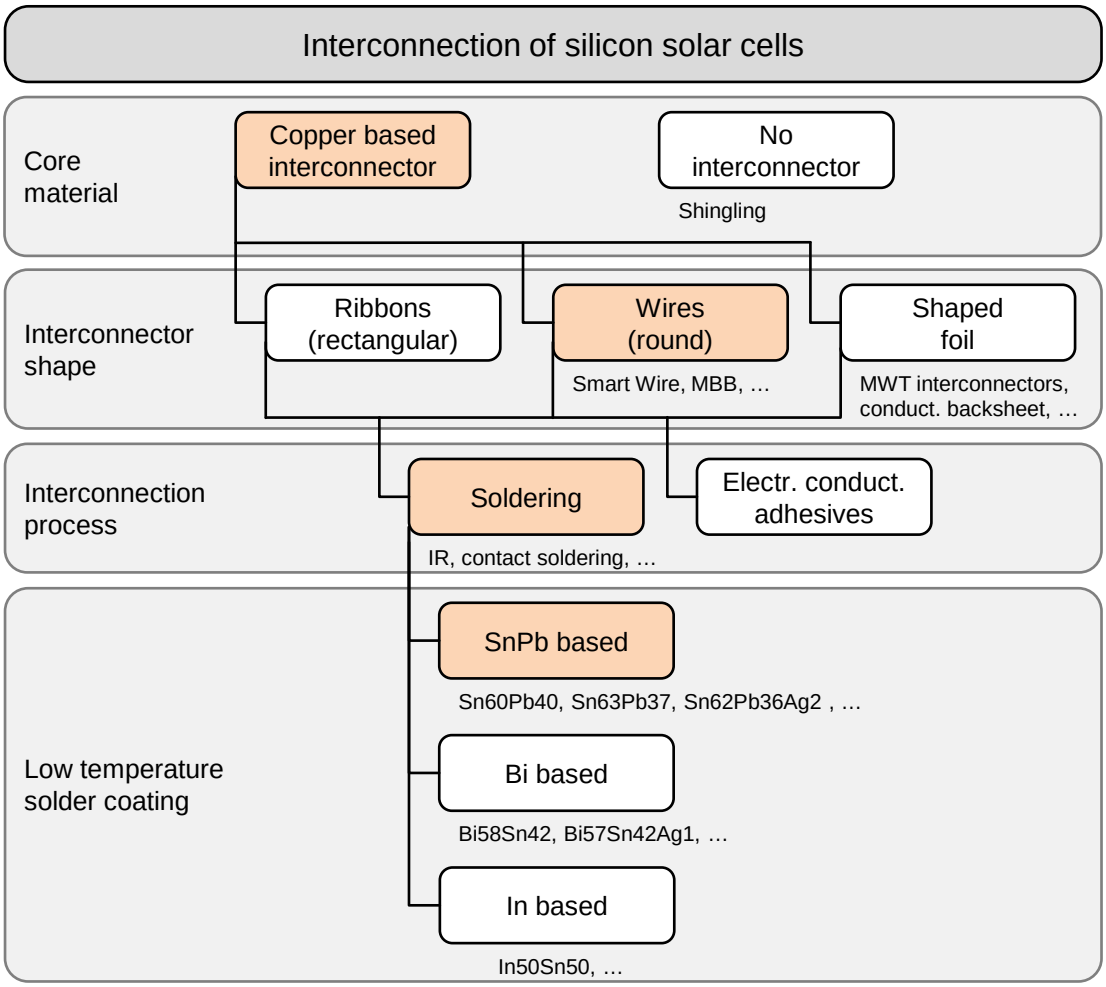

Figure 2.4: Different interconnection technologies for silicon solar cells, categorized by the interconnector material, its shape, the interconnection process, and the typical solder alloys. Highlighted in orange color are the most important technologies in this work.

After the interconnection process a solar cell matrix is encapsulated by lamination. A standard PV module has a glass pane on the front side and a polymer-based backsheet laminate or a second glass pane on the rear side. In between the glass panes, the solar cell matrix is embedded into a highly transparent polymer layer, in most cases ethylen-vinyl acetate (EVA) [60]. In the lamination process the PV module material stack is heated up and pressed together in a vacuum chamber. After a defined time at a specific temperature (for EVA approximately 7 to 15 minutes at about 150 °C) curing of the encapsulant by crosslinking of polymeric chains results in bonding of the materials. Pressing the material stack together in the vacuum chamber is performed to prevent cavities and solar cell cracking in the PV laminate. After lamination, a common PV module is equipped with an aluminum frame at the edges for stability and mounting, as well as with a junction box on the rear side for electrical connection. As a result, the solar cell matrix is protected against environmental influences to prevent degradation or breakdown. A schematic drawing of the assembly of a typical PV module is shown Figure 2.5.

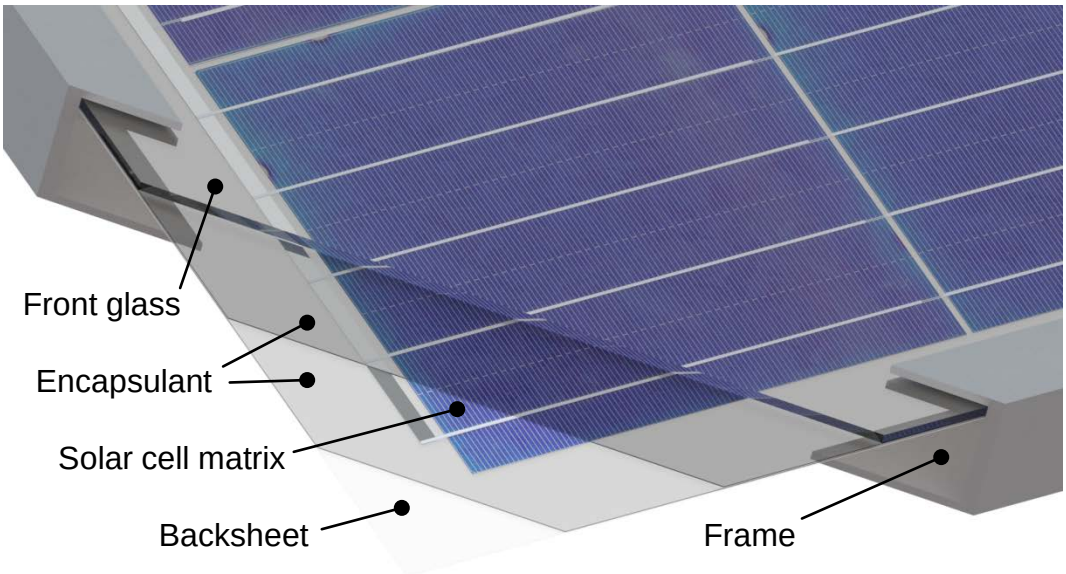

Figure 2.5: Common PV module assembly showing the front glass, the encapsulant, the solar cell matrix, the backsheet, as well as the frame.

2.2 Interconnection technologies for silicon solar cells

2.2.1 Common interconnection of solar cells

In the production process of PV modules solar cells are commonly interconnected with three to six ribbon interconnectors. Typically, interconnectors consisting of a copper core with a solder coating, have a rectangular cross-section, and are soldered on the busbars (front side) and contact pads (rear side) of a solar cell. For 5BB solar cells typical copper core cross-section dimensions are $0.9\,\mathrm{mm} \times 0.22\,\mathrm{mm}$. A number of solar cells connected in series, with interconnectors from the front side of one solar cell to the rear side of the next solar cell, forms a solar cell string.

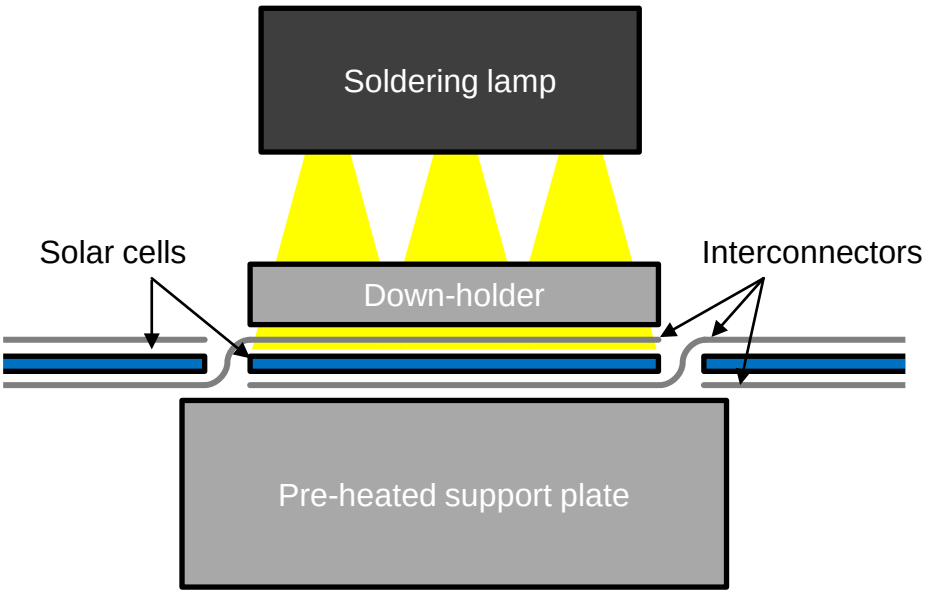

Figure 2.6: Typical setup for the interconnection of common silicon solar cells to manufacture solar cell strings by soldering using infrared (IR) lamps.

The interconnection is fully automated in a so-called stringing machine. During the soldering process solar cells and solder-coated interconnectors are heated up above the melting point of the solder alloy, in most cases Sn60Pb40 or Sn62Pb36Ag2, and the solder wets the contacts of the solar cells. In addition, the connection of the

solder alloy and the contact metallization is supported by diffusion processes at the interface leading to phase formation [61]. Nowadays, most stringing machines heat up the materials using infrared (IR) light. According to a report by Chunduri *et al.*, the market share of IR heating was approximately 58% for commercially available interconnection tools in 2017 [62]. In the following cool-down period, the solder solidifies and an electrical and mechanical connection of the solar cells is established. Subsequently, the strings are connected by cross-connectors forming the solar cell matrix. A schematic drawing of the interconnection of solar cells and a soldering setup for solar cell strings is shown by Figure 2.6.

2.2.2 Alternative interconnection technologies

2.2.2.1 Reasons

Alternative interconnection approaches based on thin wires instead of the common busbar- and ribbon-based technology were published. In the following, the most important alternatives to the common interconnection technology are concisely described. For some approaches there are already PV modules available on the market. Changing the interconnection is done for various reasons and potentially results in several advantages. One major reason is reducing costs of solar cells and PV modules, for example by using thinner wafers, by reducing the silver consumption of the contacts metallization when replacing busbars with small pads, et cetera. Such solar cell changes are only possible if the interconnection is also changed to minimize mechanical stress in order to avoid reliability issues. In addition, reducing (thermo-) mechanical stress levels in PV modules potentially leads to improved long-term stabilities in the field. Furthermore, alternative interconnection approaches potentially reduce electrical or optical losses resulting in improved photo conversion efficiencies (η) of PV modules.

2.2.2.2 Wire interconnection

There are different interconnection technologies available on the market that use thin wires instead of ribbons for the interconnection of silicon solar cells. One possibility is to solder a number of solder-coated round copper wires on the contact pads of a

silicon solar cell [53, 54]. Examples are the Multi Busbar (MBB) concept proposed by Gebr. SCHMID GmbH and the adapted CELLO-technology by LG Electronics, which are used in the mass production of PV modules [63]. Figure 2.7 shows both sides of an exemplary MBB solar cell with 15 pad rows on both sides. Another possibility is the SmartWire Connection Technology (SWCT), which uses a number of copper wires embedded in a polymer matrix and coated with low-melting (mostly indium- or bismuth-based) solder. This enables a combined soldering and lamination process, as well as the interconnection of solar cells without pads or busbars [56] and solar cells that are damaged by high temperatures, for example silicon heterojunction (SHJ) solar cells [64–66]. The SWCT, which was introduced by Day4 Energy in 2002 [55, 67], is now distributed by Meyer Burger Technology AG. Both wire-based concepts show various advantages; a reduced silver consumption due to an adapted metallization layout, increased module efficiencies caused by a lower series resistance, as well as optical improvements due to the use of round wire interconnectors [68, 69]. Moreover, the wire redundancy and the mechanical long-term stability of wire-based concepts potentially improve the module reliability [39, 70].

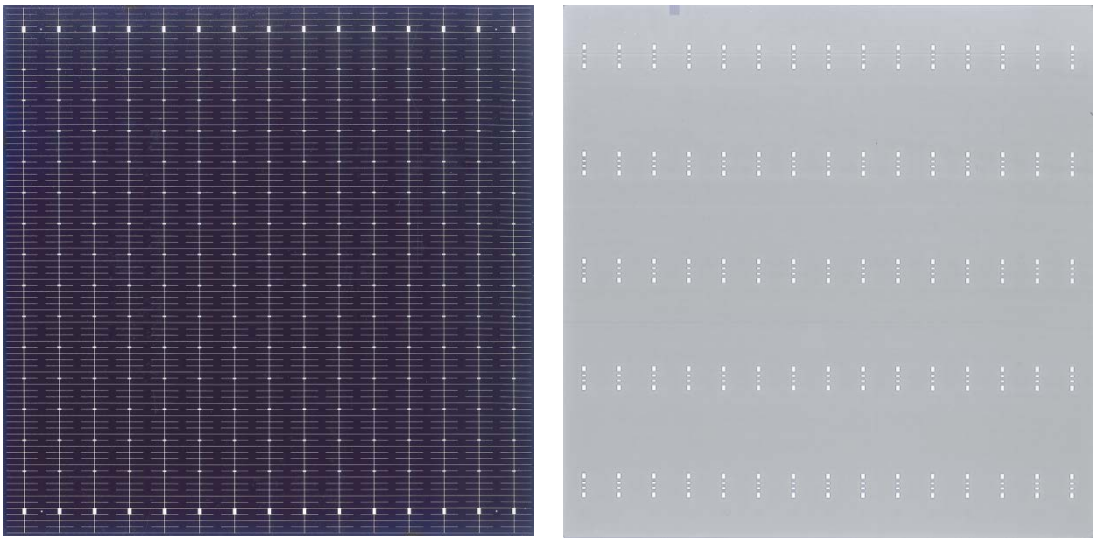

(a) (b)

Figure 2.7: (a) Front and (b) rear side of a typical MBB solar cell with 15 contact pad rows on both sides (monofacial, size: 156 mm × 156 mm).

2.2.2.3 Connecting the finger grid of solar cells

Omitting silver busbars or contact pads by soldering directly on the front finger grid of a silicon solar cell is challenging, but allows a maximum reduction of the amount of silver-based metallization paste. The typical width of screen-printed contact fingers is between 35 and 70 µm and the grid fingers usually fail at low stress levels [71, 72]. For this reason it is not possible to use standard ribbon or wire interconnectors to solder directly on the finger grid. Figure 2.8 shows an exemplary image of detachment of straight wire interconnectors after soldering on the finger grid.

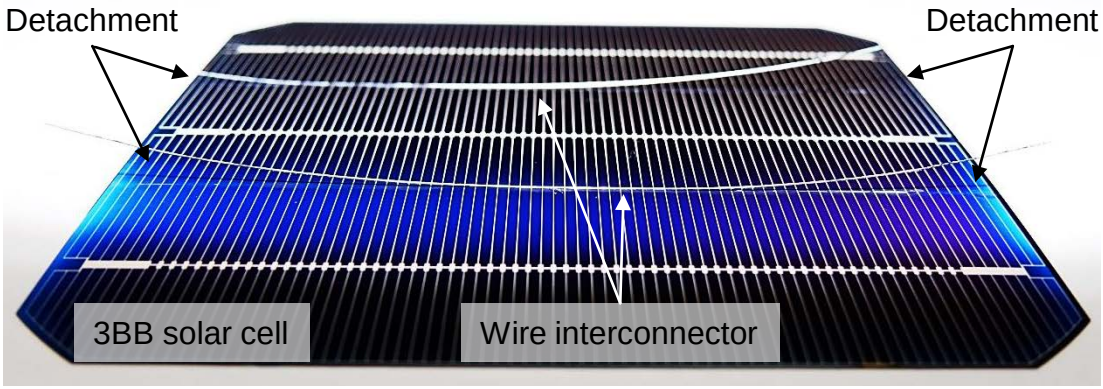

Figure 2.8: Immediate detachment of straight wire interconnectors after soldering directly on the finger grid between the busbars of a silicon solar cell (size: 156 mm × 156 mm).

However, it has been shown that contacting the finger grid is possible with selected electrically conductive adhesives (ECAs) [73, 74] or SmartWire foil [55, 56, 75]. The SWCT is concisely described in Section 2.2.2.2 while Figure 2.9 shows how to interconnect solar cells without pads or busbars by the polymer laminate with embedded wire interconnectors. In a SmartWire foil the thin wires are attached to the carrier foil which presumably reduces thermomechanical stress in the interconnections. Furthermore, the large number of wires shortens current paths and even with single interconnection failures due to thermomechanical stress the efficiency is not significantly reduced because of the high redundancy.

Figure 2.10 (a) shows an ECA that enables connecting a solar cell without contact pads or busbars. In addition, Figure 2.10 (b) shows a cross-section of an interconnection

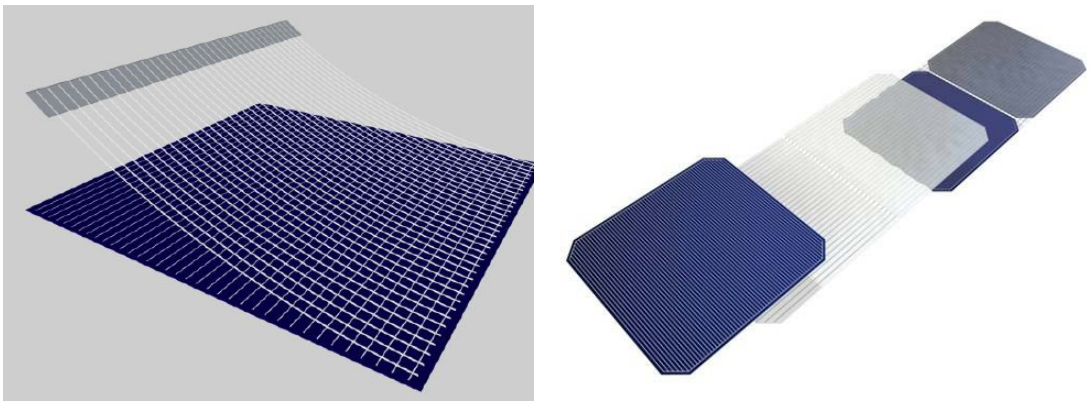

(a) (b)

Figure 2.9: Interconnection of solar cells without busbars or pads using the SWCT by Meyer Burger: (a) one solar cell with a SmartWire foil for the front side and (b) three solar cells that will be interconnected with the SWCT [56, 75].

and how the ECA connects the interconnector and one contact finger on a solar cells surface [74]. Using an ECA, consisting of silver particles in a soft polymer matrix that yields for low mechanical stress levels, reduces thermomechanical stress and therefore enables connecting the finger grid of a solar cell without substantial defects due to the CTE mismatch of copper and silicon. In this work, an important question is whether wire interconnectors with an adapted shape enable direct soldering on the finger grid of silicon solar cells without requiring additional polymer foils or ECA.

2.2.3 Back contact solar cells

The interconnection of BC solar cells is completely different to the front-to-back interconnection of solar cells schematically shown in Figure 2.6. A schematic drawing of a typical interconnection setup for BC solar cells is shown by Figure 2.11. The interconnection of BC solar cells can be challenging because the contacts of both polarities are located on the rear side [30, 76, 77]. This increases thermomechanical stress after soldering and causes significant deformation of the solar cells due to the CTE mismatch of copper and silicon.

The market share of BC solar cells, such as metal wrap through (MWT) or interdigitated back contact (IBC) solar cells, is expected to rise continuously, as this

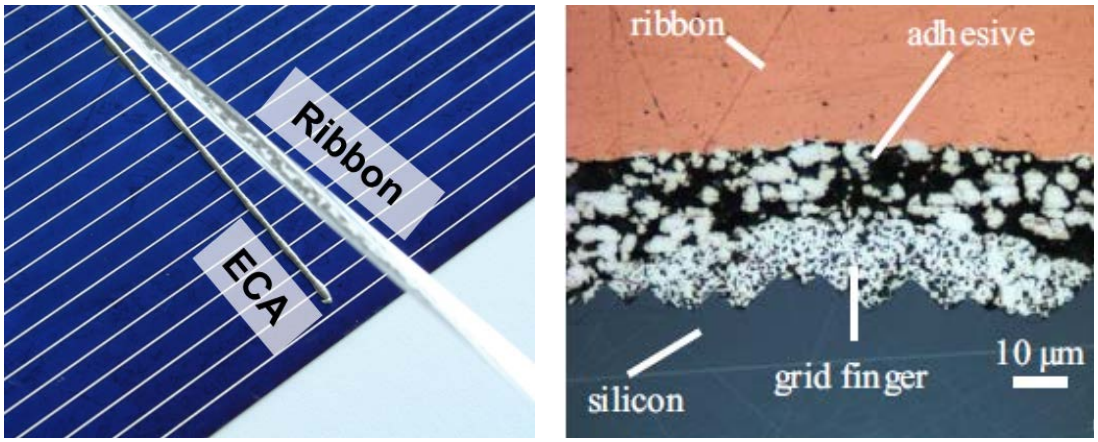

(a) (b)

Figure 2.10: Interconnection of a solar cell without contact pads or busbars by an ECA: (a) top view on a solar cell surface and (b) microscopic cross-section that shows an interconnection that connects an interconnector with a contact finger on the solar cell surface [74].

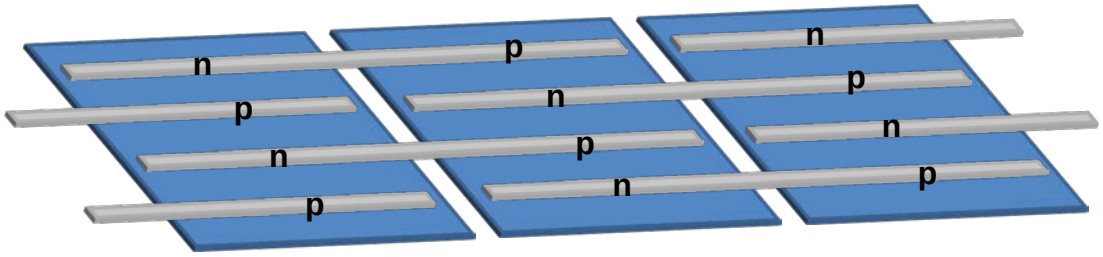

Figure 2.11: Rear side interconnection topology for BC solar cells showing interconnectors connecting one polarity of a solar cell with the opposite polarity contacts of an adjacent solar cell. Number and geometry of interconnectors depend on the contact design and should be optimized for a certain type of BC solar cell.

specific cell architecture reaches photo conversion efficiencies above 26%, which are currently the highest efficiencies for silicon-based mono-junction solar cells [13, 49]. Figure 2.12 shows the rear side of an MWT solar cell (developed and manufactured at Fraunhofer Institute for Solar Energy Systems (Fraunhofer ISE)), and a typical IBC solar cell (developed and manufactured at International Solar Energy Research Center Konstanz (ISC Konstanz)) [78].

(a) (b)

Figure 2.12: Rear sides of BC solar cells (size: 156 mm × 156 mm): (a) an exemplary MWT solar cell (developed and manufactured at Fraunhofer ISE) and (b) a typical IBC solar cell (developed and manufactured at ISC Konstanz) [78].

In order to reduce thermomechanical stress or solar cell deformation, solar cells with a smaller size can be used; for example half cells or solar cells with an edge length of 125 mm, instead of the current standard of 156.75 mm or even larger wafer sizes. Furthermore, thermomechanical stress can be reduced by using edge-to-edge interconnectors combined with a comparably thick metallization layer on the rear side. An example for this approach is the solar cell and PV module technology of Sunpower Corporation [79].

Another approach to interconnect BC solar cells is based on a conductive copper backsheet on the rear side interconnecting the solar cells that are connected to the structured backsheet by an ECA [80–82]. A schematic drawing of the interconnection of BC solar cells based on a structured copper backsheet is shown by Figure 2.13.

When using copper-based interconnectors (ribbons or wires) soldered on the contacts of BC solar cells instead of edge-interconnectors or conductive backsheets combined with an ECA there is no need for thick metallization layers or structured copper backsheets to achieve acceptable series resistances. This potentially reduces the costs of PV modules with BC solar cells significantly. The interconnection of BC solar cells

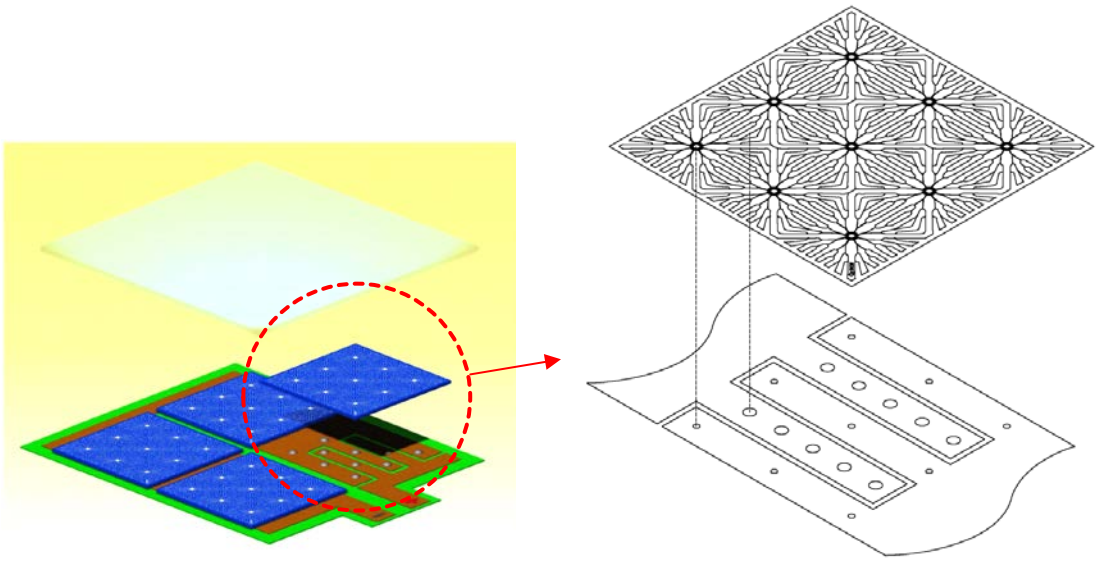

Figure 2.13: Interconnection of BC solar cells using a structured copper backsheet [80, 81].

was investigated at Fraunhofer ISE and described in detail by Hendrichs *et al.* [77]. Three solar cell designs with different contact layouts, one for the interconnection with ribbons (Group 1) and two for wire interconnection (Group 2 and 3), are shown in Figure 2.14. Further development on the interconnection of BC solar cells was published by Spribille *et al.* in 2019 [83].

Another approach to contact BC solar cells with wires that are embedded into a glass fiber fabric was developed at Interuniversity Microelectronics Centre (IMEC). This concept was introduced by Borgers *et al.* and is shown in Figure 2.15 [84]. The wire interconnectors can also be integrated into a polymer mesh, as done by Sefar AG [85].

For each of the described technologies, the interconnectors are only soldered onto one side of BC solar cells. For this reason thermomechanical stress caused by the mismatch of CTEs results in a deformation of the solar cells, in the following referred to as bowing. Modifications of the geometry or the physical properties of interconnectors can be applied to reduce thermomechanical stress and bowing of BC solar cells.

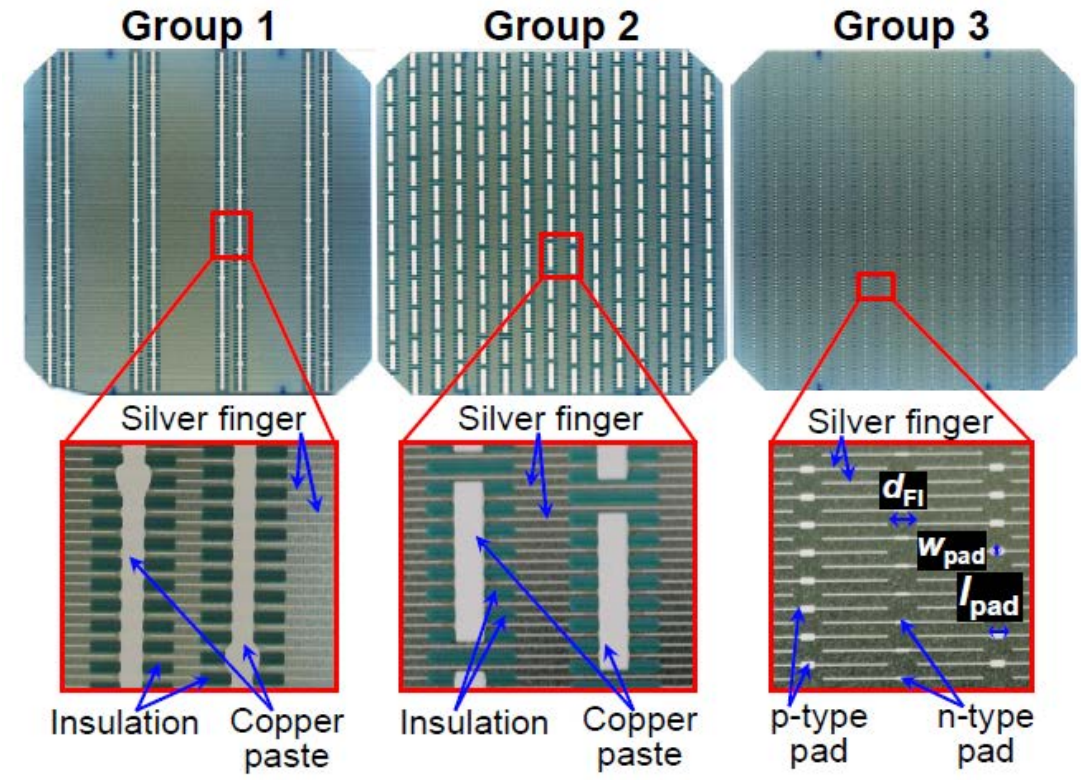

Figure 2.14: Contact design of BC solar cells (size: 156 mm×156 mm) for the interconnection with ribbons (Group 1) and wires (Group 2 and 3) developed at Fraunhofer ISE by Hendrichs *et al.* [77].

2.3 Mechanical stress in PV modules

2.3.1 Reasons for mechanical stress

A PV module and the interconnections that connect the solar cells consist of various materials. On the surface of common silicon solar cells there is a silver-based contact metallization. The contact metallization is connected by a solder alloy, typically Sn60Pb40, which is attached to the copper core of the interconnectors. In the soldering process the materials are heated up and the solder alloy melts. Subsequently, a cool-down period follows and the solder alloy solidifies. During cooling-down to room temperature mainly the significant mismatch of the CTEs of copper and silicon causes thermomechanical stress. Table 2.1 shows the CTEs of

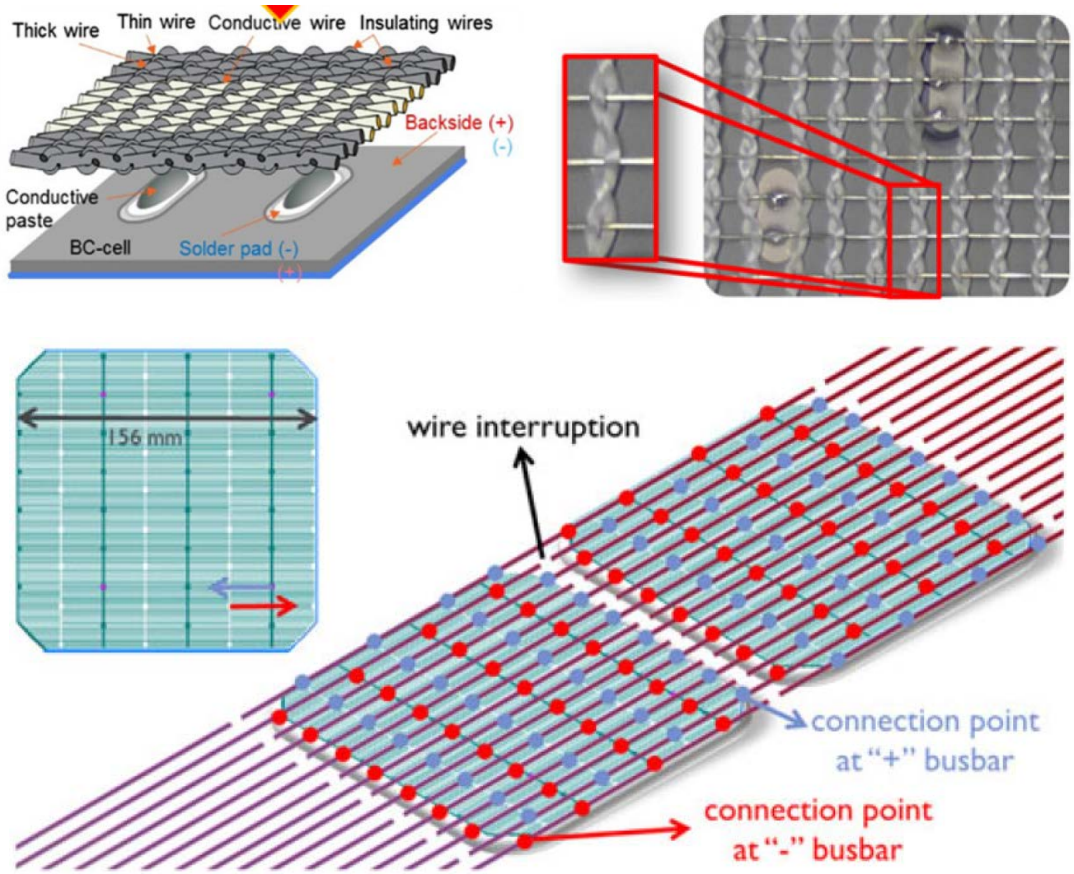

Figure 2.15: Schematic drawings of the interconnection setup, as well as a photograph of a glass fiber fabric with copper wires used for the interconnection of BC solar cells developed at IMEC by Borgers *et al.* [84].

common PV modules materials at room temperature. Figure 2.16 shows in principle how the copper interconnectors and the silicon solar cells in a PV module contract when the temperature decreases below the solidus temperature of the used solder alloy.

Typically, silicon solar cells are connected on both sides. Besides different metallization layouts on the front and rear side the solar cells interconnection setup is mostly symmetrical. For this reason, thermomechanical stress after the soldering process does not result in a significant bending deformation of solar cells connected on both sides, hence the induced stress is not directly visible. Nevertheless, small deformations can be caused by non-homogeneous temperature distribution in the

Table 2.1: CTEs of common materials of a PV module.

Material	**CTE** $[10^{-6} \cdot K^{1}]$
Glass [28]	9.0
Encapsulant (EVA) [27]	270
Copper [86]	17.0
Solder (Sn62Pb26Ag2) [30]	23.9
Silver metallization [46]	10.4
Silicon [87]	2.6
Aluminum metallization [46]	15.9
Backsheet [88]	50.4

Figure 2.16: Illustration of the contraction of copper interconnectors and silicon solar cells when the temperature decreases below the solidus temperature of the solder alloy (vertical deformations are neglected).

soldering and cool-down step. However, the deformation of solar cells, or solar cell sections, connected by interconnectors on one side can be analyzed as an indicator for the magnitude of thermomechanical stress due to the CTE mismatch after the soldering process [40]. Figure 2.17 shows two examples for the deformation of solar cells connected on only one side; a solar cell section (laser-cut, size: 78 mm × 10 mm)

connected by one wire interconnector, as well as a full solar cell connected by three ribbon interconnectors on busbars.

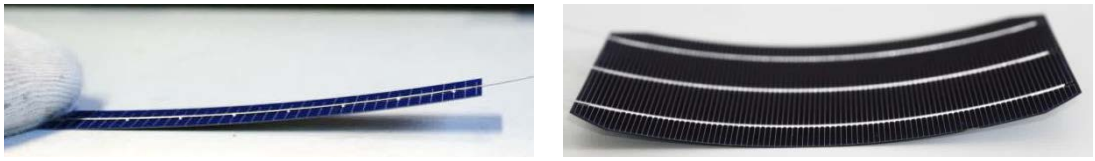

(a) (b)

Figure 2.17: Deformation of (a) a solar cell section (laser-cut, size: 78 mm × 10 mm) connected by a copper wire and (b) of a silicon solar cell (size: 156 mm × 156 mm) connected by three ribbon interconnectors on one side.

In addition to the residual stress, caused by the interconnection of solar cells, the encapsulation process causes thermomechanical stress. Table 2.1 shows the CTEs of encapsulant (EVA), front glass, and backsheet. Furthermore, a PV module undergoes several temperature changes during its lifetime (e.g. day-night, or summer-winter changes) that cause additional thermomechanical stress. Moreover, mechanical stress due to snow or wind loads may increase the stress levels even further. Figure 2.18 shows PV modules with significant snow loads, as well as a photograph of a PV module in a mechanical load test according to the IEC test standard for PV modules (IEC 61215) [19].

(a) (b)

Figure 2.18: PV modules with mechanical load caused by (a) snow load and (b) in a laboratory mechanical load test according to the test standard for PV modules (IEC 61215) [19].

Thermomechanical stress in PV modules potentially results in defects. Typical defects after soldering are solar cell cracks, metallization detachment or rupture, and solder cracks or detachment [15, 35, 89–91]. According to Köntges *et al.* [92] and Schneller *et al.* [93] solar cell cracking is one of the major degradation mechanisms for PV modules in the field (mean power degradation: 3%/year) and exceptionally crucial for regions with low temperatures or high snow loads (mean power degradation: 7%/year). According to Sopori *et al.* the edge of solar cells are more prone to mechanical stress-induced defects due to pre-damaging from the wafer manufacturing [94]. Figure 2.19 shows typical defects in PV modules caused by thermomechanical stress.

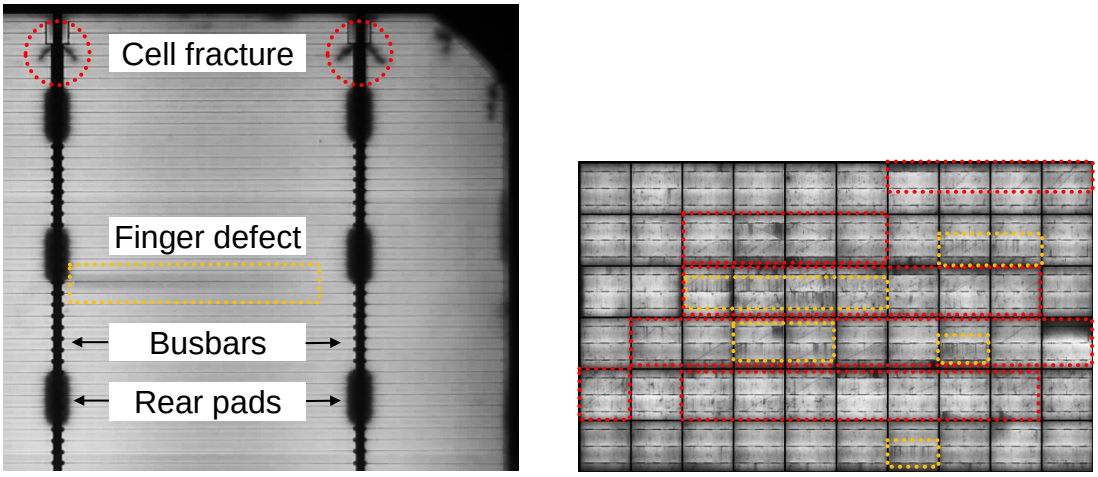

(a) (b)

Figure 2.19: Electroluminescence (EL) images showing characteristic defects caused by thermomechanical stress: (a) diagonal fracture of a silicon solar cell at the busbar ends, as well as finger defects and (b) solar cell fracture and finger defects of a substantially damaged PV module (60 solar cells, size: 1.6 m × 1.0 m) after temperature cycling according to the IEC test standard for PV modules [95].

2.3.2 Solar cell stress analysis

2.3.2.1 Experimental methods to determine mechanical stress

Currently, there are only few methods to measure (thermo-)mechanical stress in solar cells. The methods can be divided into methods with and without mechanical contact to the sample (optical methods). Mechanical stress sensors, for example strain gauges, have to be mechanically attached to the sample and influence the measured stress levels [96, 97]. Another approach uses the piezoresistive properties of silicon to measure mechanical stress by screen-printed contact structures on the surface of a solar cell [98]. However, this approach is still under development and was not available for this study. Wong *et al.* and Zheng *et al.* measured stress in solar cells contactlessly by IR photoelasticity [99, 100]. In addition, X-ray microdiffraction was used to measure mechanical stress in silicon solar cells [101, 102]. Furthermore, with Raman spectroscopy it is possible to measure thermomechanical stress contactlessly by analyzing the phonon energy of a silicon crystal due to inelastic scattering of light [34, 103–105]. However, for all these methods special tools are needed which are complex and time-consuming, hence only small area or line scans are possible.

2.3.2.2 FE analyses

The finite element method (FEM) is one of the most common numerical methods to solve physical problems and can be used to analyze the distribution of (thermo-)mechanical stress. For this reason, in this work mainly the FEM is used to simulate the stress distribution in solar cells after the soldering process. A simplified geometry is subdivided into a number of mesh elements where the problem is solved. In between the nodes polynomial functions interpolate the results. The material behavior is assumed by material models. Boundary conditions and set values also significantly influence the results of the simulation. The validity of the simulation results significantly depends on the accuracy of the assumptions (geometry, boundary conditions, etc.) and the fineness of the used mesh. However, the more precise the material models are and the finer the mesh is, the more degrees of freedom has a model and the more calculation time and hardware requirements are needed. Specifics and a detailed explanation to the FEM can be found in literature [106–108].

2.3.2.3 Mechanical strength of silicon wafers

For an interpretation of (thermo-)mechanical stress it is important to know typical stress levels that cause cracks in in silicon wafers, especially in solar cells. Zhou *et al.* compared the ultimate tensile strength (350 MPa) with the ultimate compressive strength (950 MPa) of (mono-crystalline) silicon [109]. The results show that silicon is more prone to defects caused by tensile stress maxima (compared to compressive stress). For this reason, primarily the first principal stress (σ_I), which represents the tensile stress in the silicon, is analyzed in the following. Rupnowski *et al.* explained that structural imperfections of the silicon wafer, for example grain boundaries, impurities, or crystal defects, increase the probability for cracks [110]. Micro-cracks in a silicon wafer significantly affect the mechanical stability of solar cells [111, 112]. The mechanical strength of silicon solar cells is crucial for the long-term stability of PV modules [113, 114]. The mechanical strength of silicon solar cells was experimentally investigated by several studies [46, 115–117], for example Kaule *et al.* determined an ultimate strength of between 163 MPa and 246 MPa for mono-crystalline silicon solar cells [118]. Table 2.2 shows exemplary fracture strength results for different silicon solar cell samples determined by various experiments.

2.4 Modification of interconnectors

As described in Section 2.3.1, the CTE mismatch of copper interconnectors and silicon solar cells (see Table 2.1) causes thermomechanical stress after the interconnection of solar cells, which is one of the major causes for damages in PV modules. Therefore, the influence of the mechanical properties of an interconnector on the thermomechanical stress in an interconnection, as well as on the bowing of a solar cell has been analyzed and published [40, 119–121].

Thermomechanical stress can be reduced by using interconnectors with lower Young's modulus and yield limit [38–40, 120]. There are different possibilities to modify the mechanical properties of an interconnector: primarily by modifications of the material properties, but also by adapting the geometry of an interconnector. Enhanced thermal treatment in the production process of interconnectors is one possibility to soften the copper core material. A maximum reduction of the yield limit of about −45%

was published by Meier *et al.* [38]. In addition, according to Kang *et al.*, lubrication of copper material and rollers in the cold-rolling step during the production of interconnectors can reduce the yield limit by up to −10% [122]. Stress relief structures substantially change stress levels in interconnections in a PV module. For instance MWT solar cells can be interconnected with specifically designed interconnectors to reduce thermomechanical stress [39, 123]. Figure 2.20 shows an example of an interconnected string of two MWT solar cells.

Table 2.2: Results of several studies to determine the characteristic fracture stress of silicon solar cells.

Experiment setup	**Solar cell type**	**Characteristic fracture stress** [MPa]
4-point-bending [118]	Silicon solar cells[1]	163 - 246
Concentric-ring [46]	Silicon solar cells[2]	65 - 170
4-point-bending [116]	Silicon solar cells[3]	255 - 269
Ball-on-ring [116]	Silicon solar cell sections[4]	365 - 380
Twist test [116]	Silicon solar cells[3]	153 - 162
4-point bending [115]	Silicon solar cells[5]	136 - 222
Ball-on-ring [117]	Silicon solar cell sections[6]	200 - 1300

[1]Mono-crystalline, different solar cell orientations

[2]Mono-crystalline, different metallization layers

[3]Mono-crystalline

[4]16 mm × 16 mm, mono-crystalline

[5]Different multi-crystalline wafer types and diamond wire sawing methods

[6]10 mm × 10 mm, different multi-crystalline wafer types (as-cut and textured)

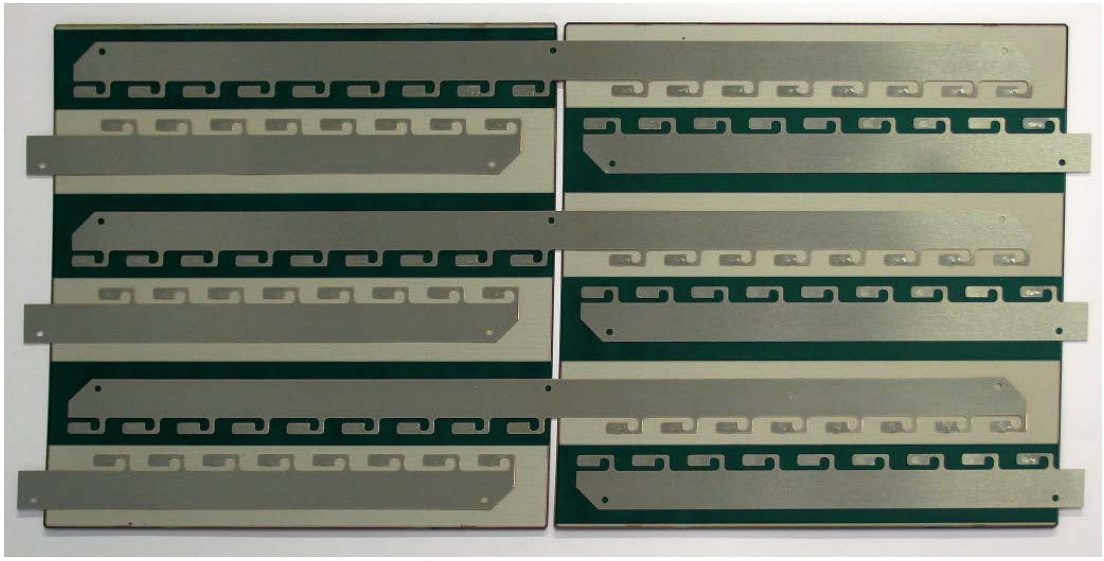

Figure 2.20: Two MWT solar cells (size: 156 mm × 156 mm) with special interconnectors as an example for an interconnector design that aims to minimize thermomechanical stress.

In 2010, Storbeck and Hahn filed a patent application for a wave-shaped ribbon interconnector for the interconnection of solar cells (wave perpendicular to the solar cell surface). They proposed to use toothed wheels and roughly described the mechanical property change of the interconnectors [124]. In 2011, another patent application was filed by Krokoszinski and Amorim that describes the interconnection of solar cells by wire interconnectors with an adapted shape. Here, the wires are deformed in the surface of the solar cells and are used to interconnect BC solar cells [125]. Beyond the context of photovoltaics there are approaches to change the shape of metallic materials. Most importantly Wehr patented a tool to adapt the shape of metallic ribbons in 1999 [126]. These ribbons were not used to interconnect solar cells, but this tool may be used to change the shape of interconnectors for solar cells. Figure 2.21 shows two methods how Storbeck and Hahn suggested to deform ribbon interconnectors by toothed wheels or toothed racks, and how to possibly interconnect two solar cells using reshaped ribbons (a), a BC solar cell connected by wires with an adapted shape deformed by rods as proposed by Krokoszinski and Amorim (b), as well as how Wehr proposed to adapt the shape of a metallic ribbon (c).

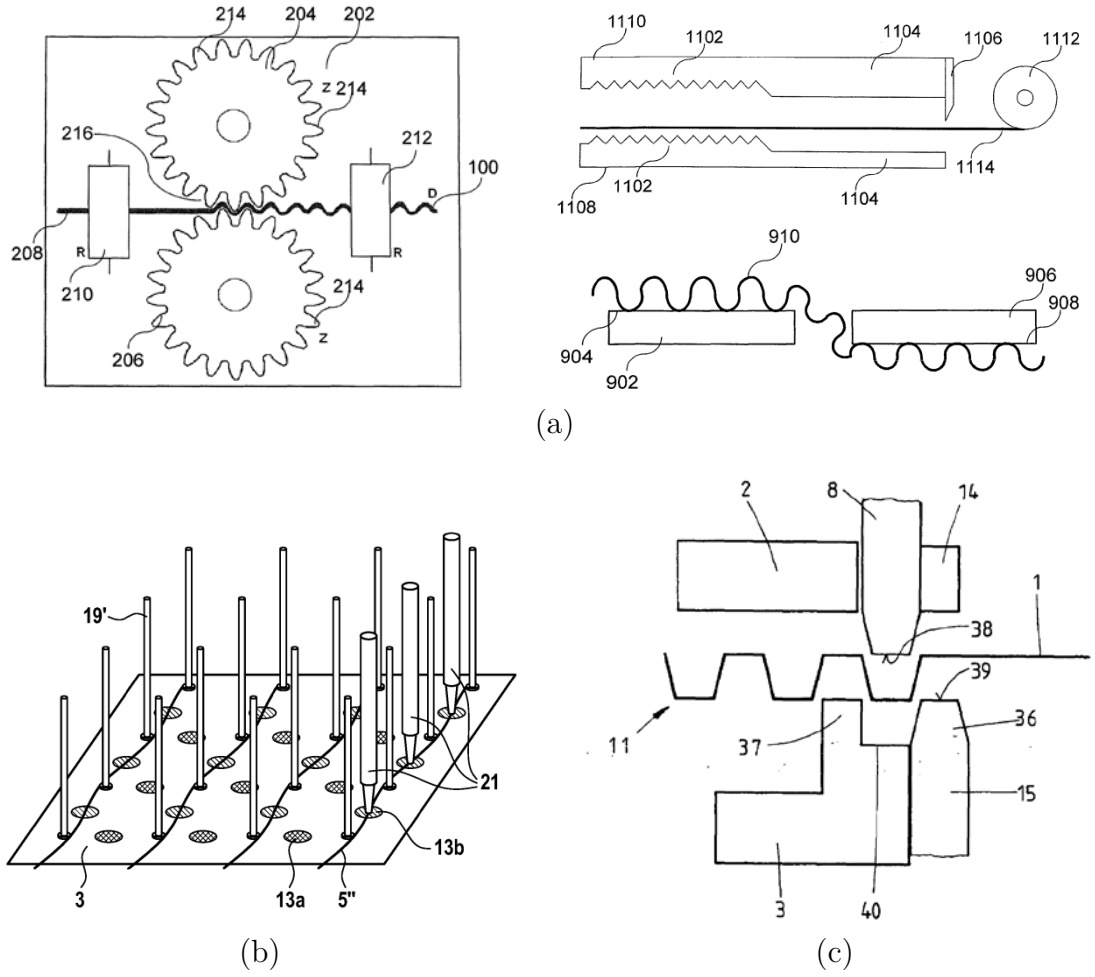

Figure 2.21: Four patented methods how to adapt the shape of ribbons or wires: (a) two reshaping methods proposed by Storbeck and Hahn, and one idea how to interconnect two solar cells with wave-shaped ribbons [124], (b) ribbon interconnection of a BC solar cell by wave-shaped wires (in-plane wave) developed by Krokoszinski and Amorim [125], and (c) approach invented by Wehr [126].

3 Simulating stress caused by the interconnection process

3.1 Background and approach

This chapter intends to reveal most critical areas with maximum stress levels and to identify major influence factors on thermomechanical stress. This leads to guidelines for solar cell and PV module manufacturers to reduce thermomechanical stress, resulting in improved long-term stability of PV modules. For this reason, thermomechanical stress in a silicon solar cell near interconnections, caused by the soldering process, was analyzed by four different simulations using the FEM [95, 119–121].

Simulation I analyzes the deformation of an exemplary solar cell section connected by an interconnector on one side, which is a characteristic attribute for the amount of thermomechanical stress induced by the soldering process. The influence of Young's modulus, yield limit, and diameter of an interconnector on the deformation of a solar cell section connected on one side was evaluated to analyze their influence on thermomechanical stress after the interconnection of solar cells by soldering.

The stress distribution of solar cells with common busbar-based interconnection was analyzed by Simulation II to determine critical areas with maximum stress. Simulation III analyzes the stress distribution after soldering for MBB solar cells that are interconnected by round wires soldered on contact pads. The stress results for both interconnection technologies were compared.

Simulation IV compares thermomechanical stress for single interconnections and linear rows of interconnections attached to a continuous interconnector. Furthermore, the influence of the contact metallization layout on the thermomechanical stress in the silicon solar cell was analyzed.

To determine whether the simulations with its assumptions and chosen configurations deliver plausible results the deformation of an interconnected solar cell with different interconnector wires was simulated (equivalent to Simulation I) and compared with experimentally measured data.

3.2 Modeling

3.2.1 Residual stress

A stack of solar cell, liquid solder and copper interconnector(s) was assumed to be stress-free at and above the solidus temperature of the used solder alloy. Furthermore, residual stresses from the solar cell production were neglected.

3.2.2 Geometry models

Since the thermomechanical stress maxima are expected to be located near the contact pads, the geometry model for Simulation I-III is a solar cell section including one connected pad row. In contrast to Simulation I the solar cell section is connected on both sides for Simulation II and III. Figure 3.1 shows the geometry models of the solar cells that are used for Simulation I-III, calculating bending and thermomechanical stress in solar cell sections with three busbar (3BB) or MBB contact layout respectively. Geometry details and the used meshes are shown by Figure A.1 in the appendix.

The geometry for Simulation IV is one quarter of a solar cell with symmetry boundary conditions. Figure 3.2 shows the geometry that is used for Simulation IV and a detail that shows the used mesh.

3.2.3 Material models

The material parameters used for the simulations were mainly taken from literature. The mechanical parameters of the copper interconnectors were determined by standard tensile tests according to the test standard for metal materials [127]. In the tensile tests the stress-strain-curve was measured. The measurement delivers the engineering stress (σ_{Eng}) and the engineering strain ($\varepsilon_{\mathrm{Eng}}$), which assumes that the geometrical dimensions do not change. The true stress (σ_{True}) and the true strain ($\varepsilon_{\mathrm{True}}$) was calculated by Equation 3.1 and 3.2 to represent the mechanical behavior of the copper material accurately (including geometry changes) [128].

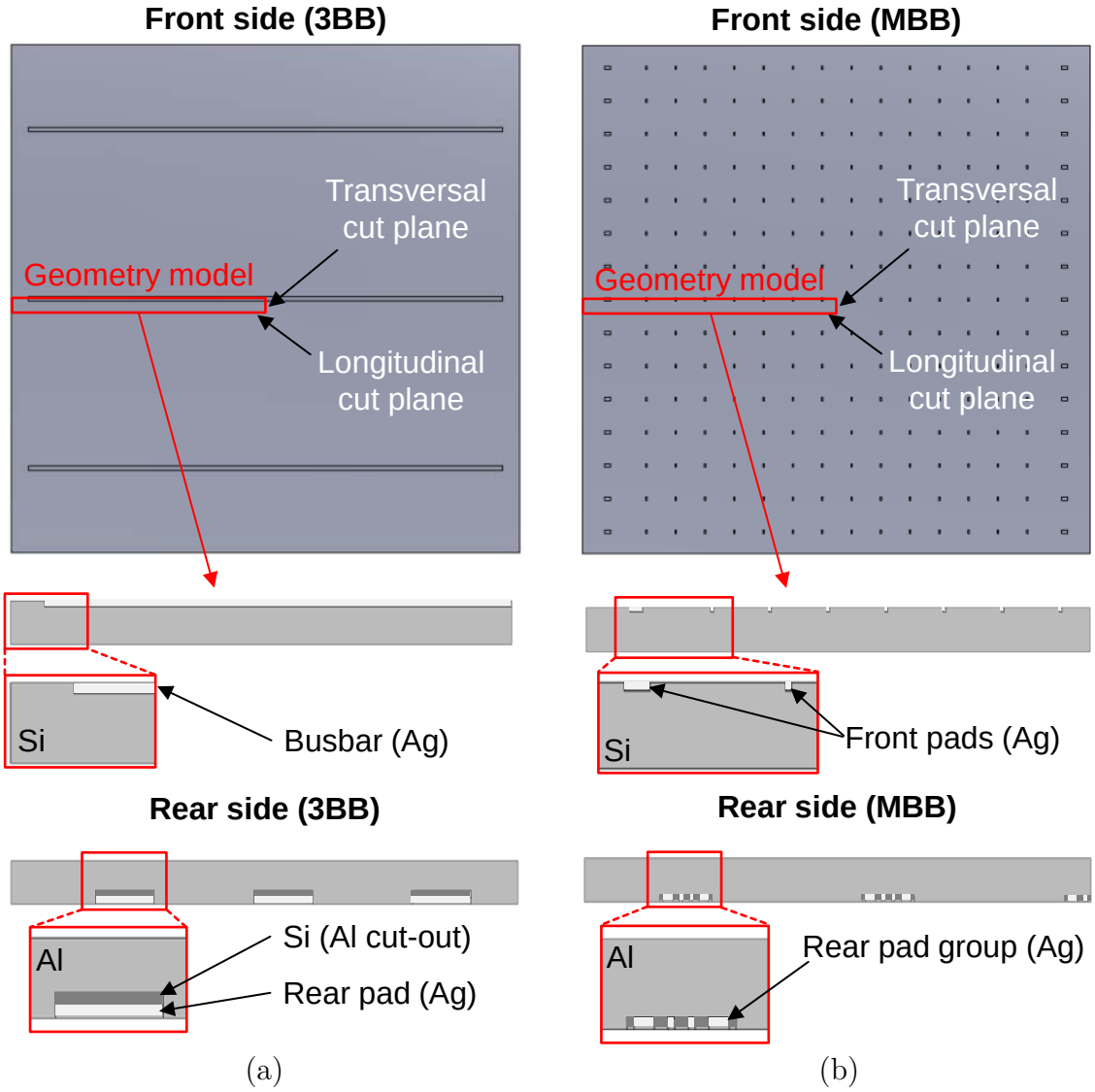

Figure 3.1: Geometries of (a) a 3BB solar cell and (b) a MBB solar cell for simulation 1-3 analyzing thermomechanical stress in connected solar cell sections (size: 78 mm × 10 mm). The area to analyze thermomechanical stress is indicated by the red box. The cut planes (longitudinal and transversal) show where symmetry conditions were applied. The front side of the geometry including one quarter of a busbar or pad row, as well as the rear side with aluminum cut-outs and contact pads are shown [121].

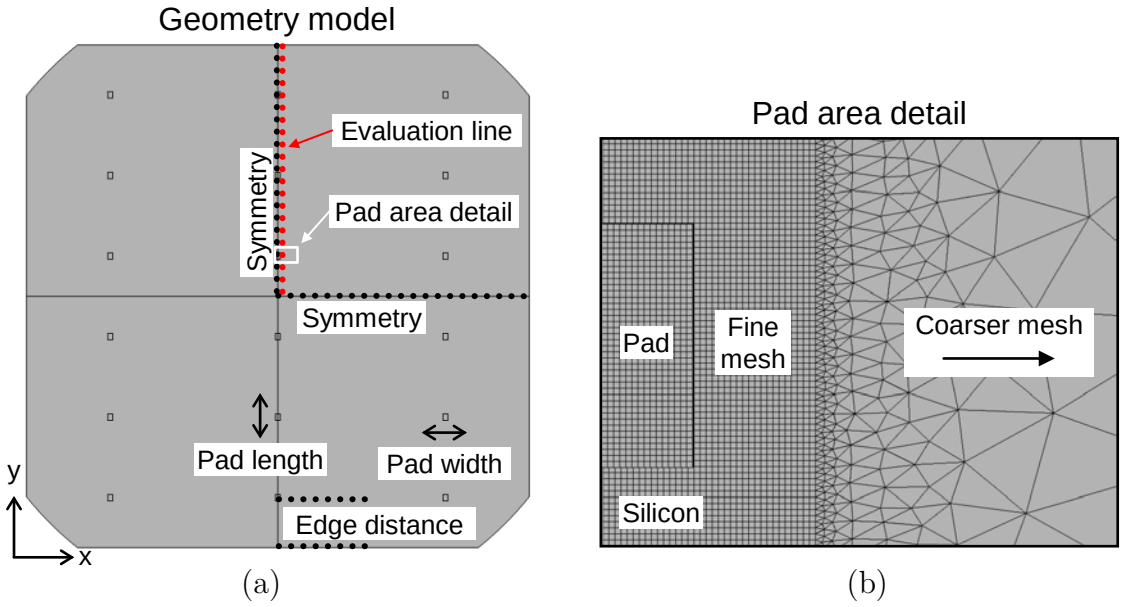

Figure 3.2: Geometry model used for Simulation IV: (a) front and rear side of the solar cell geometry including symmetry conditions (except the additional vertical symmetry condition) and the evaluation line indicated and (b) a geometry detail shows the used mesh in the area of one exemplary contact pad [95].

$$\sigma_{\text{True}} = \sigma_{\text{Eng.}} \cdot (1 + \varepsilon_{\text{Eng.}}) \tag{3.1}$$

$$\varepsilon_{\text{True}} = ln(1 + \varepsilon_{\text{Eng.}}) \tag{3.2}$$

The mechanical behavior of an interconnector in a specified strain range (e.g. up to a strain level of 0.3%) can be approximated by two linear areas, which was done for Simulations I-III. In contrast, Simulation IV uses the whole stress-strain-curve as material model for the copper interconnector. For the aluminum paste, the solder alloy, the silver paste, and the silicon literature values were used. Table 3.1 shows the mechanical properties that were used for the FEM simulations.

Table 3.1: Mechanical properties of the materials in the simulations [121]. The CTEs are listed in Table 2.1.

Material	**Young's modulus** [GPa]	**Yield limit** [MPa]	**Tangent modulus** [GPa]
	Bilinear material model		
Al paste [30, 129]	6.0	28.3	0.06[1]
Copper	70	100	30
	Linear material model		
Solder[2] [130]	16.0	-	-
Ag paste [30, 129]	7.0	-	-
Silicon [88, 131]	Stiffness matrix[3]	-	-

[1]Assumption of a moderate growth of the stress when increasing the strain level above the yield limit

[2]Sn62Pb36Ag2

[3]The material model for silicon includes a Young's modulus tensor with cubic symmetry

3.3 Results

3.3.1 Simulation I: Variation of interconnector properties

Variations of the mechanical wire properties reveal their influence on the deformation of solar cell sections and the thermomechanical stress [120]. Table 3.2 shows the variation of Young's modulus, yield limit and wire diameter, and the simulated relative change of the deformation of a solar cell section. An increase of the yield limit from 100 MPa to 150 MPa results in an insignificant increase of the deformation of only 1%. However, all other variations show significant changes of the deformation of between -72% and +42%.

Table 3.2: Variations of the mechanical wire properties and relative change of the vertical displacement determined by simulation of a solar cell section connected by one wire interconnector on one side [120].

Wire type	**Wire diameter** [µm]	**Young's modulus** [GPa]	**Yield limit** [MPa]	**Tangent modulus** [MPa]	**Rel. disp. change** [%]
Reference	300	70	100	30	
−100 µm	**200**	70	100	30	-72
+100 µm	**400**	70	100	30	+42
−30 GPa	300	**40**	100	30	-37
+30 GPa	300	**100**	100	30	+15
−50 MPa	300	70	**50**	30	-24
+50 MPa	300	70	**150**	30	+1

3.3.2 Simulation II: Three busbar solar cells

Simulation II analyzes thermomechanical stress in most common solar cells with a busbar layout on the front side and pad contacts on the rear side interconnected by solder-coated copper ribbons [121]. Figure 3.3 shows the thermomechanical stress results (first principal stress (σ_{I})) of the simulation in cross sections of a connected solar cell (along the evaluation line indicated in Figure 3.2). The maximum tensile stress in the interconnectors is 145 MPa in the front ribbon and 143 MPa in the rear ribbon. This is larger than the yield limit approximation of 100 MPa, which indicates that typical ribbon interconnectors with a yield limit between 60 and 100 MPa undergo plastic deformation on both front and rear side after the soldering process. In most areas of the silicon solar cell there are only small tensile stress levels. However, the results show two significant stress maxima; one stress peak of about 100 MPa near the end of the busbar (front side), and one stress peak that exceeds 200 MPa located at the outermost contact pad (rear side). Such stress peaks can possibly cause defects in solar cells (example shown by Figure 2.19).

Most importantly, the results show that the interconnectors undergo plastic deformation if their yield limit is below 145 MPa, which reduces thermomechanical stress

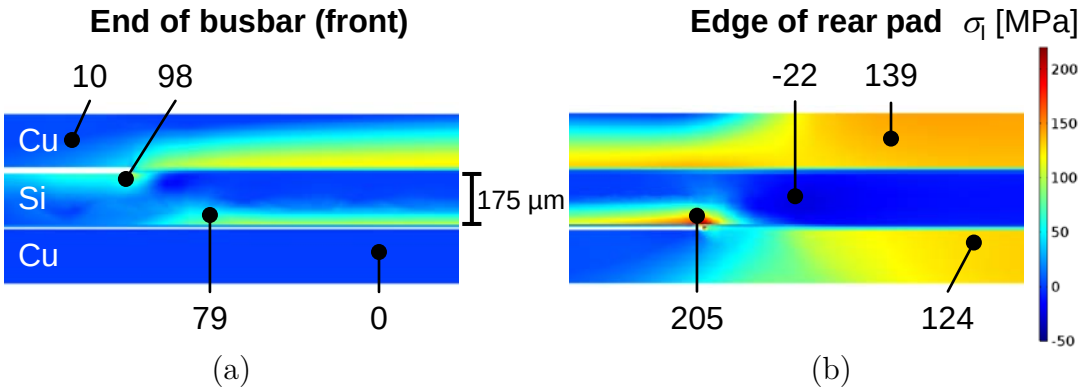

Figure 3.3: Distribution of σ_I in the longitudinal cut plane (along the evaluation line indicated in Figure 3.2): (a) at the outermost pad on the front side and (b) where the outermost pads on the rear side are located (all values in MPa) [121].

in the interconnections and the silicon wafer after the soldering process. In addition, the results show the areas of maximum stress in the silicon which are located at the edges of the outermost contacts on both sides of the solar cell. This indicates that the outermost interconnections need to withstand the most significant stress levels.

3.3.3 Simulation III: Multi busbar solar cells

Simulation III analyzes thermomechanical stress in solar cells with an adapted MBB contact layout on both sides [119–121]. Instead of busbars the solar cells have pad rows and are interconnected by round, solder-coated copper wires (yield limit: 100 MPa, tangent modulus: 30 MPa). On the front side each pad row consists of 16 pads. The outermost pads have a size of 2.0 mm × 1.0 mm, whereas the dimensions of the inner pads are 0.45 mm × 1.0 mm. On the rear side five pad groups with a size of 2.0 mm × 1.6 mm (outer pads of a pad group) or 0.5 mm × 1.6 mm (inner pads of a pad group) are located.

Figure 3.4 shows the distribution of σ_I in the cross section at four characteristic positions. The outermost contact (a) and an inner pad (b) is shown. In addition, the distribution of σ_I in the cross section at the outermost contact (c) and at the position of two inner pads on the rear side (d) is presented. Both wire interconnectors, on the front side and on the rear side, reveal stress levels up to 160 MPa for the wires

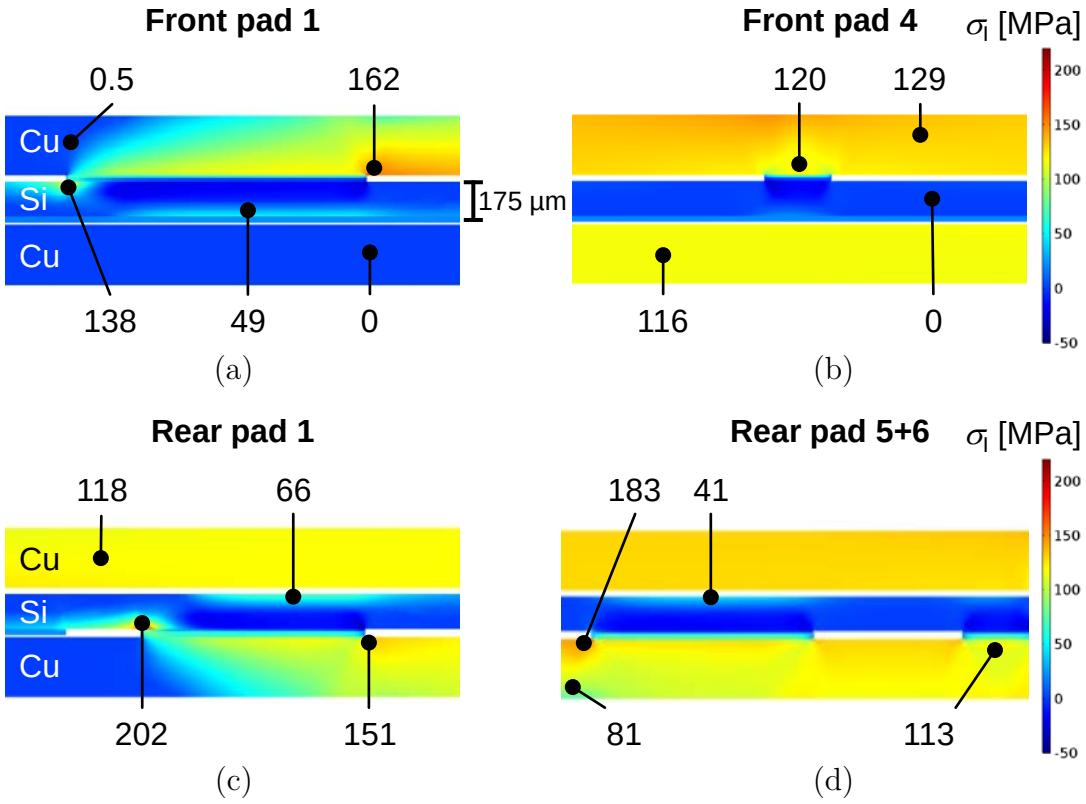

Figure 3.4: Distribution of σ_I in the longitudinal cut plane (along the evaluation line indicated in Figure 3.2): (a) at the larger outermost pad and (b) at the position of an inner pad (front pad 4) on the front side, as well as (c) at the outermost pad and (d) at the position of an inner pad group (rear pad 5 and 6) on the rear side (all values in MPa) [121].

on the front side and 150 MPa for the rear side of a MBB solar cell. The results also show that between the contact pads there is an almost homogeneous stress level of approximately 129 MPa in the front wires and 116 MPa in the rear wires. Furthermore, the stress level in the wire interconnectors is slightly lower adjacent to the contact pads (front side: 120 MPa, rear side: 113 MPa). This indicates that the wire interconnectors undergo plastic deformation after the soldering process. In most parts of the silicon solar cell the simulation results show low tensile stress levels. However, the results reveal local stress peaks; approximately 140 MPa adjacent to the first front pad and above 200 MPa adjacent to the first rear pad.

3.3.4 Simulation IV: Different contact pad layouts

The main goal of this analysis was to understand how different segments of an interconnector influence the stress distribution in a silicon solar cell. For this simulation, instead of a bilinear material model for copper, the stress-strain curve of an interconnector is used. In addition, instead of a solar cell section, a full solar cell (quarter of a solar cell with symmetry boundary conditions) is used as material model (see Figure 3.2). However, most model assumptions (e.g. material models, temperature change, etc.) are identical as for Simulation I to III. By Simulation IV the stress distribution in solar cells was simulated with three different interconnector configurations; with interconnectors only on contact pads (single pad soldering, in the following referred to as on pads configuration), with interconnectors only in between pads (connecting pads only with a slight overlap at the edges, in the following referred to as between pads configuration), and with continuous interconnectors (in the following referred to as continuous configuration). For each configuration, a number of mesh elements is ignored due to singularities, which is shown by Figure A.2 in the appendix. Additionally, by Simulation IV, thermomechanical stress in solar cells with different contact pad layouts is compared to determine the influence of the contact layout on the maximum stress level and distribution [95].

3.3.4.1 Comparison of different contact configurations

Figure 3.5 shows the three different contact configurations (a), as well as the thermomechanical transversal stress (σ_{XX}) and longitudinal stress (σ_{YY}) along the pad rows (6 pads on a full solar cell, pad length: 2.0 mm, pad width: 1.5 mm) on the surface of one quarter of a silicon solar cell connected by a ribbon interconnector (b, c). The results indicate that the stress maxima are located directly adjacent to the contact pads. For this reason, the analysis is focused on the transversal and longitudinal stress in the center of one pad row as indicated by the evaluation lines in Figure 3.5 (b) and (c).

For the three different configurations the transversal and longitudinal stress on the silicon surface along the evaluation line is shown by Figure 3.6. The transversal stress curve (σ_{XX}) of the on pads configuration shows only compressive stress with a

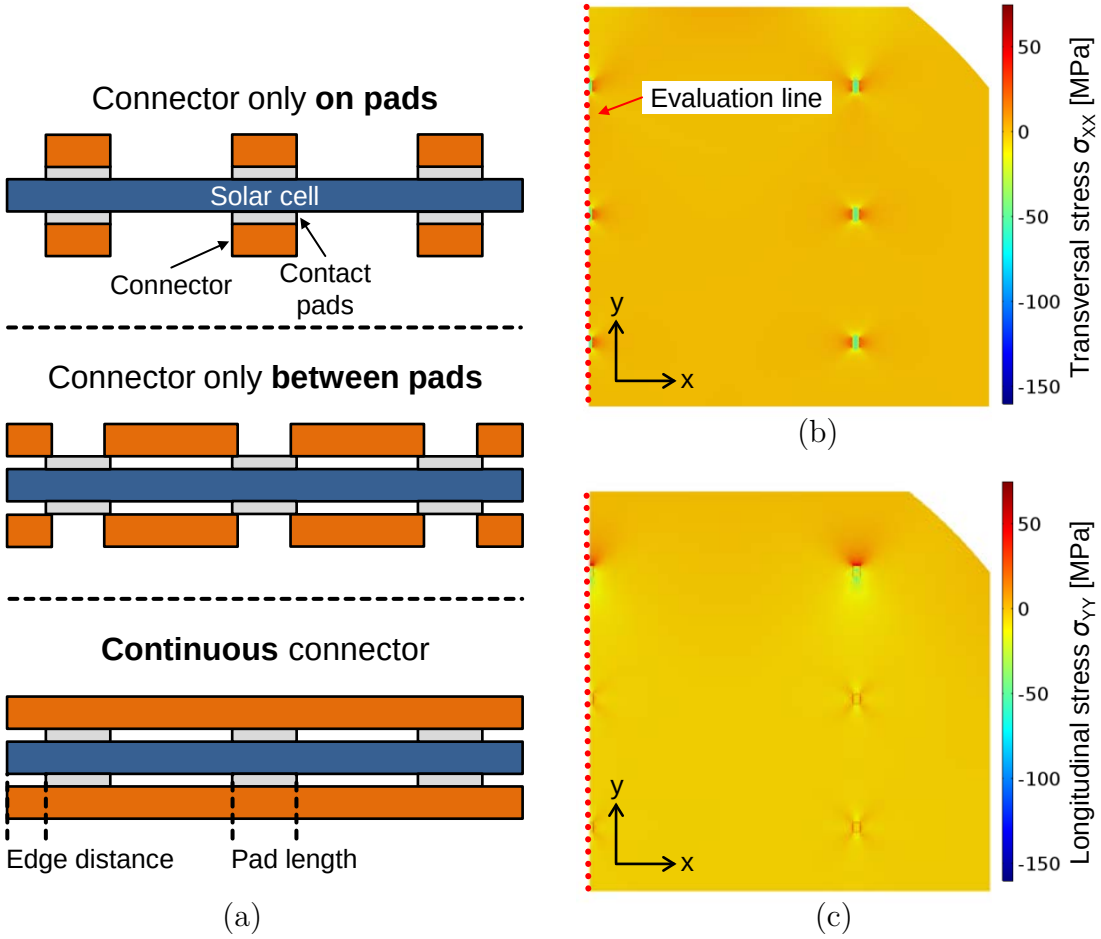

Figure 3.5: (a) Schematic longitudinal cut drawings of the three simulated contact configurations, as well as (b, c) the distribution of the thermomechanical stress on the surface of a quarter of a silicon solar cell caused by cooling down after soldering continuous interconnectors on the pad rows (6 pads on a full solar cell, pad length: 2.0 mm, pad width: 1.5 mm). Shown is (b) the transversal stress σ_{XX}, and (c) the longitudinal stress σ_{YY} (in MPa) on the solar cell surface (size: 78 mm × 78 mm). The evaluation line indicates where the stress is analyzed in detail [95].

maximum of about −112 MPa in the pad areas, whereas the longitudinal stress (σ_{YY}) shows tensile stress peaks up to 22 MPa at the pad edges and compressive stress with a maximum of about −108 MPa in the pad area. In between the pads the stress level rapidly decreases to zero. For the between pads configuration the transversal stress curves (σ_{XX}) show insignificant stress levels between −15 MPa and 4 MPa for inner pads and a stress peak of −31 MPa at the edge of the outermost contact pad. The longitudinal stress (σ_{YY}) shows tensile stress peaks in the pad spacings near the pad edges with a maximum of 55 MPa. In addition, the compressive stress in the pad spacings near the pad edges reaches maxima of −31 MPa. The slight material overlap (as visible in Figure 3.5 (a)) causes small stress peaks of 20 MPa near the outermost pad edge. As expected, stress is reduced in the pad centers because there is no copper material attached.

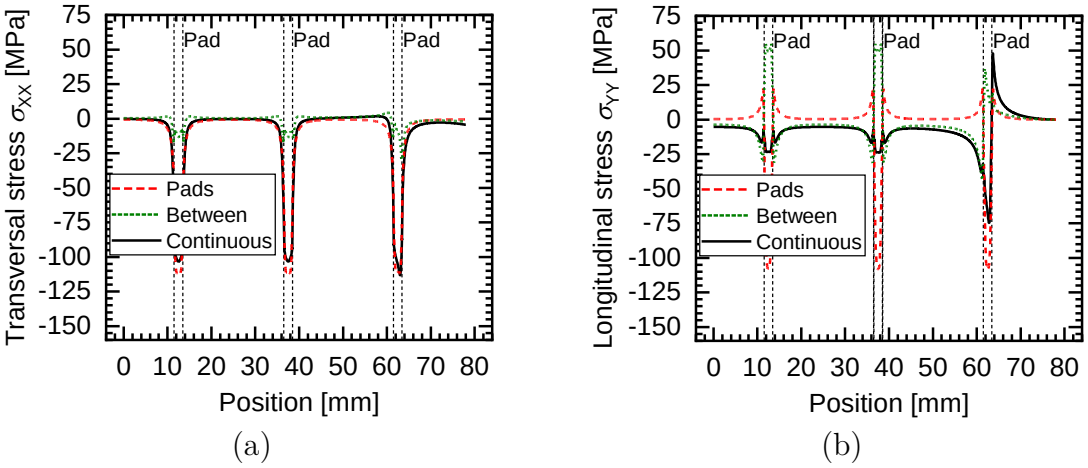

Figure 3.6: Comparison of the thermomechanical stress in a silicon solar cell for different contact configurations: on pads only (Pads), in between pads (Between) and continuous connection (Continuous). For a pad length of 2 mm (a) σ_{XX} and (b) σ_{YY} on the silicon solar cell surface under half of a pad row are shown [95].

For the transversal stress (σ_{XX}) the continuous configuration shows comparable stress levels as the on pads configuration. However, the maximum compressive stress of about −103 MPa is slightly lower. Except for the outermost contact pad edge, the curves of the longitudinal stress (σ_{YY}) show only compressive stresses, with a maximum of −34 MPa located at the pad center, and nearly no stress in the middle of the pad spacings. For uninterrupted connection with continuous interconnectors the

maximum tensile stress of 48 MPa is higher and the compressive stress of −75 MPa is lower compared to the on pads configuration (tensile stress: 22 MPa, compressive stress: −108 MPa).

3.3.4.2 Contact pad layout variations

Figure 3.7 (a) and (b) show the maximum transversal (σ_{XX}) and longitudinal (σ_{YY}) compressive stress of the inner pads for different pad lengths (constant number of 6 pads per pad row on a full solar cell), as well as for different pad distances and numbers (constant pad size: 2.0 mm × 1.5 mm) compared to a busbar. The results indicate that the larger the pad length the higher is the compressive stress. Maximum compressive stress levels between −83 MPa (0.4 mm pads) and −124 MPa (23 mm pads) in the transversal direction and between −13 MPa (0.4 mm pads) and −39 MPa (23 mm pads) in the longitudinal direction are located at the contact pads. The maximum compressive stress of −40 MPa and −125 MPa in longitudinal and transversal direction was determined for the busbar layout. This shows that the larger the contact pads are, the higher is the compressive stress maximum at the pad locations, ending up at the largest stress levels for a continuous busbar. Furthermore, with decreasing pad distance and, for this reason, increasing number of pads (with constant pad size), the maxima of the compressive stress at the inner pad locations, longitudinal, as well as transversal, increase.

Located at the contact pads the results show a compressive stress maximum between −103 MPa (25 mm pad distance) and −115 MPa (1 mm pad distance) in the transversal direction and between −17 MPa (1 mm pad distance) and −38 MPa (25 mm pad distance) in the longitudinal direction. Under a continuous busbar the homogeneous stress level is −125 MPa in transversal and −40 MPa in longitudinal direction. In addition, Figure 3.7 (c) shows the maximum tensile and compressive stress in longitudinal direction at the outermost contact pads of pad rows with different distances between pad edge and solar cell edge. There is a significant tensile stress peak up to 48 MPa for pad edge to cell edge distances larger than 8 mm that decreases with smaller distance between pad edge and cell edge. Furthermore, the compressive stress maxima of the longitudinal stress curves decrease with increasing distance

between pad edge and cell edge and are between −75 MPa (17 mm edge distance) and −115 MPa (0 mm edge distance).

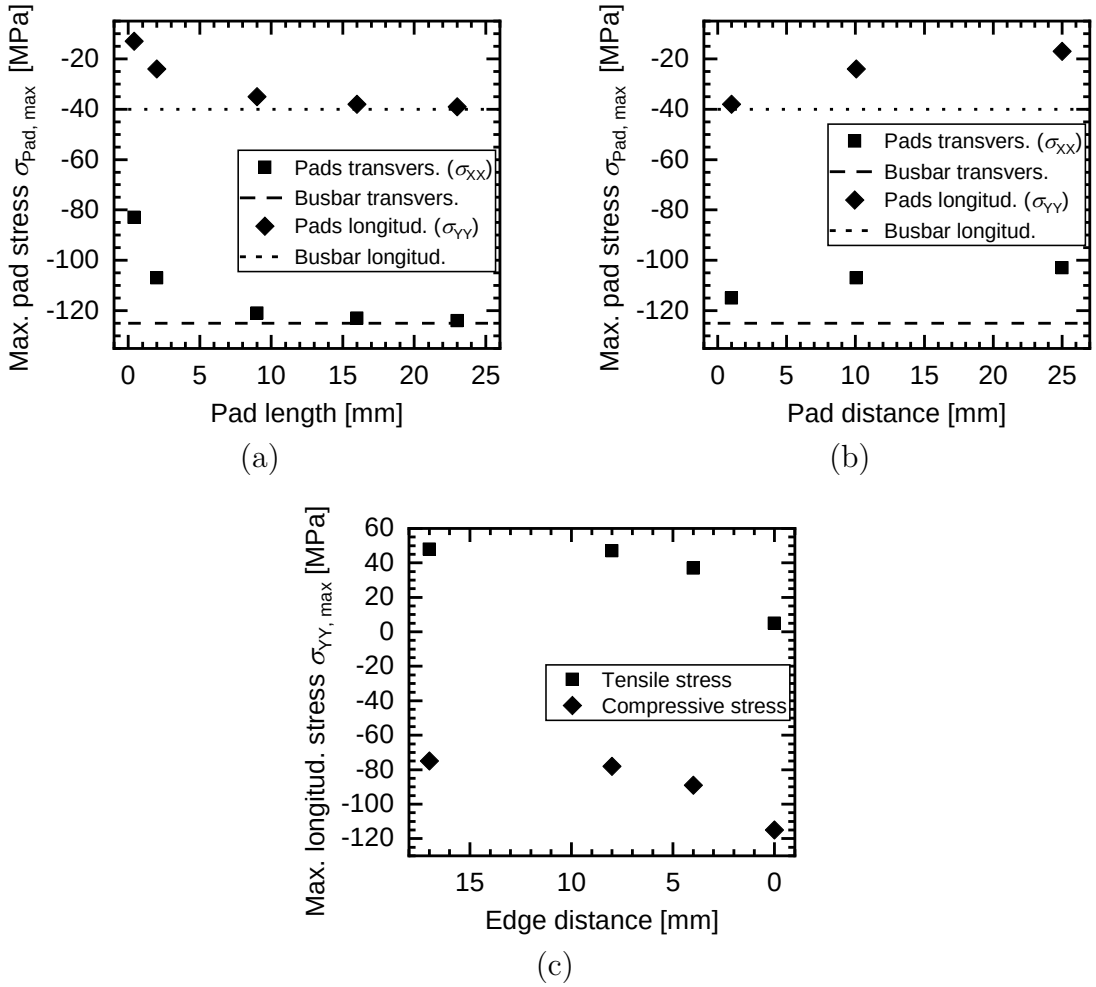

Figure 3.7: Maximum compressive stress levels (transversal and longitudinal): (a) for different pad sizes at the locations of the inner pads (excluding the edges of the outermost pads), (b) for different pad distances at the locations of the inner pads (excluding the edges of the outermost pads), and (c) the maximum longitudinal tensile and compressive stress at the outermost pads near the cell edge for pad rows with different distances to the solar cell edge [95].

3.4 Experimental verification

An experimental verification was prepared for the deformation of solar cell sections as analyzed by simulation I-III [119]. Measurements of (thermo-)mechanical stress in a full solar cell (described by Section 2.3.2.1) was not performed due to its complexity and the lack of availability of required methods. The deformation of solar cell sections connected by an interconnector on one side was simulated. In addition, six groups of solar cell sections (laser-cut, size: 78 mm × 10 mm, solar cells as shown by Figure 2.7) were connected by different round copper wire interconnectors. Original wires from the roll and pre-stretched wires (1% relative length increase) with a copper core diameter of 250, 300, and 430 µm were used. The deformation was measured by an optical distance sensor at two different positions. The calculated simulation results and the measured deformation data from the experiment were compared. Figure 3.8 (a-c) shows how the deformation of the connected solar cell sections was measured. Furthermore, Figure 3.8 (d) reveals that the results of simulation and experiments are comparable. This demonstrates that trends and locations with maximum stress levels determined by Simulation I-IV can be assumed to be valid. The results of the experimental verification show that, despite the assumptions and simplifications, the simulation delivers data that enable an analysis of the stress distribution caused by interconnection process for silicon solar cells.

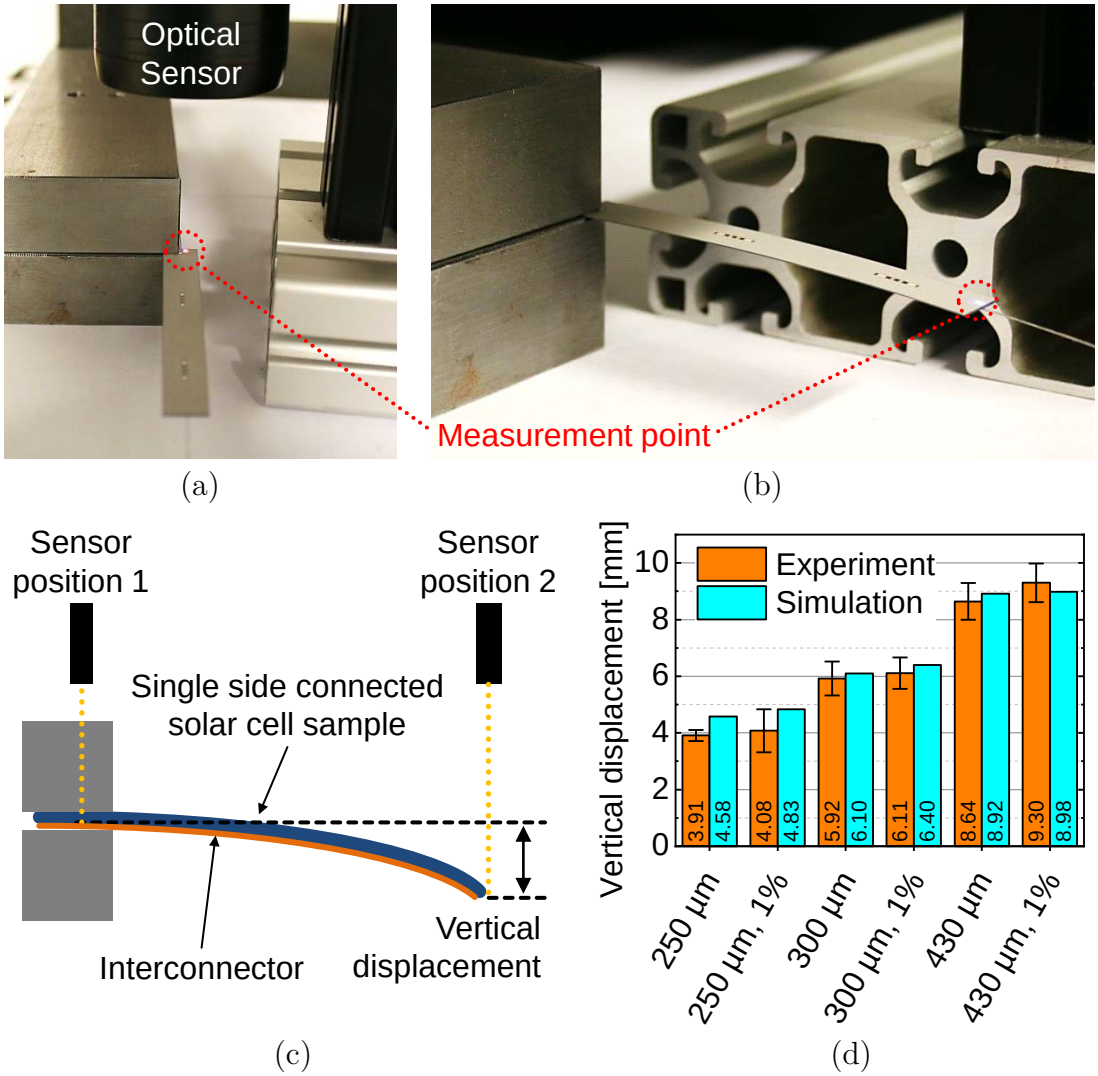

Figure 3.8: Deformation of a solar cell section connected on one side (size: 78 mm × 10 mm): (a, b) measurement setup showing the measurement points to determine the vertical displacement, (c) schematic drawing of how the measurement of the deformation is performed, and (d) the comparison of the simulated vertical displacement and the measurement results for wire interconnectors with a diameter between 270 and 430 µm (initial state and 1% pre-stretched) [119].

4 Pilot experiments with wave-shaped wires

4.1 Concept description

In this work, the focus is to reduce thermomechanical stress for wire-based interconnection of silicon solar cells, particularly BC solar cells. As shown in Chapter 3 thermomechanical stress is influenced by the layout of the contact metallization. However, it was also shown that the mechanical interconnector properties significantly influence thermomechanical stress. Adapting the mechanical properties, especially the yield limit and the Young's modulus, has the potential to substantially reduce thermomechanical stress. This has been determined by simulations and the results are shown in Table 3.2. Wave-shaped wires for the interconnection of silicon solar cells is a new concept that presumably reduces thermomechanical stress significantly. In between two contact pads of a solar cell a horizontally wave-shaped interconnector (in the surface plane of the solar cell) behaves like a mechanical spring. When the temperature changes the copper material still contracts, but the direction differs. This results in less wire deformation linear to contacts in a row and therefore less deformation of the connected material. For this reason, wave-shaped interconnectors are expected to be advantageous, especially for BC solar cells that are only connected on one side. Figure 4.1 shows schematic drawings of a wave-shaped and a straight wire interconnector on three contact pads, including arrows that indicate the contraction of the wire interconnectors when the temperature decreases.

4.2 Pilot experiments

To assess the concept first experiments were performed. First, the mechanical behavior of preliminary wave-shaped wire samples was analyzed by tensile tests according to the test standard for metallic materials [127]. Second, bending of solar cell sections connected by different wave-shaped wires on one side was measured

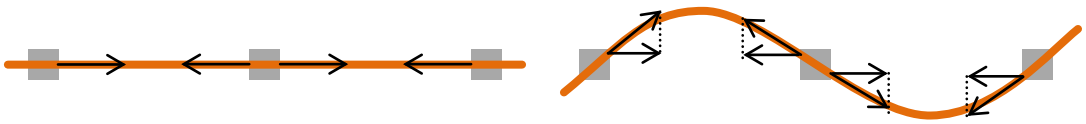

(a) (b)

Figure 4.1: Schematic drawing of the contraction due to a temperature decrease (indicated by arrows) caused by (a) a straight and (b) by a wave-shaped interconnector soldered on contact pads (equivalent force between the pads of a pad row indicated by arrows).

and compared to bending caused by straight wire interconnectors. Third, soldering of wave-shaped wires on very small contacts was tested and fourth, the long-term stability of contact pad rows on solar cells connected by wave-shaped and by straight wires was measured by electroluminescence (EL) measurements and temperature cycling according to the IEC test standard for PV modules [19].

4.2.1 Mechanical characterization of first wire samples

To roughly analyze the mechanical behavior of wave-shaped wires samples were manufactured with a simple hand-tool that is normally used to deform and shorten wires in beehives. This tool uses two toothed wheels that are manually pressed together to change the shape of a wire. Figure 4.2 shows a photograph of the tool and the preliminary manual reshaping process.

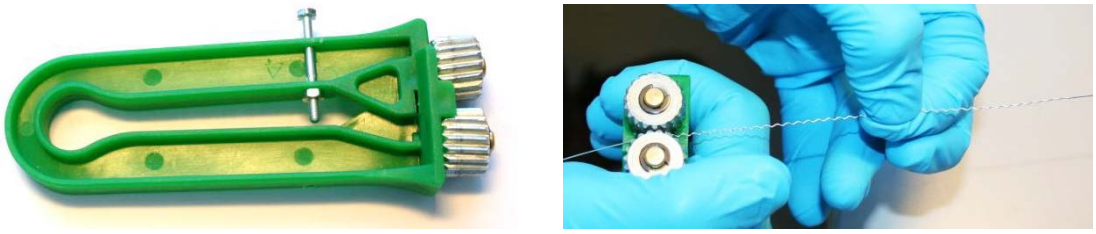

(a) (b)

Figure 4.2: (a) Hand-tool to manufacture first wave-shaped wires and (b) photograph of the manual reshaping process, as well as the resulting wire.

Tensile tests of straight and wave-shaped wires were performed to analyze how the mechanical behavior is affected by the geometry change. Figure 4.3 shows the results of tensile tests on first wire sample groups. For the wave-shaped wire samples, the axes are called pseudo stress and relative elongation, since stress in the copper is assumed to be non-homogeneous and there is a material, as well as a shape deformation. The measured tensile test curves show that for specific strain values a wave-shaped wire causes significantly lower stress levels compared to a straight wire.

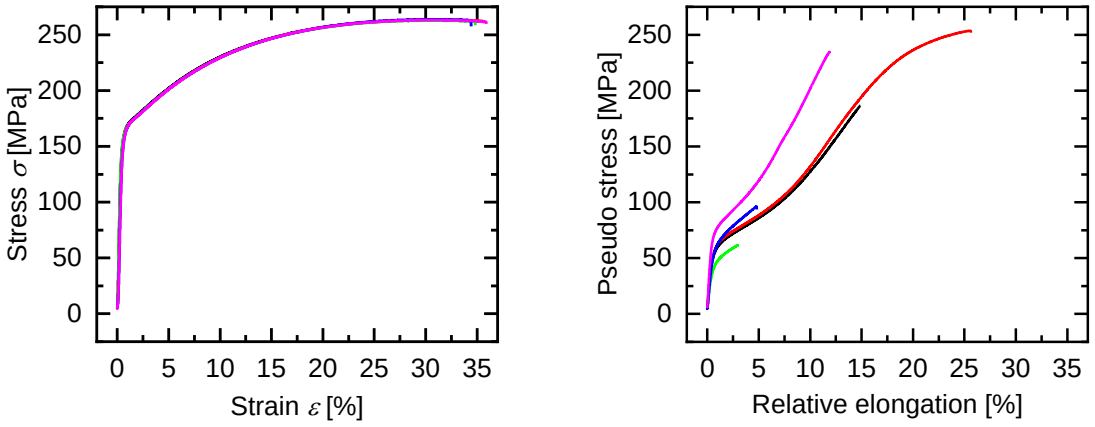

Figure 4.3: Measured stress-strain curves of (a) five straight wire interconnectors and (b) five wave-shaped wires manufactured with the hand-tool shown in Figure 4.2 (b). For the wave-shaped wires the axes are called pseudo stress and relative elongation because the material is stretched and bended at the same time, resulting in non-homogeneous stress and strain in the copper material.

Using the CTEs of copper and silicon (see Table 3.1), it can be calculated that the maximum strain level in an interconnector caused by the temperature changes in a standard temperature cycling (TC) test (between -40 and $85\,^{\circ}\mathrm{C}$) is far below 1%. For example, when using Sn60Pb40 as solder alloy, the stress-free temperature is the solidus temperature of $183\,^{\circ}\mathrm{C}$ [130]. The maximum difference of the relative thermal deformation strain (ε) at $-40\,^{\circ}\mathrm{C}$ is 0.32% using

$$\varepsilon = CTE \cdot \Delta T. \tag{4.1}$$

For this reason, the beginning of the stress strain curve is most relevant for an analysis of the thermomechanical stress caused by the interconnectors in PV modules. The measured curves show a substantial influence of the wave-shaping process on the mechanical behavior of a wire interconnector. Especially for low strain values the measured stress is significantly lower for wave-shaped wires compared to straight wire interconnectors. According to Table 3.2, a reduced yield limit reduces thermomechanical stress due to the soldering process. However, the curves also show that the reshaping process is not ideal. The large curve deviations for the wave-shaped wires compared to the group of straight wire interconnectors indicate that there are variations of the amplitude. In addition, the stress-strain curves of the wave-shaped wires end at different and for some wires at low strain levels, which indicates that some wires have been pre-damaged in the wave-shaping process. Optimizations of the wave-shaping process are described in chapter 5.

4.2.2 Solar cell bending due to single side soldering

The deformation of solar cell sections, cut by a laser (78 mm × 10 mm) and connected by an interconnector on one side, was analyzed. Commercially available MBB solar cells were used. Each sample has one pad row including eight contact pads on the front side. The soldering was done manually using a solder iron. The CTE mismatch causes deformation of the samples after the soldering process, which can be seen as an indicator for the amount of induced thermomechanical stress. The larger the deformation, the higher is the thermomechanical stress. For four different interconnector types the deformation of 10 samples was determined. Two straight wire interconnectors with a diameter of 300 µm and with high (Hard: ~150 MPa) and low yield limit (Soft: ~100 MPa) were analyzed. In addition, two wave-shaped wires with different amplitudes, small (Wave 1: ~0.5 mm peak-to-peak) and large (Wave 2: ~1.0 mm peak-to-peak), were compared. Each wire type is coated with solder (Sn62Pb36Ag2). The deformation was measured as described by Figure 3.8 (a). Figure 4.4 shows the maximum deformation of samples connected by different wire types.

The results show a mean deformation of the samples connected by the harder wire interconnectors of 6.7 mm, whereas the softer wire interconnectors cause a mean

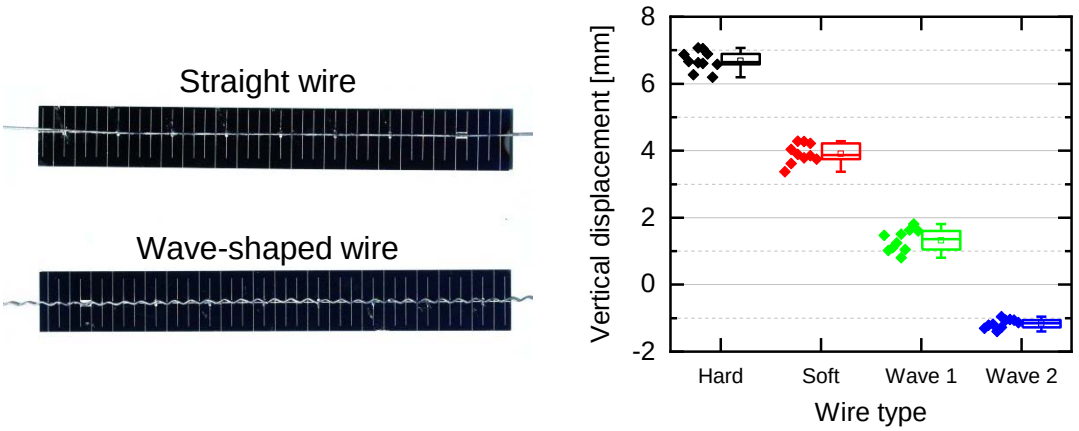

(a) (b)

Figure 4.4: (a) Laser-cut solar cell sections (78 mm × 10 mm) connected by straight and wave-shaped wires, as well as (b) the maximum deformation of each sample after the soldering process (yield limit of about 150 MPa (Hard) or 100 MPa (Soft), peak-to-peak amplitude of about 0.5 mm (Wave 1) or 1.0 mm (Wave 2)).

deformation of 3.9 mm. Furthermore, a mean sample deformation of the samples connected by wave-shaped wires of 1.3 mm for wire interconnectors with a small amplitude (Wave 1) and −1.2 mm for large amplitudes (Wave 2) was determined. The negative deformation for wave-shaped wires with large amplitudes is presumably caused by the aluminum layer on the rear side of the samples, which also causes thermomechanical stress that, in this case, exceeds the deformation caused by the wire interconnector.

4.2.3 Direct soldering on the contact finger grid

In this experiment, wave-shaped wires were connected directly on the finger grid of a commercially available silicon solar cell by manual soldering [132]. The finger distance of the used solar cell is 1.94 mm and the maximum finger width is 70 µm. Furthermore, the long-term stability was analyzed by temperature cycling. Figure 4.5 shows the front side and the rear side of a common solar cell (3BB) that is connected by six wave-shaped wires on each side. On the front side, the wave-shaped wires with a diameter of 300 µm, an amplitude (peak-to-peak) of 1.5 mm, and a period of 3.1 mm were soldered on the finger grid. On the rear side each pad row is connected

by two wave-shaped wires with the same diameter, but an amplitude of 0.8 mm and a period of 1.6 mm (smaller amplitude and period of rear wires chosen due to narrow rear pads).

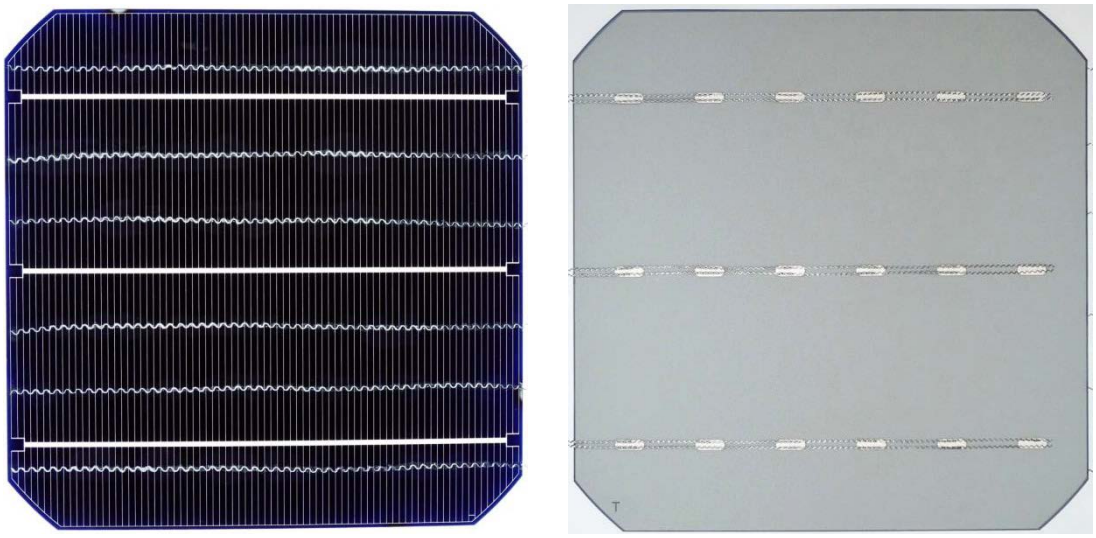

(a) (b)

Figure 4.5: (a) The front and (b) the rear side of a 3BB solar cell (size: 156 mm × 156 mm) connected by six wave-shaped wires on both sides. On the front side the wires are soldered on the finger grid, whereas on the rear side each row of contact pads is connected by two wave-shaped wires [132].

The solar cells, one with wave-shaped wires and one reference with standard busbar and ribbon interconnection, were laminated to determine the long-term stability of the interconnections in a solar module setup. Temperature cycling according to the IEC test standard for PV modules up to 370 cycles was performed [19]. EL and electrical measurements (current and voltage (IV)) were performed after lamination (initial) and after 50, 170, and 370 thermal cycles. Figure 4.6 shows the EL images of the initial mini-module with wave-shaped wires and the final measurement after 370 thermal cycles.

Figure 4.7 shows the results of IV measurement of both module samples (3BB and with wave-shaped wires). The development of the electrical parameters show a comparable behavior of both module samples. The short-circuit current (I_{SC}) and the open-circuit voltage (V_{OC}) show only insignificant changes within the measurement

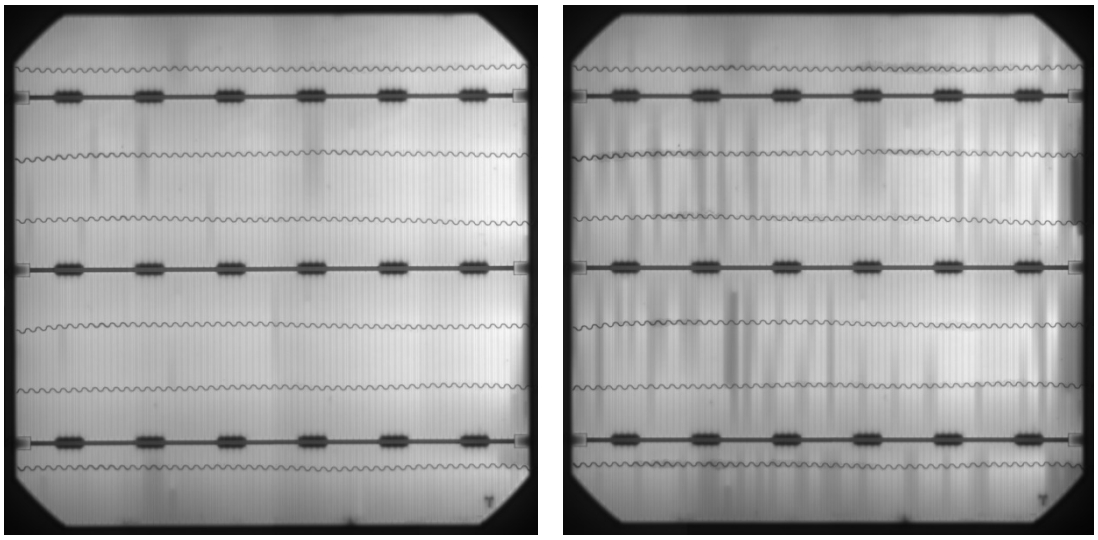

(a) (b)

Figure 4.6: EL images of a PV module including one solar cell (size: 156 mm × 156 mm) connected by wave-shaped wires: (a) EL image after the lamination process and (b) after 370 thermal cycles according to the IEC test standard for PV modules [132].

uncertainties (V_{OC}: ±1.5%, I_{SC}: ±2.0%, power at the maximum power point (P_{MPP}): ±3.5%, fill factor (FF): ±3.0%). Most importantly, the FF, as well as the P_{MPP} reveal a degradation of below −2% after 370 thermal cycles for both module samples, demonstrating a comparable long-term stability meeting the threshold degradation value of the IEC test standard of less than −5% after 200 thermal cycles [19].

4.2.4 Temperature cycling of pad rows with wave-shaped wires

This experiment's target was to compare the long-term stability of pad rows connected by straight wire interconnectors and by wave-shaped wires. In addition, the long-term stability of single pads was analyzed. A comparison of the defect rate shows the influence of thermomechanical stress on the long-term stability of interconnections for different contact configurations. The connected samples are laser-cut solar cell sections (156 mm × 10 mm). For this experiment solar cells with a specific design

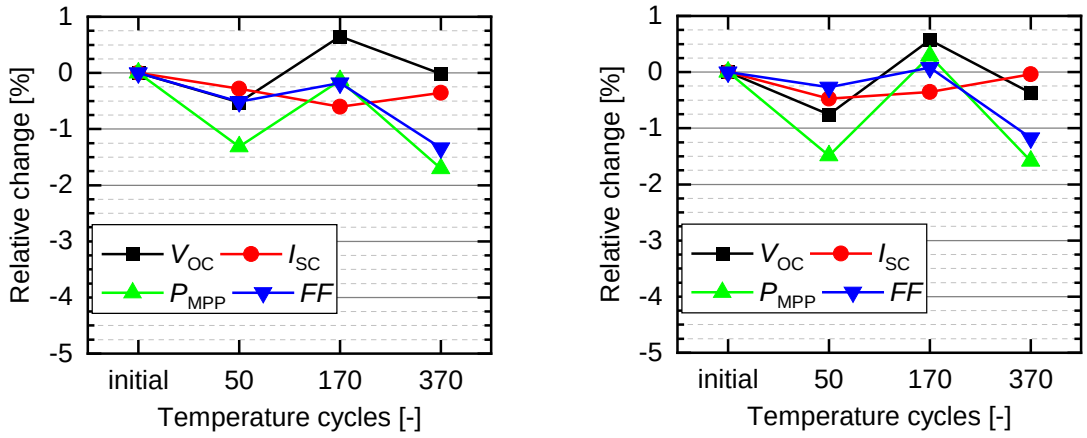

Figure 4.7: Development of the measured electrical parameters of a PV module including (a) one solar cell connected by wave-shaped wires and (b) a solar cell with standard busbar-based interconnection (3BB). Shown is the relative change of the electrical parameters after the lamination process (initial), and after 50, 170, and 370 thermal cycles according to the IEC test standard for PV modules [132].

were used to reveal contact defects. Each sample has 24 contact pads that were connected by soldering. The soldering was done semi-automatically with IR light. Three different sample groups, each including three samples, were connected by wire interconnectors with a diameter of 300 µm and a solder coating (Sn62Pb36Ag2). The pad rows of the samples of the first two groups were continuously connected by straight wire interconnectors or wave-shaped wires on both sides. In the third group each sample is connected by five independent wire interconnectors that were soldered on one contact pad (Single pads) and one wave-shaped wire on the rear side. Subsequently, the connected samples were embedded in a standard module setup (see Figure 2.5) and underwent up to 800 thermal cycles according to the IEC test standard for PV modules [19]. Figure 4.8 (a) shows a photograph of the three sample types with a pad row continuously connected by a straight or a wave-shaped wire or with single pad connection. Furthermore, by Figure 4.8 (b) the development of defects for each interconnection type is shown.

The results indicate the relative amount of pad failures of the samples optically detected by EL measurements. The mean value, as well as the result for each sample is shown. For straight wire interconnectors an approximately constant increase of the relative amount of pad failures was determined, ending at 57% after 800 thermal cycles. For the samples connected with wave-shaped wires the increase of the relative amount of pad failures ends up at about 27%. Furthermore, the results reveal the long-term stability of single interconnections, showing no defects after up to 400 thermal cycles. However, single interconnections start failing after 400 thermal cycles, ending at the same amount of pad failures as pad rows connected by wave-shaped wires after 800 thermal cycles.

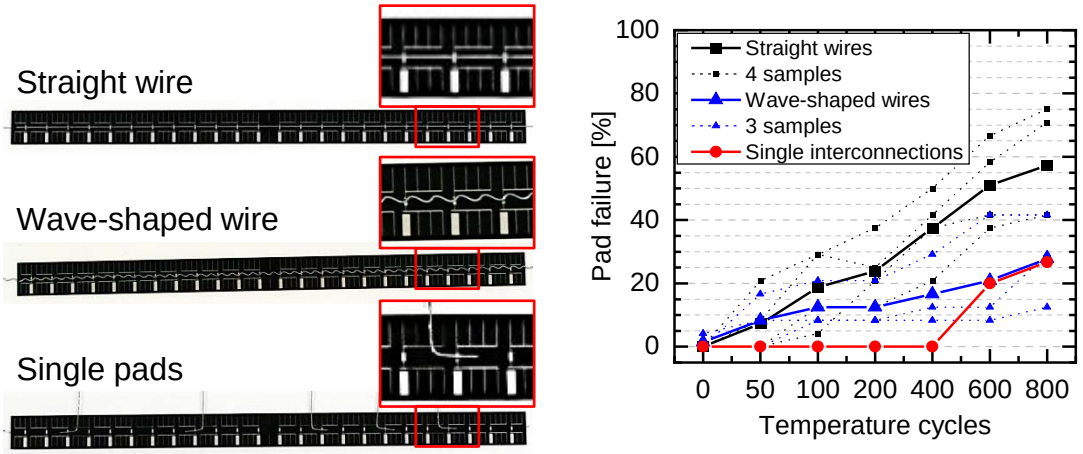

Figure 4.8: (a) Front side of three sample types: solar cell section (size: 156 mm × 10 mm) connected by straight wire interconnectors, by wave-shaped wires, and single pad soldering, as well as (b) the relative amount of defect pads after up to 800 thermal cycles according to the IEC test standard for PV modules [19]. The dotted curves show the amount of pad failure of the samples and the thick lines show the mean value for each sample group.

5 Manufacturing and characterization of wave-shaped wires

5.1 Manufacturing methods

Main goals were to identify a method and to develop a machine that is able to manufacture wave-shaped wires with minimized wire damaging, well-controlled geometry, and high reproducibility. Furthermore, the process should be fast and easily integrable into commercial stringing machines. Four different methods to transform commercially available straight copper wire interconnectors with a round cross-section and a solder coating into wave-shaped wires were analyzed. On the one hand, key factors that describe the quality of the used method to reshape a wire interconnector were analyzed; the reproducibility, the homogeneity of the shape, and the amount of damaging (grooves, diameter changes, etc.). On the other hand, the mechanical, as well as the electrical properties of wave-shaped wires, modified by two different reshaping methods, were investigated in detail.

5.1.1 Method 1: Toothed racks

The first method to transform a straight into a wave-shaped wire uses two toothed racks. A straight wire interconnector has to be positioned in between the toothed racks and by pressing them together the shape of the wire is changed. Figure 5.1 shows a schematic drawing, as well as a photograph of Method 1. The reshaping tests with Method 1 revealed two major problems. First, to produce wave-shaped wires with well defined and homogeneous amplitudes is challenging. Second, the longer the length of the toothed racks the more inhomogeneous gets the amplitude. This can be explained by high forces required for the reshaping process and a difficult adjustment of the distance of the two toothed racks. In addition, parts of the wire interconnector are significantly stretched during the reshaping. This causes strain hardening, diameter changes, and, for large amplitudes, the wire interconnectors

tend to break, which is shown by Figure 5.2. Consequently, Method 1 is not taken into consideration for further experiments.

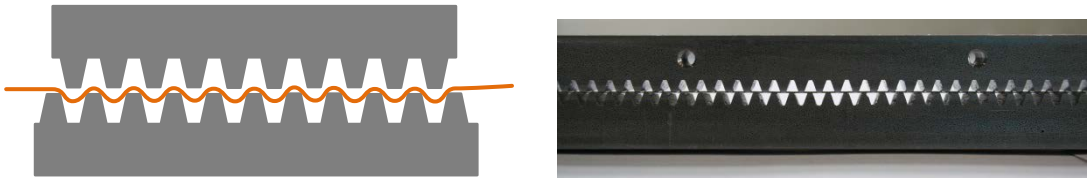

(a) (b)

Figure 5.1: Wave-shaping with Method 1: (a) schematic drawing and (b) photograph of the wire deformation using two toothed racks.

Figure 5.2: Multiple breakage of the copper wire when using wave-shaping Method 1 (toothed rack, width: 10 mm).

5.1.2 Method 2: Toothed wheel and toothed rack

For the second method to transform straight into wave-shaped wires one toothed wheel and one toothed rack was used. The wire interconnector has to be positioned on the toothed rack and the toothed wheel is rolled over the wire, pressing parts of it into the periodic spacings. Figure 5.3 shows a schematic drawing and a photograph of Method 2.

This method requires lower operating forces because a successive deformation is performed instead of a reshaping of a wire interconnector in one step. Furthermore, with Method 2 it was possible to manufacture wave-shaped wires with homogeneous amplitude. Figure 5.4 shows the laboratory wave-shaping machine for Method 2 (Machine 1) using a height-adjustable base plate (distance adjustable plate) on which the toothed rack is mounted. In addition, the toothed wheel is mounted on a manual slider.

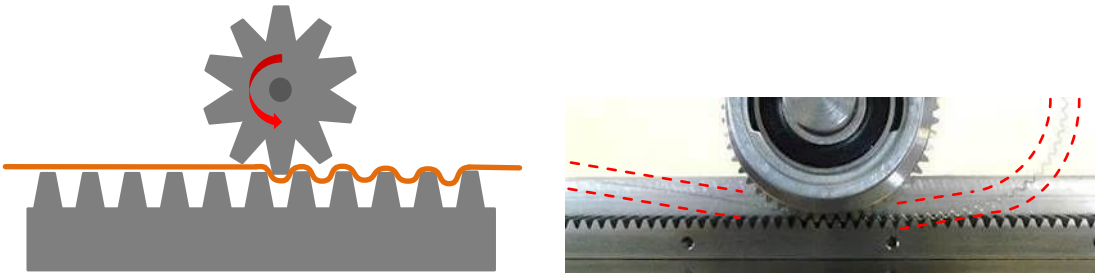

(a) (b)

Figure 5.3: Wave-shaping with Method 2: (a) schematic drawing and (b) photograph of the wire deformation using one toothed rack and one toothed wheel. A bowing of the resulting wave-shaped wire is visible.

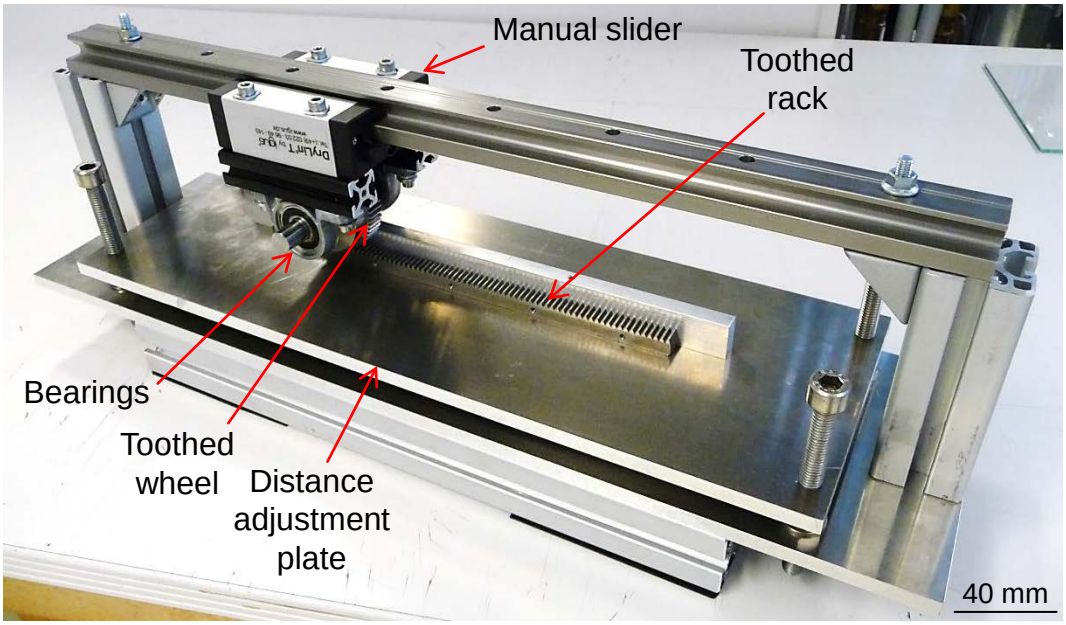

Figure 5.4: Photograph of Machine 1 to test wave-shaping using Method 2 (toothed wheel + toothed rack).

Disadvantages of Method 2 are that a wire interconnector is still stretched significantly, which causes strain hardening of the copper core and an increase of the electrical resistance of a wire interconnector, and that the resulting wave-shaped wires show significant bowing, which is also shown by Figure 5.3 (b). For these reasons, also Method 2 was not used for further experiments.

5.1.3 Method 3: Toothed wheels

To further reduce wire stretching and to avoid bowing Method 3 uses two toothed wheels. The wire interconnector is reshaped between the two toothed wheels as shown by Figure 5.5, which shows a schematic drawing, as well as a photograph of the deformation process. In the first approach one toothed wheel was manually rotated while the second could rotate independently. Machine 2 works with the described approach and is shown in Figure 5.6.

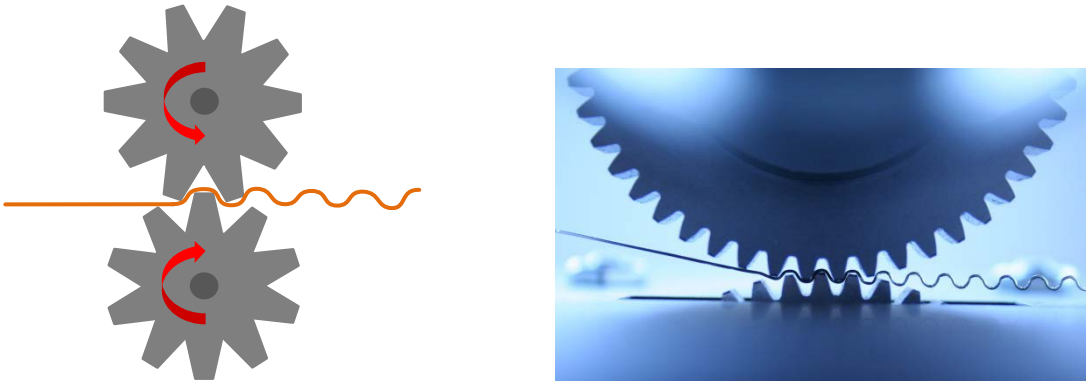

(a) (b)

Figure 5.5: Wave-shaping with Method 3: (a) schematic drawing and (b) photograph of the wire deformation using 2 toothed wheels.

Tests revealed that it is disadvantageous having only one directly driven toothed wheel. A wire interconnector is compressed between two teeth of the opposing toothed wheels, which results in wire damaging, such as grooves, diameter reduction, et cetera.

An improved second version of the setup was developed using two toothed wheels rotated simultaneously and inversely by the operator. Machine 3 works with the

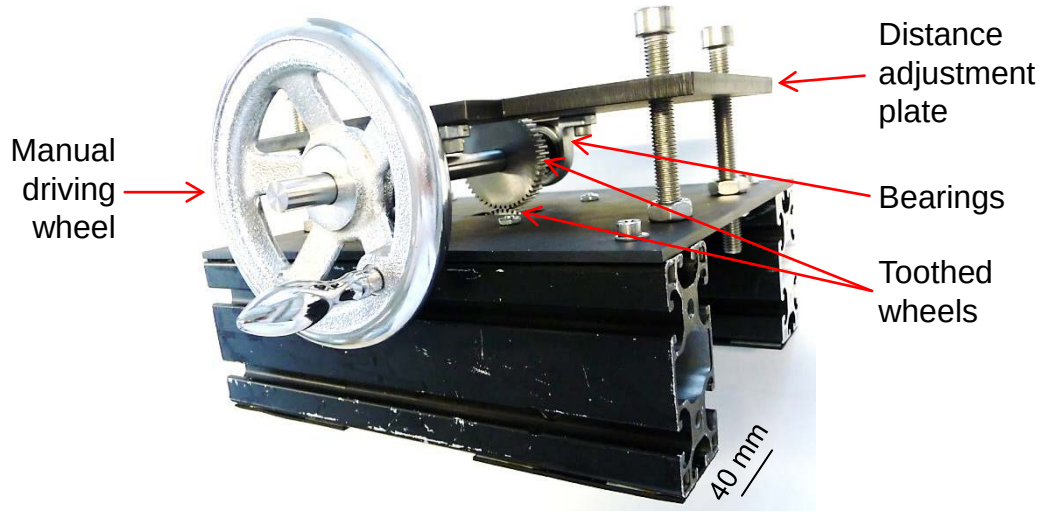

Figure 5.6: Photograph of Machine 2 to test wave-shaping using Method 3 (toothed wheel + toothed wheel).

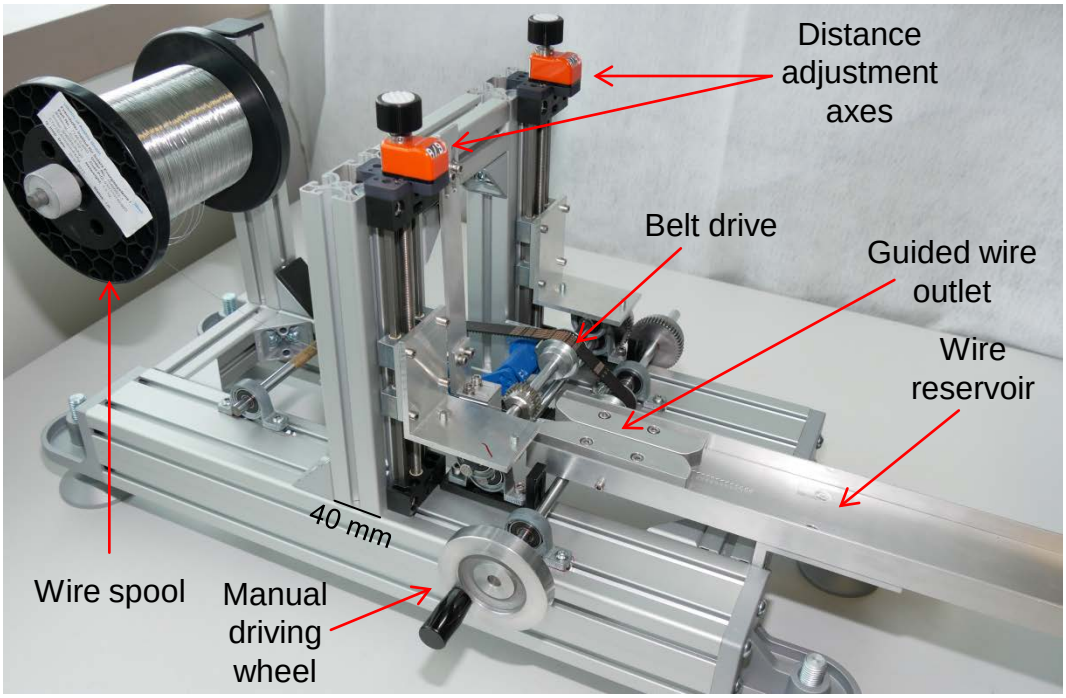

Figure 5.7: Photograph of Machine 3 (improved setup of Machine 2) to test wave-shaping using Method 3 (toothed wheel + toothed wheel)

improved approach and is shown by Figure 5.7. In addition, Figure 5.8 indicates details that describe the setup and working principle of Machine 3.

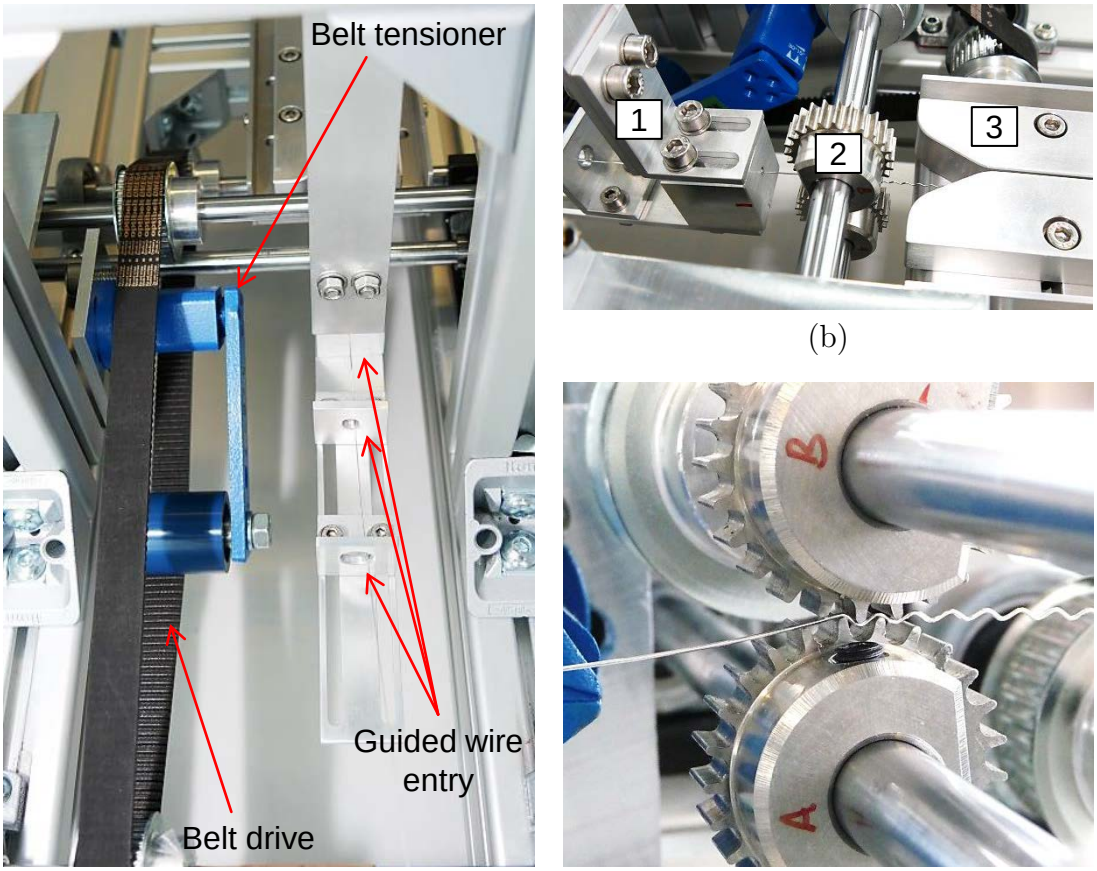

Figure 5.8: Details of Machine 3 showing (a) the belt drive to move both toothed wheels simultaneously and inversely, as well as the wire guidance before the shaping process, (b) a top view on the wire guidance inlet (1), the toothed wheels (2), and the guided wire outlet (3), and (c) a wire interconnector that is shaped between two optimized toothed wheels.

Additionally, new toothed wheels were designed, having an adapted teeth shape without sharp edges, resulting in less damaging of the wire interconnectors in the deformation process and enabling larger wire amplitudes. A comparison of commercially available and optimized toothed wheels is shown by Figure 5.9.

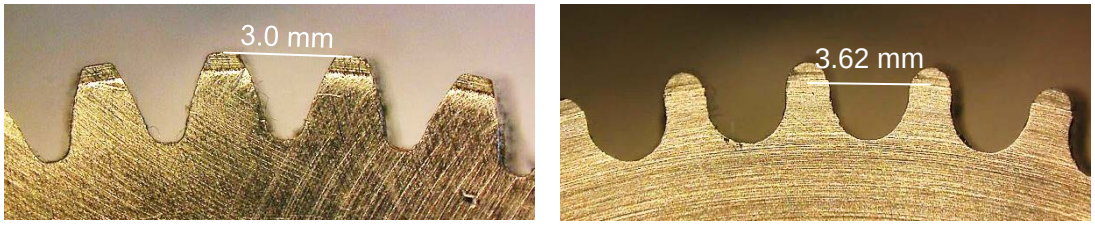

(a) (b)

Figure 5.9: Microscopic image of the toothed wheels: (a) commercially available toothed wheel with typical tooth shape, as well as (b) newly designed toothed wheels with optimized shape for less wire damaging and larger maximum wave amplitudes.

Method 3 enabled manufacturing wave-shaped wires with different amplitudes and periods. Figure 5.10 shows exemplary microscopic images of wave-shaped wires with amplitudes between 0.64 and 2.02 mm and periods of 1.5 and 3.0 mm.

In the deformation process with Method 3 several problems may occur. For example, the alignment, especially the relative positions of the two toothed wheels, influence the wire shape and have to be controlled accurately. Figure 5.11 shows exemplary microscopic images of damages (grooves, diameter change, etc.) and an inaccurate wire shape, which both should be avoided.

Microscopic images of the longitudinal cross-section, etched for 10 minutes in a Klemm 3 etching solution [134], enabled to determine the influence of reshaping on the grain structure of a copper-based wire interconnector. The grain structure

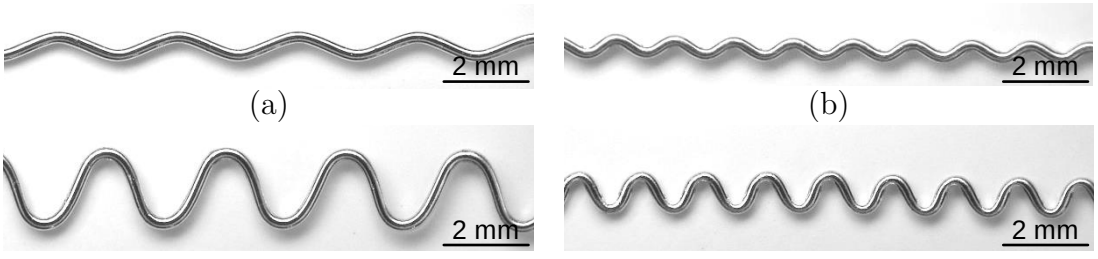

(a) (b)

(c) (d)

Figure 5.10: Microscopic images of exemplary wave-shaped wires manufactured with Method 3: (a) period: 3.0 mm, amplitude: 0.78 mm; (b) period: 3.0 mm, amplitude: 2.02 mm; (c) period: 1.5 mm, amplitude: 0.64 mm; (d) period: 1.5 mm, amplitude: 1.023 mm [133].

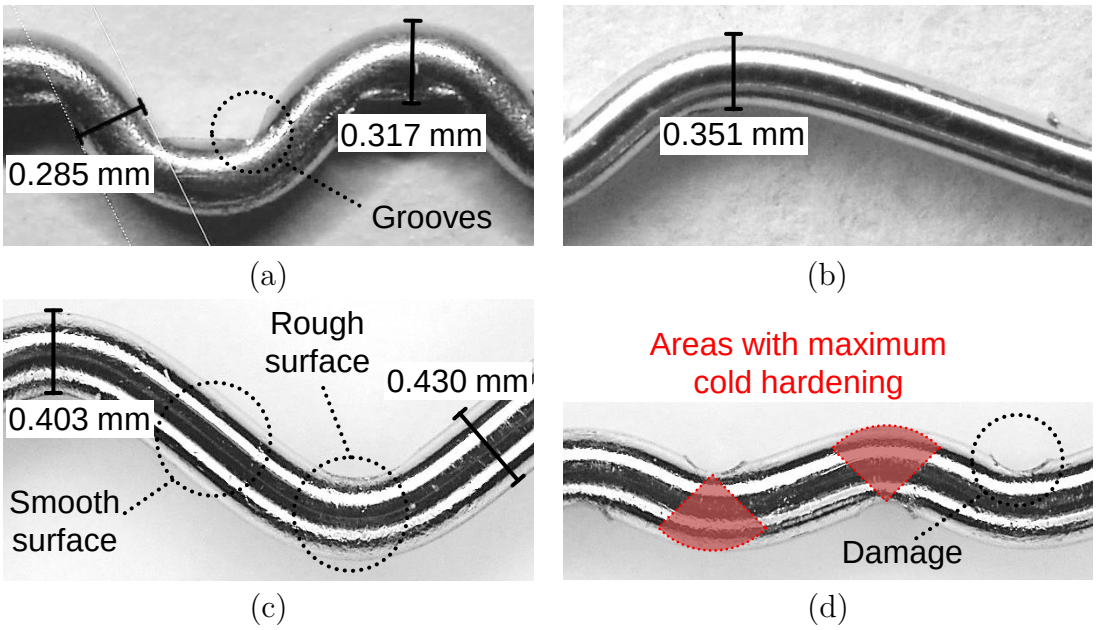

Figure 5.11: Potential damages as results of wave-shaping of copper-based wire interconnectors with solder coating: (a) change of the diameter, as well as grooves, (b) asymmetric wave shape caused by an imprecise reshaping process, (c) surface and diameter changes, and (d) surface damage (pressure marks). In addition, areas are indicated that show maximum optical surface changes in areas with most strain hardening [133].

indicates which areas are mainly affected by the reshaping and where the material properties are significantly changed. Figure 5.12 shows the cross-section of an exemplary wave-shaped wire (amplitude: 1.0 mm, period: 3.0 mm) manufactured by Method 3. The image reveals that there is strain hardening (grain refinement) in the areas where a wire interconnector was bent around the tooth of a toothed wheel, but in most parts the influence on the grain structure is negligible.

5.1.4 Method 4: Bending elements and feeding wheels

In the following experiments mainly Method 3 was used. However, a fourth approach was tested to determine whether a further reduction of wire damaging would be possible. In addition, this method is able to reshape many wire interconnectors in parallel, presumably has lower space requirements, and can potentially be integrated

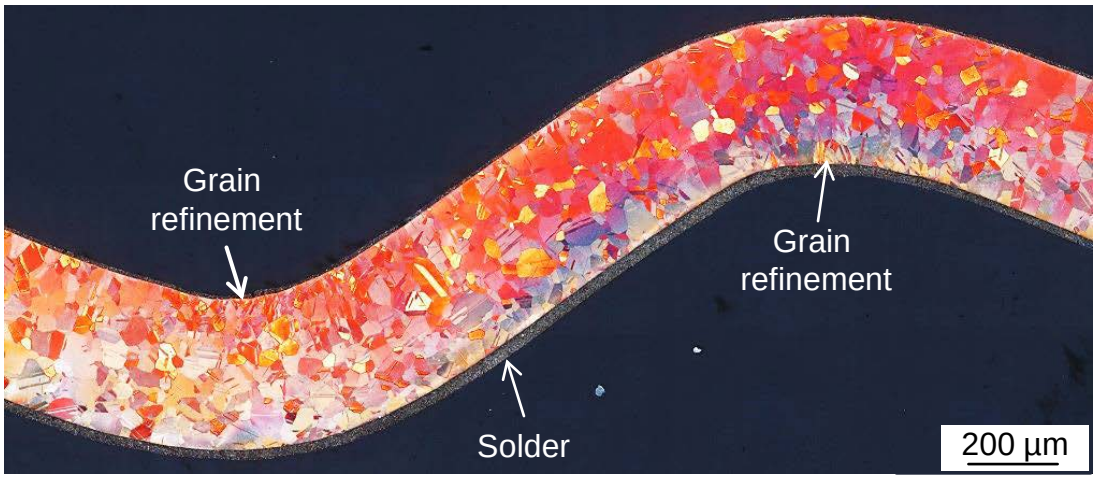

Figure 5.12: Longitudinal section of a wave-shaped wire with a diameter of 350 µm, a period of 3.0 mm and an amplitude of 1.0 mm [135]. Grain boundaries are visible due to 10 minutes etching with a chemical solution called Klemm 3 [134].

in industrial stringing machines. No toothed racks or wheels are used for Method 4. The wire interconnector is successively reshaped by two alternating process steps. The first step is to move the wire forward in a channel using feeding wheels. The second step is bending the wire with bending elements that move relatively to a channel outlet. This approach enables the manufacturing of wave-shaped wires with different amplitudes and periods without re-designing and/or replacing toothed wheels. In addition, Method 4 has the potential for reshaping wire interconnectors with minimized stretching, as well as insignificant diameter change and strain hardening. Additionally, parallel reshaping of several wire interconnectors by using higher numbers of bending elements and wire channels is possible. For these reasons, a patent application was prepared for this method which is currently pending [136]. The test setup can be further optimized and is still under development. The software based on LabView controls the electrical parts: the bending elements mounted on an electrical axis as well as the feeding wheel connected to an electrical motor. The working principle is concisely described by Figure A.8 in the appendix. However, with the current wave-shaping machine setup for Method 4 (Machine 4) the maximum amplitude is 1.1 mm with a minimum period of 3.6 mm. Figure 5.13 shows a schematic drawing of the wire deformation with Method 4 and photographs of the experimental

test setup (Machine 4) that describe the working principle in detail. A schematic drawing of the single steps used for the wave-shaping process is described in detail by Figure A.7 in the appendix.

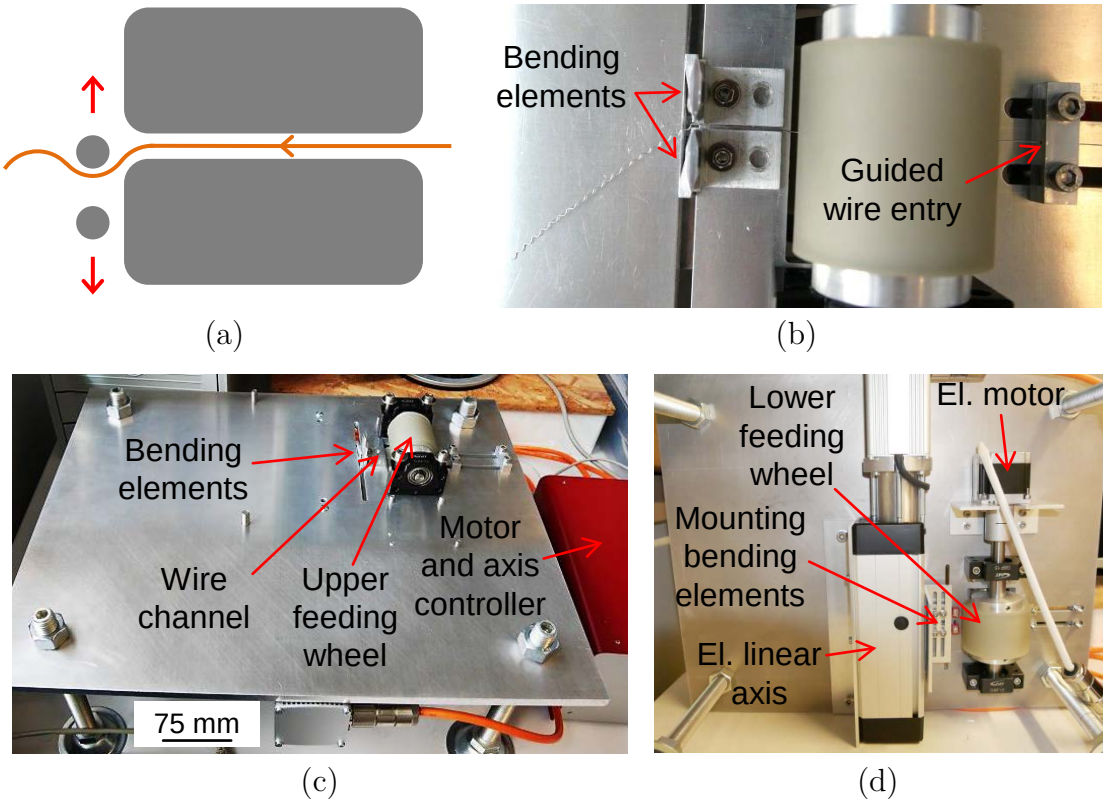

Figure 5.13: Wave-shaping with Machine 4 using Method 4 (bending elements + feeding wheels): (a) schematic drawing of the method (for schematic drawing of the single steps see Figure A.7 in the appendix), (b) detailed view on a wire interconnector in the wave-shaping process showing the upper feeding wheel, the wire channel and the bending elements, (c) top view on the test machine showing the upper feeding wheel, the motor and axis controller, the position of the wire inlet channel and the bending elements, as well as (d) bottom view of the wave-shaping machine showing the lower feeding wheel, the electrical axis and motor, and the mounting of the bending elements below the base plate.

5.2 Characterization and properties

5.2.1 Experiment description

The geometry, as well as the mechanical and electrical properties of different wave-shaped wires were investigated [133]. For the mechanical characterization tensile tests were performed according to the test standard for metallic materials [127]. Subsequently, the measured force-elongation curve is analyzed by a self-written software tool that determines the yield limit automatically (MATLAB code included in the appendix Section A.2) [133]. For the electrical characterization the length change, as well as the electrical resistance is measured. In a first experiment, wave-shaped wires with diameters of 300, 350, and 400 µm and periods of 1.5 and 3.0 mm were characterized. In a following second experiment, Method 3 and 4 were used to manufacture wave-shaped wires with a diameter of 350 µm, a period of 3.6 mm, and various amplitudes. Using Method 3, the maximum amplitudes of wave-shaped wires in the test - avoiding damaging visible by the naked eye - were 1.023 mm for a period of 1.5 mm, 2.056 mm for a period of 3.0 mm, and 2.125 mm for a period of 3.6 mm. Microscopic images revealed how precise a nominal amplitude can be realized by using Method 3 and 4. Table 5.1 shows the amplitude of wave-shaped wires manufactured by Method 3 with different diameters (300, 350, and 400 µm) and periods (1.5 and 3.0 mm), as well as the deviation of the measured amplitude from the particular target value, which is called nominal amplitude. The results show a deviation of the amplitudes between −2.4% and +6.5% for wires with a period of 1.5 mm and between −3.0% and +2.8% for wires with a period of 3.0 mm.

Table 5.1: Nominal, measured, and relative amplitude deviation of wave-shaped wires with different diameters and periods of 1.5 and 3.0 mm after the reshaping process using Method 3.

Diameter	**Period**	**Nominal amplitude**	**Measured amplitude**	**Relative deviation**
[µm]	[mm]	[mm]	[mm]	[%]
300	1.5	0.6	0.639	+6.5
		0.8	0.842	+5.2
		1.0	1.023	+2.3
	3.0	0.8	0.776	−3.0
		1.0	0.992	−0.8
		1.2	1.218	+1.5
		1.5	1.521	+1.4
		2.0	2.024	+1.2
350	1.5	0.6	0.615	+2.5
		0.8	0.838	+4.7
		1.0	1.000	+0.0
	3.0	0.8	0.786	−1.8
		1.0	1.001	+0.1
		1.2	1.217	+1.4
		1.5	1.524	+1.6
		2.0	2.056	+2.8
400	1.5	0.6	0.603	+0.5
		0.8	0.802	+0.3
		1.0	0.976	−2.4
	3.0	0.8	0.813	+1.6
		1.0	1.002	+0.2
		1.2	1.203	+0.3
		1.5	1.531	+2.1
		2.0	2.033	+1.7

Furthermore, wave-shaped wires with a maximum amplitude of approximately 1.1 mm for a period of 3.6 mm were possible to manufacture using the current experimental setup to test Method 4. The relative deviation of the amplitudes was between −1.6% and +2.6%. Table 5.2 shows the amplitudes for wave-shaped wires with a period of 3.6 mm manufactured by Method 3 and 4.

Table 5.2: Nominal, measured, and relative amplitude deviation of wave-shaped wires with different diameters (period of 3.6 mm) after reshaping by Method 3 and 4.

Method	**Diameter**	**Period**	**Nominal amplitude**	**Measured amplitude**	**Relative deviation**
	[µm]	[mm]	[mm]	[mm]	[%]
3	350	3.6	0.8	0.814	+1.8
			1.0	1.029	+2.9
			1.2	1.213	+1.1
			1.5	1.496	−0.3
			2.0	2.125	+6.3
4	350	3.6	0.8	0.800	+0.0
			1.0	1.026	+2.6
			1.1	1.082	−1.6

5.2.2 Mechanical characterization

To analyze the mechanical properties of wave-shaped wires tensile tests according to the test standard for metallic materials (ISO 6892-1) were performed [127]. A sensor was used to measure the force during longitudinal deformation of a wave-shaped wire. The wave-shaped wire was straightened and the copper material was stretched at the same time. For this reason, instead of the commonly used expression strain, the lengthening is referred to as relative elongation. Furthermore, there is tensile and compressive stress in a wave-shaped wire when it is straightened. The outer surface material in the peaks of wave-shaped wires is compressed while the inner surface material is stretched during straightening. In addition, stretching of the copper material causes tensile stress. Hence, the stress distribution in wave-shaped

wires during a tensile test is expected to be non-homogeneous and the measured force cannot be easily transformed into a homogeneous stress level in the wire cross section. Consequently, instead of the typical stress-strain curves the force-rel. elongation curves of wave-shaped wires were analyzed. The influence of the wave-shaping on the force-rel. elongation curve of an interconnector was determined. Figure 5.14 shows the behavior of a straight and a wave-shaped wire in the tensile test.

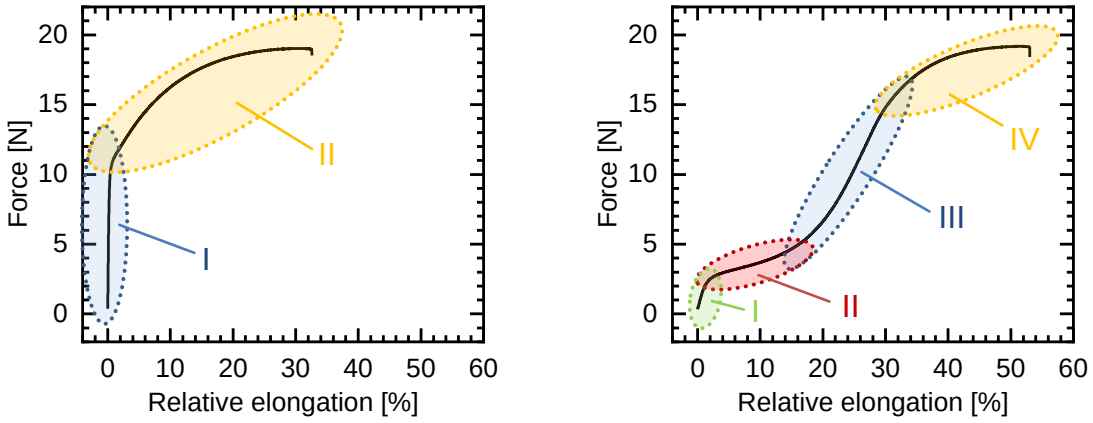

Figure 5.14: Force-rel. elongation curves of (a) a straight and (b) a wave-shaped wire. For the straight wire interconnector, the regions where predominantly elastic deformation (I, blue) and where predominantly plastic deformation (II, orange) occurs are indicated. A wave-shaped wire shows four regions of predominant deformation; elastic wire straightening (I, green), plastic wire straightening (II, red), elastic material deformation (III, blue), and plastic material deformation (IV, orange) [133].

The force-rel. elongation curve of the straight wire interconnector shows two areas; the elastic area (I) where the deformation is predominantly reversible, whereas in the plastic area (II) the deformation is predominantly irreversible. The force-rel. elongation curve of a wave-shaped wire indicates four areas; elastic wire straightening (I), plastic wire straightening (II), elastic material stretching (III), and plastic material stretching (IV). The areas of the measured curves only indicate the dominant deformation mode and include portions of other deformation modes.

Presumably, the maximum relative stretching of an interconnector in a solar module never exceeds 5% [30]. For this reason, the mechanical behavior of wires is only analyzed between 0% and 5% relative elongation. The main important characteristic values of an interconnector in a PV module are the Young's modulus and the yield limit. The lower these parameters are, the lower is the thermomechanical stress in the interconnections caused by the CTE mismatch. To determine the Young's modulus and the yield limit of an interconnector a detection algorithm was developed [133]. The software automatically finds an approximation line for the linear region at the beginning of the force-rel. elongation curve. Subsequently, this linear approximation is shifted by 0.2% and the cross-section with the force-rel. elongation curve delivers the 0.2% yield force ($F_{\mathrm{p0.2}}$) of the interconnector. For wave-shaped wires two yield limits exist; the first is a pseudo yield limit, because primarily the geometry is changed. The second one is where the material changes from elastic to plastic deformation, which, for wave-shaped wires, occurs at very high elongation levels larger than 5% and which is not taken into account in the following analysis. Figure 5.15 outlines graphically how the $F_{\mathrm{p0.2}}$ of an interconnector is determined.

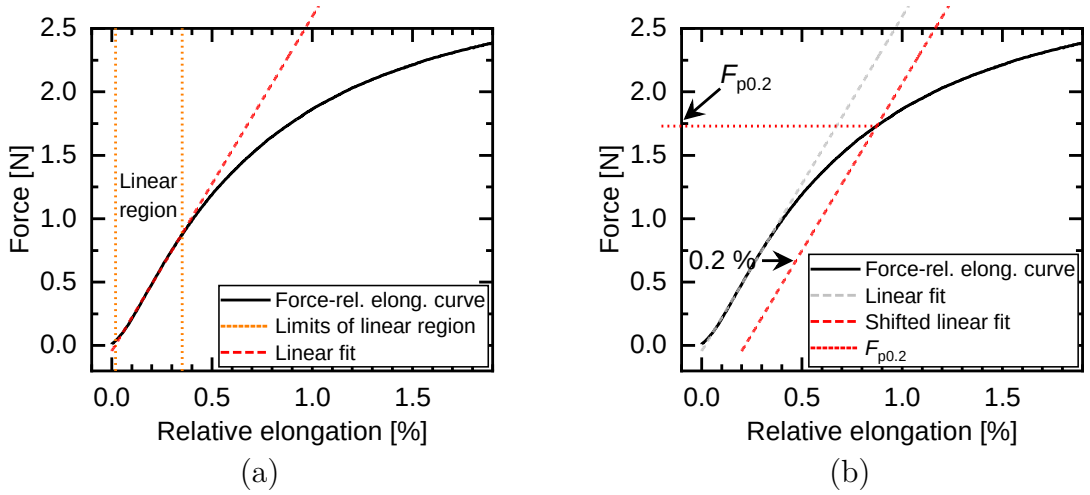

Figure 5.15: (a) Diagram with an example that shows the detection of the linear region, as well as a linear fit of the force-rel. elongation curve of a wave-shaped wire. (b) Example diagram that shows how the 0.2% yield force $F_{\mathrm{p0.2}}$ of a wave-shaped wire was determined [133].

As indicated by Figure 5.14 the mechanical properties are significantly influenced by the deformation of a wire interconnector. Comparing the force-rel. elongation curve (between 0% and 5% rel. elongation) of a straight wire interconnector and wave-shaped wires with different amplitudes reveals that the higher the amplitude is, the lower is the pseudo yield limit, which is shown by Figure 5.16 (a).

5.2.2.1 Method 3: Wire samples with periods of 1.5 and 3.0 mm

Figure 5.16 (a) shows the force-rel. elongation curves for wire interconnectors with an amplitude between 0 and 2.024 mm (diameter: 300 µm, period: 3.0 mm). Furthermore, the pseudo yield limit in Newton ($F_{p0.2}$) of wave-shaped wires with core diameters of 300, 350, and 400 µm, periods of 1.5 and 3.0 mm, and amplitudes up to 2.056 mm is indicated by Figure 5.16 (b).

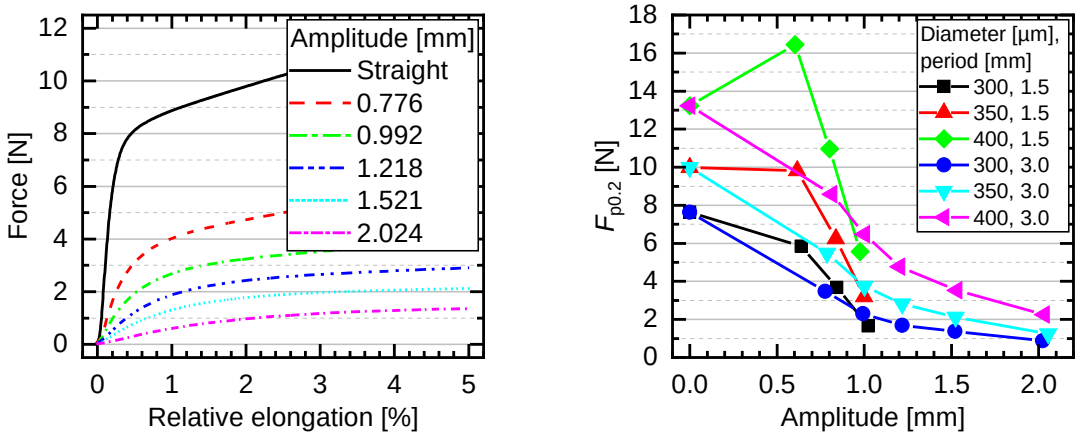

Figure 5.16: (a) Force-rel. elongation curves of a straight wire interconnector with a 300 µm copper core and five wave-shaped wires with different peak-to-peak amplitudes between 0.78 and 2.024 mm and a period of 3.0 mm, as well as (b) detected $F_{p0.2}$ (mean value of six samples per configuration) of straight, as well as wave-shaped wires with peak-to-peak amplitudes between 0.60 and 2.056 mm, periods of 1.5 or 3.0 mm, and three different diameters (300, 350, and 400 µm) [133].

The results show that the diameter influences the $F_{p0.2}$ significantly; the larger the diameter, the higher the $F_{p0.2}$. The initial $F_{p0.2}$ of straight wire interconnectors with diameters of 300, 350, and 400 µm are 7.64, 9.99, and 13.23 N. For one wire configuration (diameter: 400 mm, period: 1.5 mm, amplitude: 0.602 mm) there is an increase of the $F_{p0.2}$ that can be explained by significant cold-hardening of the wire material. In this special case, damaging and cold-hardening outperforms the softening effect of the wavy shape. Typically, the wire configurations show a significant reduction of the $F_{p0.2}$ up to -88.5%. For amplitudes larger than 0.9 mm the $F_{p0.2}$ of wave-shaped wires with a period of 1.5 mm is potentially lower compared to wave-shaped wires with a period of 3.0 mm. However, significant damaging can be expected for larger amplitudes with a period of 1.5 mm.

Table 5.3 shows the mean value of the $F_{p0.2}$ of wave-shaped wires (six samples per configuration) with different diameters (300, 350, and 400 µm), periods (1.5 and 3.0 mm) and amplitudes (between 0.603 and 2.056 mm). In addition, the relative change of the $F_{p0.2}$ for a wave-shaped wire compared to a straight wire interconnector is indicated.

5.2.2.2 Comparison of Method 3 and 4: Wire samples with periods of 3.0 and 3.6 mm

Wave-shaped wires with a period of 3.6 mm were manufactured using Method 3 and 4 to compare their mechanical properties. For the wave-shaped wire samples manufactured by Method 3 wire material from a first wire batch with a mean $F_{p0.2}$ of 9.99 N were used, whereas for the samples manufactured by Method 4 wire material of the second batch with a mean $F_{p0.2}$ of 9.51 N was used. Figure 5.17 (a) shows a top view on Machine 4 using Method 4 while reshaping a wire sample. Furthermore, Figure 5.17 (b) indicates the $F_{p0.2}$ of wave-shaped wires manufactured by Method 3 and 4. For Method 3 different copper core diameters of 300, 350, and 400 µm, periods of 3.0 and 3.6 mm, and amplitudes up to 2.125 mm are included. For Method 4 wave-shaped wires with a copper core diameters of 350 µm, a period of 3.6 mm, and amplitudes up to 1.082 mm are shown.

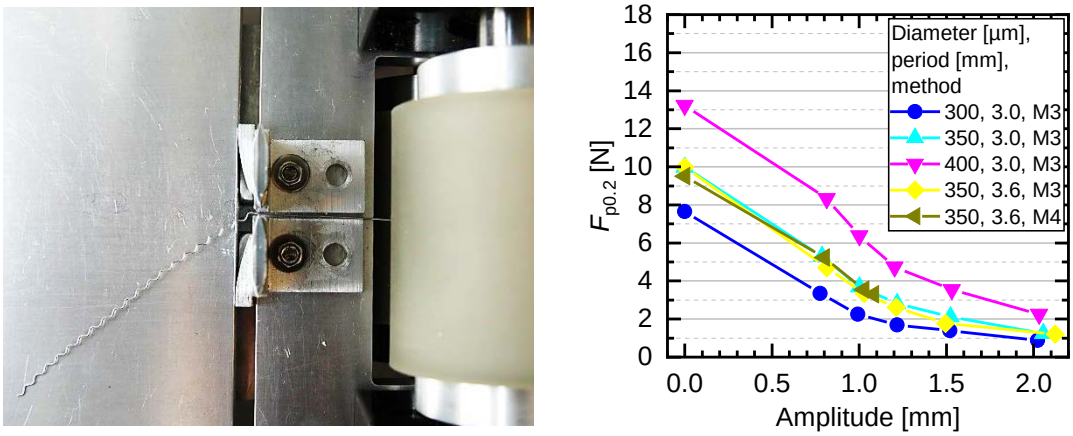

(a) (b)

Figure 5.17: (a) Wave-shaping process by Method 4 with Machine 4, as well as (b) the detected $F_{p0.2}$ (mean value of six samples per configuration) of straight, as well as wave-shaped wires manufactured by Method 3 and 4, with copper core diameters of 300, 350, and 400 µm, peak-to-peak amplitudes between 0.776 and 2.125 mm, and periods of 3.0 and 3.6 mm.

For both periods (3.0 and 3.6 mm) the measurement results show comparable $F_{p0.2}$ mean values of wave-shaped wires with a copper core diameter of 350 µm. In addition, the results indicate that the $F_{p0.2}$ values of wave-shaped wires manufactured by Method 3 and 4 are comparable. Table 5.4 shows the mean value of the measured $F_{p0.2}$ of wave-shaped wires (6 samples per configuration) with a diameter of 350 µm, but different periods (3.0 and 3.6 mm) and amplitudes (between 0.786 and 2.125 mm). In addition, the relative change of the $F_{p0.2}$ for wave-shaped wires compared to straight wire interconnectors is indicated.

Table 5.3: Mean values of the pseudo yield limit ($F_{p0.2}$) of wave-shaped wires with different diameters and periods, as well as its relative change compared to straight wire interconnectors [133].

Diameter	**Period**	**Amplitude**	**Pseudo yield limit** ($F_{p0.2}$)	**Relative change**
[µm]	[mm]	[mm]	[N]	[%]
300	Straight wire		7.64	
	1.5	0.639	5.78	−24.4
		0.842	3.67	−51.9
		1.023	1.65	−78.4
	3.0	0.776	3.35	−56.2
		0.992	2.25	−70.5
		1.218	1.69	−77.8
		1.521	1.38	−81.9
		2.024	0.88	−88.5
350	Straight wire		9.99	
	1.5	0.615	9.57	−4.2
		0.838	6.23	−37.7
		1.000	3.17	−68.2
	3.0	0.786	5.30	−46.9
		1.001	3.69	−63.1
		1.217	2.82	−71.8
		1.524	2.12	−78.8
		2.056	1.24	−87.6
400	Straight wire		13.23	
	1.5	0.603	16.07	+21.4
		0.802	10.99	−17.0
		0.976	5.51	−58.3
	3.0	0.813	8.33	−37.0
		1.002	6.38	−58.8
		1.203	4.74	−64.2
		1.531	3.54	−73.2
		2.033	2.25	−83.0

Table 5.4: Mean values of the pseudo yield limit ($F_{p0.2}$) of wave-shaped wires (diameter of 350 µm) with different amplitudes and periods manufactured with wave-shaping Method 3 and 4, and the relative $F_{p0.2}$ change compared to straight wire interconnectors.

Method	**Period**	**Amplitude**	**Pseudo yield limit** ($F_{p0.2}$)	**Relative change**
	[mm]	[mm]	[N]	[%]
	Straight wire batch 1		9.99	
3	3.0	0.786	5.30	−46.9
		1.001	3.69	−63.1
		1.217	2.82	−71.8
		1.524	2.12	−78.8
		2.056	1.24	−87.6
	3.6	0.814	4.71	−52.9
		1.029	3.35	−66.5
		1.213	2.62	−73.8
		1.496	1.77	−82.3
		2.125	1.20	−87.9
	Straight wire batch 2		9.51	
4	3.6	0.800	5.23	−45.0
		1.026	3.55	−62.7
		1.082	3.30	−65.3

5.2.3 Electrical characterization

The wave-shaping process changes the electrical properties of a wire interconnector. First, damaging of the wire as shown in Figure 5.11 increases the electrical resistance. Second, the reshaping process changes the length of a wire interconnector. When interconnecting solar cells with a certain size additional wire material is required and the electrical current path is longer. Damaging of the wire interconnector can be reduced by optimizing the wave-shaping process, but the length change is inevitable. To quantify these influence factors the length and the electrical resistance of straight (length between two markers of an initially straight wire (l_1), electrical resistance between two markers of an initially straight wire (R_1)) and of wave-shaped wires (length between two markers of a wave-shaped wire (l_2), electrical resistance between two markers of a wave-shaped wire (R_2)) were measured. Figure 5.18 shows schematically how the measurements were performed.

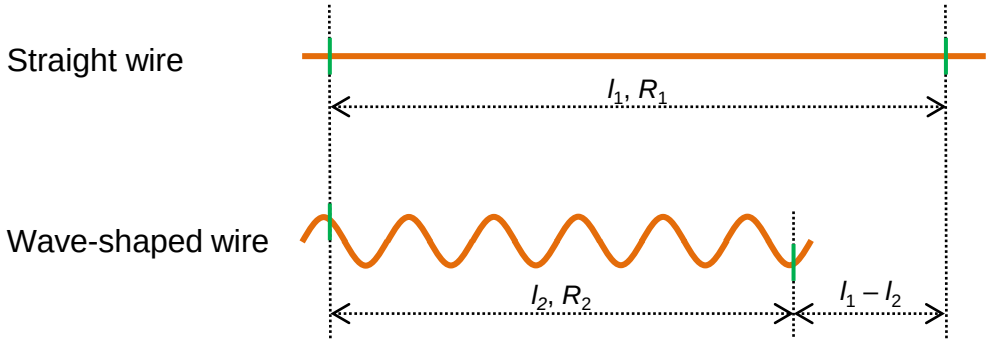

Figure 5.18: Measurement of the electrical properties of a wave-shaped wire compared to a straight wire interconnector. Characteristic values are length and electrical resistance between two markers of initial straight wire interconnectors (l_1, R_1), as well as of wave-shaped wires (l_2, R_2) [133].

Subsequently, three characteristic factors were calculated to describe the reasons for, and the amount of relative change of the electrical resistance: the relative change of the electrical resistance induced by damaging due to reshaping (f_D), the relative change of the length due to reshaping (f_L), and the overall relative change of the electrical resistance due to reshaping (f_W). The f_D (index D stands for "damage") of a wave-shaped wire is defined by

$$f_{\mathrm{D}} = \frac{R_2 - R_1}{R_1}, \tag{5.1}$$

where R_1 is the initial and R_2 is the electrical resistance between two markers after the wave-shaping process. The f_{L} (index L stands for "length") of a wire is defined by

$$f_{\mathrm{L}} = \frac{l_1 - l_2}{l_2}, \tag{5.2}$$

where l_1 is the initial length of the straight wire and l_2 is the length of the wave-shaped wire. It describes how much additional wire material is required and the increase of the electrical resistance caused by a longer current path.

Based on f_{D}, f_{L}, and the electrical resistance of a straight wire (R_{Straight}) the electrical resistance of a wave-shaped wire (R_{Wave}) can now be calculated by using

$$R_{\mathrm{Wave}} = R_{\mathrm{Straight}} \cdot (1 + f_{\mathrm{D}}) \cdot (1 + f_{\mathrm{L}}). \tag{5.3}$$

f_{D} and f_{L} can be combined to f_{W} (index W stands for "wave-shaped"), which is defined by

$$f_{\mathrm{W}} = (1 + f_{\mathrm{D}}) \cdot (1 + f_{\mathrm{L}}) - 1 = \frac{R_2}{R_1} \cdot \frac{l_1}{l_2} - 1. \tag{5.4}$$

This enables the calculation of the electrical resistance of a wave-shaped wire R_{Wave} by

$$R_{\mathrm{Wave}} = R_{\mathrm{Straight}} \cdot (1 + f_{\mathrm{W}}) = \rho \cdot \frac{l_1}{A_1} \cdot (1 + f_{\mathrm{W}}), \tag{5.5}$$

using the cross-sectional area of a wave-shaped wire (A_1) and the specific electrical resistance (ρ) of the interconnectors core material.

5.2.3.1 Method 3: Wire samples with periods of 1.5 and 3.0 mm

The results of f_D for wave-shaped wires manufactured by Method 3 show a significantly larger damaging for a wave period of 1.5 mm compared to 3.0 mm. An f_D up to 45.6% was determined, whereas for a period of 3.0 mm an f_D below 13.0% was measured. This difference can be explained by diameter changes and defects as shown in Figure 5.11. For wave-shaped wires with a period of 3.0 mm and amplitudes between 0.776 and 1.531 mm f_D is below 4.5%, which proves modest damaging by a gentle reshaping process using Method 3 (see Section 5.1.3). However, the results show small f_D differences for the different wire diameters with a period of 3.0 mm that demonstrate an increasing amount of defects for larger diameters. The maximum f_D for wave-shaped wires with a diameter of 300 µm and a period of 3.0 mm is 8.7% (amplitude: 2.024 mm), whereas for a diameter of 350 µm 11.4% (amplitude: 2.056 mm), and for a diameter of 400 µm 13.0% (amplitude: 2.033 mm) was measured (see Table 5.5 and Figure 5.19 (a)).

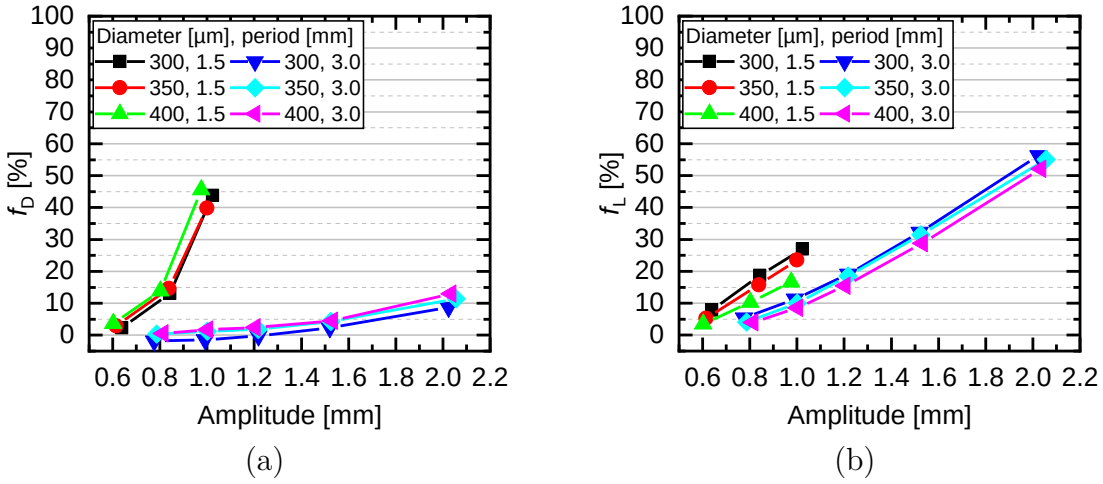

Figure 5.19: (a) f_D and (b) f_L of the different wave-shaped wire configurations. f_D describes the relative change of the electrical resistance induced by damaging and f_L shows the relative change of the length due to the reshaping [133].

As expected, the length measurement indicates an almost linear f_L increase with the amplitude. In addition, the f_L values are higher for a period of 1.5 mm compared to 3.0 mm. Figure 5.19 shows the results for the measurement of f_D and f_L of wave-shaped wires with peak-to-peak amplitudes between 0.60 and 2.056 mm, a period of

1.5 or 3.0 mm, and three different diameters (300, 350, and 400 µm). The calculated f_W values increase with the amplitude of the wave-shaped wire. Furthermore, wave-shaped wires with a period of 3.0 mm show significantly lower f_W values compared to a period of 1.5 mm. This is caused by both; higher f_D, as well as higher f_L values for wave-shaped wires with a period of 1.5 mm. For a period of 1.5 mm a maximum f_W of 82.7% was determined (diameter: 300 µm, amplitude: 1.023 mm), whereas the maximum f_W of wave-shaped wires with a period of 3.0 mm show a maximum f_W of 72.8% (diameter: 350 µm, amplitude: 2.056 mm). A comparison of the f_W values for different wire diameters indicates only small variations, which can presumably be explained by slight amplitude differences. Figure 5.20 shows the f_W values for different wire configurations. In addition, for each wire configuration the correlation of the f_W and the relative pseudo yield force reduction (see Table 5.3) is indicated. Table 5.5 shows f_D, f_L, and f_W of wave-shaped wires with different diameters (300, 350, and 400 µm) and periods (1.5 and 3.0 mm).

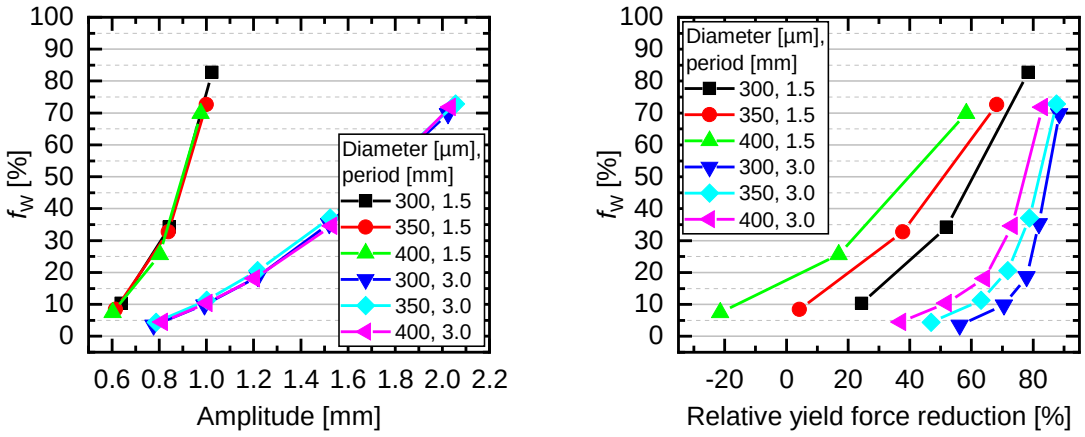

Figure 5.20: (a) f_W values that describe the overall relative change of the electrical resistance of wave-shaped wires manufactured by Method 3 compared to a straight wire interconnector for the different wire configurations and (b) correlation of the relative pseudo yield force reduction and the overall relative change of the electrical resistance [133].

Table 5.5: Influence factors f_D, f_L, and f_W describing the amount and reason for the relative resistance change for wave-shaped wires manufactured by Method 3 with different diameters and periods compared to straight wire interconnectors [133].

Diameter	**Period**	**Amplitude**	**Defect influence**	**Length change**	**Resistance change**
			f_D	f_L	f_W
[µm]	[mm]	[mm]	[%]	[%]	[%]
300	1.5	0.639	2.3	7.8	10.3
		0.842	13.1	18.7	34.2
		1.023	43.8	27.0	82.7
	3.0	0.776	−1.8	5.4	3.5
		0.992	−1.4	11.3	9.8
		1.218	−0.3	19.1	18.7
		1.521	2.3	32.2	35.3
		2.024	8.7	56.2	69.8
350	1.5	0.615	2.9	5.3	8.4
		0.838	14.7	15.7	32.7
		1.000	39.8	23.5	72.6
	3.0	0.786	0.3	4.1	4.4
		1.001	1.2	10.0	11.3
		1.217	1.8	18.5	20.6
		1.524	4.3	31.4	37.1
		2.056	11.4	55.1	72.8
400	1.5	0.603	3.7	3.5	7.4
		0.802	13.9	10.3	25.6
		0.976	45.6	16.6	69.9
	3.0	0.813	0.5	4.0	4.5
		1.002	1.7	8.5	10.4
		1.203	2.4	15.4	18.1
		1.531	4.5	28.8	34.6
		2.033	13.0	52.1	71.8

5.2.3.2 Comparison of Method 3 and 4: Wire samples with periods of 3.0 and 3.6 mm

Figure 5.21 (a) shows the f_D values of wave-shaped wires with a diameter of 350 µm, a period of 3.6 mm, and different amplitudes manufactured with Method 3 and 4. In addition, the f_D values of wave-shaped wires with diameters between 300 and 400 µm, a period of 3.0 mm, and different amplitudes manufactured by Method 3 are shown. A comparison of different periods for wave-shaped wires manufactured by Method 3 reveals significantly lower f_D values for a period of 3.6 mm. For wires with a diameter of 350 µm the maximum f_D is 2.2% for a wave-shaped wire with a period of 3.6 mm (amplitude: 2.125 mm) and 11.4% for a wave-shaped wire with a period of 3.0 mm (amplitude: 2.056 mm). This once again demonstrates that a larger period leads to more gentle reshaping with less wire damaging.

Furthermore, the f_D of wave-shaped wires with amplitudes up to 1.082 mm manufactured with Method 4 is shown (diameter: 350 µm, period: 3.6 mm). For the current wave-shaping machine setup (see Figure 5.13 and Figure 5.17 (a)) wave-shaped wires manufactured with Method 4 have approximately 1.6% higher f_D values compared to Method 3. This indicates that Method 4 can be further improved to induce less wire damaging.

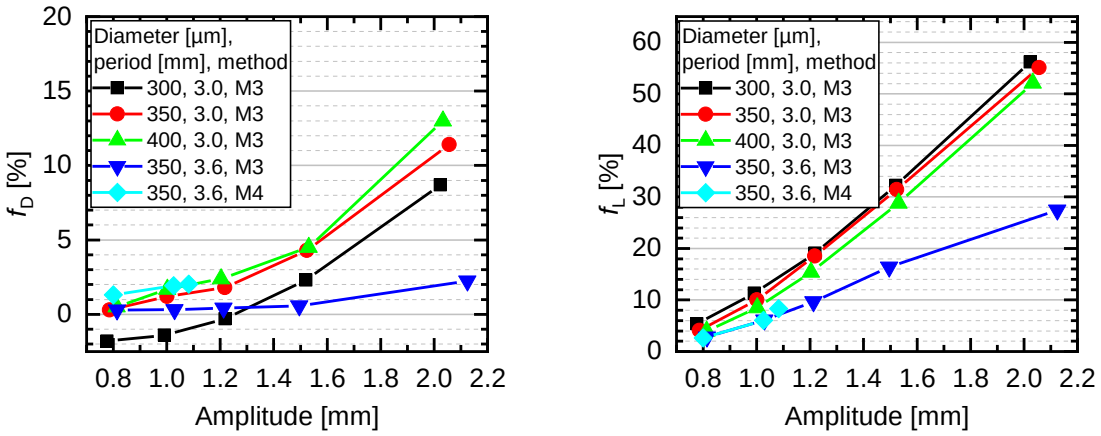

Figure 5.21: (a) f_D and (b) f_L of the different wave-shaped wire configurations manufactured by Method 3 and 4.

In addition, Figure 5.21 (b) shows the f_L values of the same configurations of wave-shaped wires. The results reveal significantly lower f_L values for wave-shaped wires manufactured by Method 3, with a period of 3.6 mm, with the same diameter (350 µm) and equivalent amplitudes, compared to wave-shaped wires with a period of 3.0 mm. Wave-shaped wires with an amplitude of 2.056 mm and a period of 3.0 mm show a mean f_L of 55.1%, whereas wave-shaped wires with an amplitude of 2.125 mm and a period of 3.6 mm show a mean f_L of 27.5%. Comparing the f_L of wave-shaped wires manufactured by Method 3 and 4 (diameter: 350 µm, period: 3.6 mm) with amplitudes between 0.800 and 1.213 mm reveals comparable values between 2.6% and 9.7% for both methods (see Table 5.6).

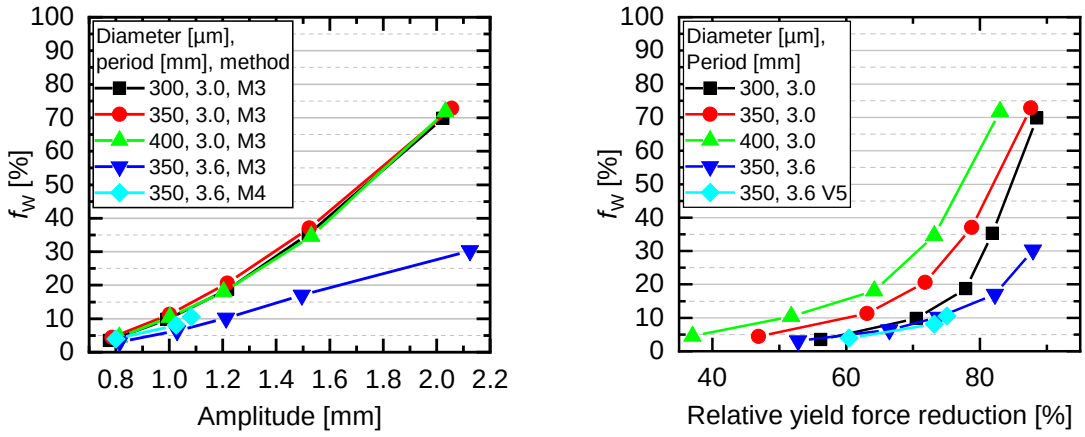

Figure 5.22: (a) f_W values of a wave-shaped wire manufactured by Method 3 and 4 compared to a straight wire interconnector for the different wire configurations; (b) correlation of the relative pseudo yield force reduction and the overall relative change of the electrical resistance.

Figure 5.22 shows the f_W values for different wire configurations manufactured by Method 3 and 4 calculated from the f_D and f_L values. In addition, for each wire configuration the correlation of the f_W and the relative pseudo yield force reduction (see Table 5.4) is indicated. Due to lower f_D and f_L values for wave-shaped wires manufactured by Method 3 lower f_W values between 3.1% and 30.3% for a period of 3.6 mm were measured, whereas comparable wires with a period of 3.0 mm show f_W values between 4.1% and 55.1%. The higher f_D values for wave-shaped wires

manufactured by Method 4 compared to Method 3 also lead to approximately 2% higher f_W values for amplitudes up to 1.082 mm. Table 5.6 shows f_D, f_L, and f_W of wave-shaped wires with a diameter of 350 µm, and different amplitudes and periods, manufactured by Method 3 and 4.

Table 5.6: Influence factors f_D, f_L, and f_W for wave-shaped wires manufactured by wave-shaping Method 3 and 4 with a diameter of 350 µm and different periods.

Method	**Period**	**Amplitude**	**Defect influence** f_D	**Length change** f_L	**Resistance change** f_W
	[mm]	[mm]	[%]	[%]	[%]
3	3.0	0.786	0.3	4.1	4.4
		1.001	1.2	10.0	11.3
		1.217	1.8	18.5	20.6
		1.524	4.3	31.4	37.1
		2.056	11.4	55.1	72.8
	3.6	0.814	0.3	2.8	3.1
		1.029	0.3	6.1	6.4
		1.213	0.4	9.7	10.2
		1.496	0.6	16.4	17.0
		2.125	2.2	27.5	30.3
4	3.6	0.800	1.3	2.6	4.0
		1.026	1.9	6.0	8.1
		1.082	2.0	8.3	10.5

6 Interconnection of solar cells by wave-shaped wires

6.1 Process description

Soldering of wave-shaped wires on silicon solar cells with small contacts instead of busbars, as well as on BC solar cells using a typical, industry-related IR soldering process was evaluated. The applied, semi-automatic soldering process is described in detail. The initial quality and the long-term stability of both types of silicon solar cells connected by wave-shaped wires were determined. In the first experiments, commercially available standard solar cells were connected by soldering wave-shaped wires on the contact finger grid on their front side. These experiments were performed for two reasons; first, there were no BC solar cells available at that time, and second, to determine whether the softening of the wires enables soldering on very small contacts. In the following second experiment, BC solar cells, developed at Fraunhofer ISE, were connected by wave-shaped wires. To detect interconnection defects EL measurements were performed showing initial defects of interconnections or cracks in the silicon solar cells. Furthermore, accelerated temperature cycling (aTC) tests were performed (combined with EL and IV measurements) to determine the long-term stability of silicon solar cells connected by wave-shaped wires.

To heat up a solar cell above the melting point of the used solder lamps that emit IR light were used. In addition, a vacuum hotplate heated up the solar cell and the interconnectors to a base temperature below the melting point of the solder before further heating up the whole setup by the IR lamps. In between the vacuum hotplate and the solar cells a support-plate made of glass-fiber composite material was used, especially designed for a certain type and number of solar cells. The used support plate was also designed for a specific interconnection concept, with predefined numbers and sizes of slots for the used interconnectors. In addition, the support-plate provides holes for the vacuum to hold the cells. The solar cells were placed on top of the support plate with the interconnectors in between. Subsequently,

the vacuum was enabled and the solar cells were pressed on the interconnectors and the surface of the support-plate. Figure 6.1 shows a schematic drawing of the setup for single side soldering of silicon solar cells.

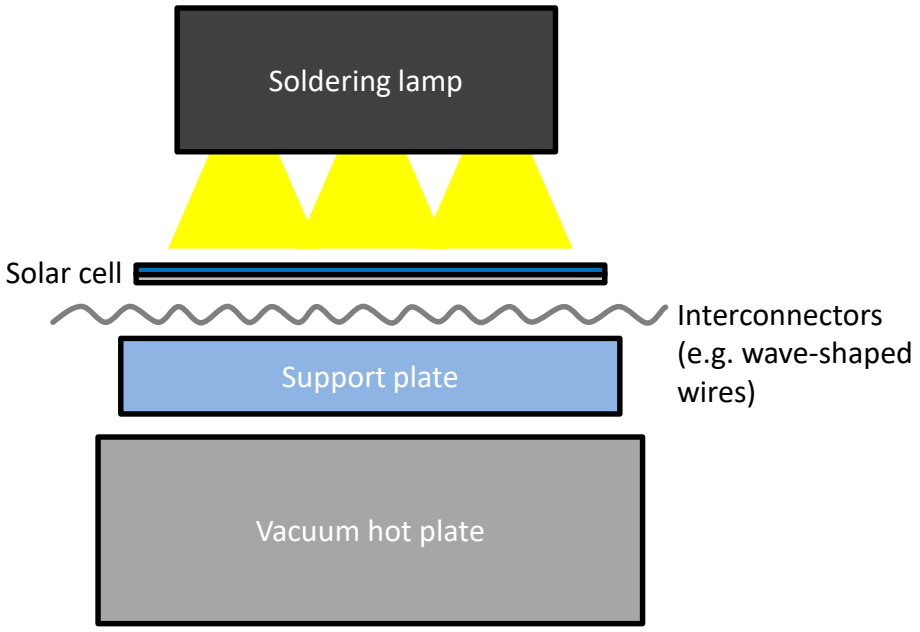

Figure 6.1: Setup used for single side soldering of interconnectors (e.g. wave-shaped wires) on BC solar cells by IR light.

An exemplary computer aided design (CAD) drawing of the used soldering setup is shown by Figure 6.2. With the current test setup 30 wave-shaped wires can be soldered on a maximum of four half solar cells (size: 78 mm × 156 mm). Figure 6.3 shows a photograph of the glass-fiber support-plate, two half solar cells, and 30 wave-shaped wires positioned in the wire slots, as well as a detail image indicating the vacuum holes in between the wire slots used to press the cell on the wave-shaped wires and the support-plate.

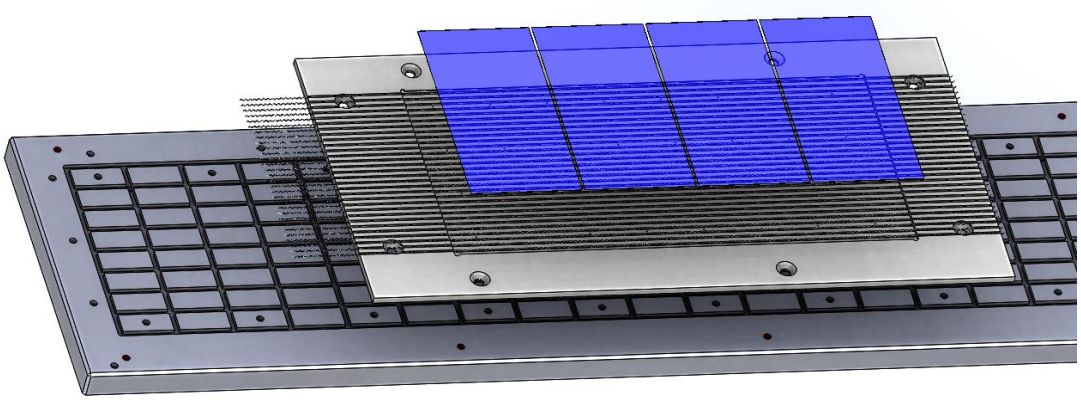

Figure 6.2: CAD drawing of the hotplate, the glass-fiber support plate, the wire interconnectors, and four half solar cells (size: 156 mm × 78 mm).

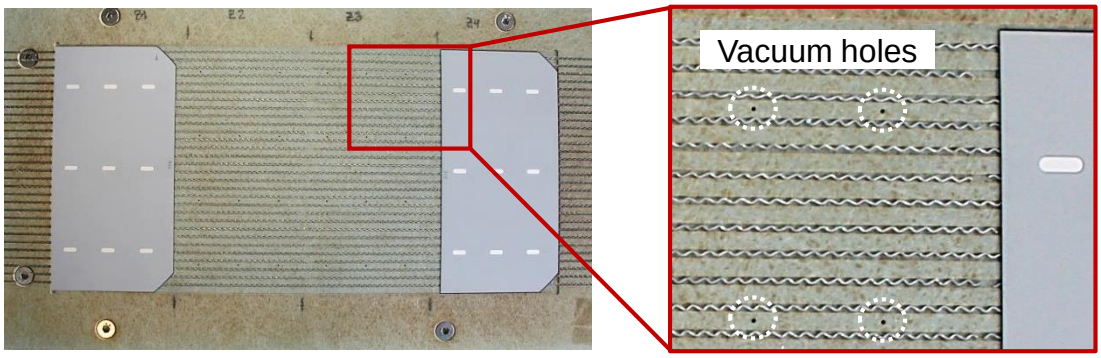

Figure 6.3: Glass-fiber support plate including vacuum holes, wave-shaped wires, and two half solar cells (size: 156 mm × 78 mm).

A photograph of the IR soldering station with the most important components is shown by Figure 6.4. The soldering lamp, a glass-fiber support plate for one full or two half solar cells, the vacuum hotplate, a rubber tube for sealing the vacuum area below the used support-plate, a pressure gauge to measure the vacuum, and a temperature controller are shown.

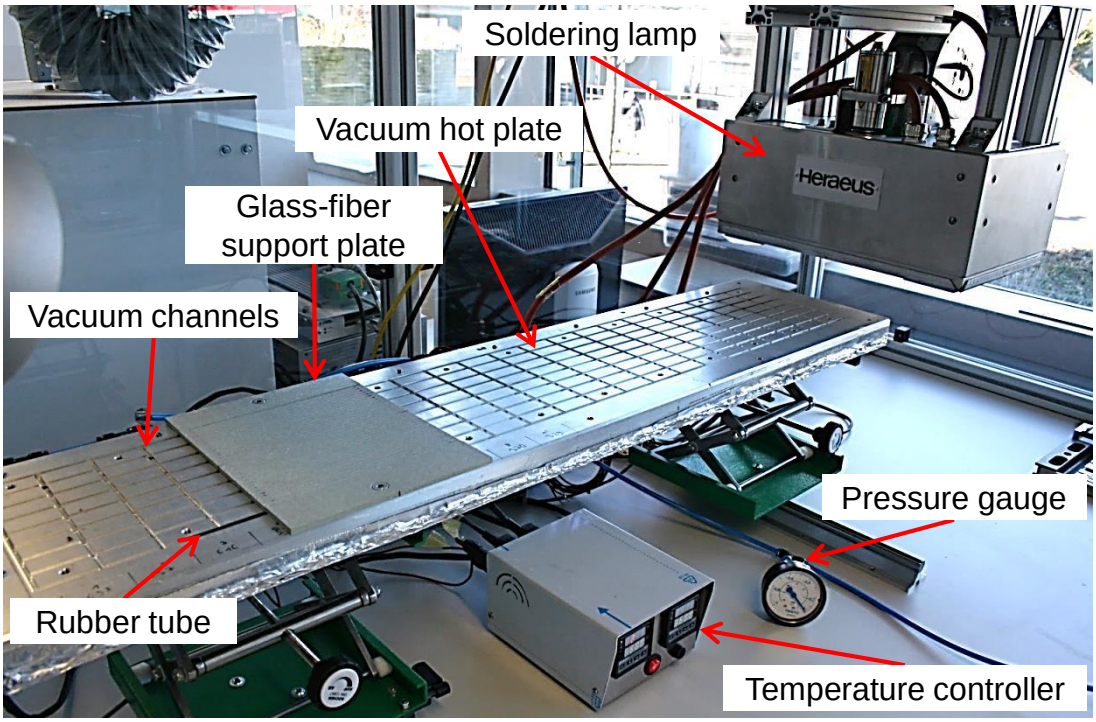

Figure 6.4: IR soldering station used for the interconnection of solar cells by wave-shaped wires.

6.2 Semi-automatic soldering on contact finger grid

6.2.1 Soldering specifics

Commercially available 6" solar cells with a common 3BB contact metallization layout were used to test soldering of wave-shaped wires on very small contacts. The width of the contact fingers on the front side of the used solar cells is between 50 and 70 µm (measured by optical profilometry with a confocal microscope). Figure 6.5 shows photographs of a standard solar cell connected by three ribbon interconnectors on the busbars (a), as well as an identical solar cell connected by 30 wave-shaped wires on the finger grid on the front side (b). The comparison of the solar cell deformation shows the significant reduction of the thermomechanical stress when

using wave-shaped wires instead of ribbon interconnectors. In addition, Figure 6.6 shows scanning electron microscope (SEM) measurements of wave-shaped wires soldered on the front finger grid of a solar cell which indicates that the solder alloy wets the contact fingers.

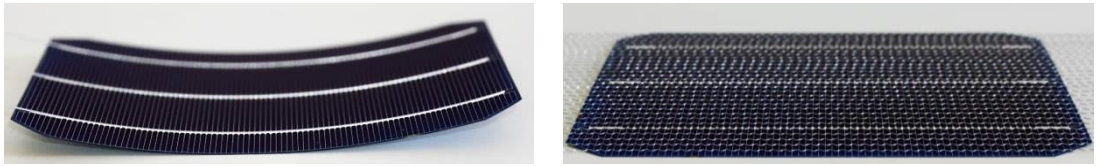

(a) (b)

Figure 6.5: Deformation of a solar cell (size: 156 mm × 156 mm) connected on one side: (a) solar cell connected by three ribbon interconnectors on its busbars and (b) solar cell connected by 30 wave-shaped wires on its finger grid.

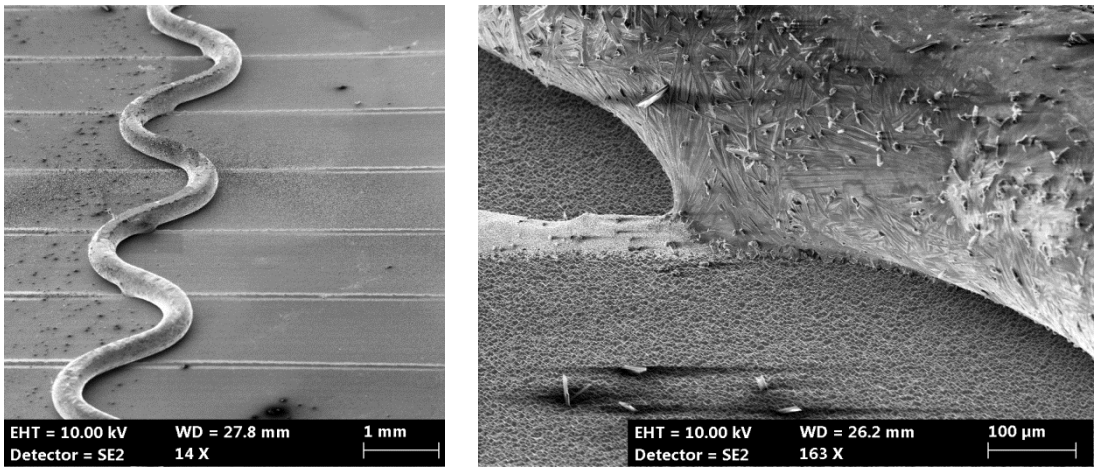

(a) (b)

Figure 6.6: SEM images of a solar cell connected by wave-shaped wires soldered on the finger grid: (a) part of one wire (14x magnification) and (b) wetting of one contact finger by the solder alloy coating of the wave-shaped wire (163x magnification).

30 wave-shaped wires were soldered on the front finger grid of eight solar cells; four full cells and four laser-cut half cells. In addition, three half solar cells were interconnected to a solar cell string to determine whether the interconnection of multiple solar cells is more challenging compared to single cell soldering. Wave-shaped

wires with a copper core diameter of 300 µm, a period of 3.0 mm, an amplitude of 1.5 mm (peak-to-peak), and a solder coating consisting of Sn62Pb36Ag2 with a thickness of 5 to 20 µm were used. The distance between the wires was 5.1 mm. The solar cells and the wave-shaped wires were positioned on a glass-fiber support plate with a surface temperature of 110 °C and the interconnection was done by semi-automatic IR soldering. To enable electrical characterization measurements with minimized mechanical stress by rear interconnectors each solar cell is connected by solely one ribbon interconnector (1.5 mm × 0.2 mm, Sn62Pb36Ag2 coating) manually soldered on the middle pad row on the rear side. The soldered string consisting of three half solar cells was connected by three ribbon interconnectors on the rear side. Figure 6.7 shows both sides of a solar cell sample connected by wave-shaped wires, and Figure 6.8 shows a string of three interconnected half solar cells.

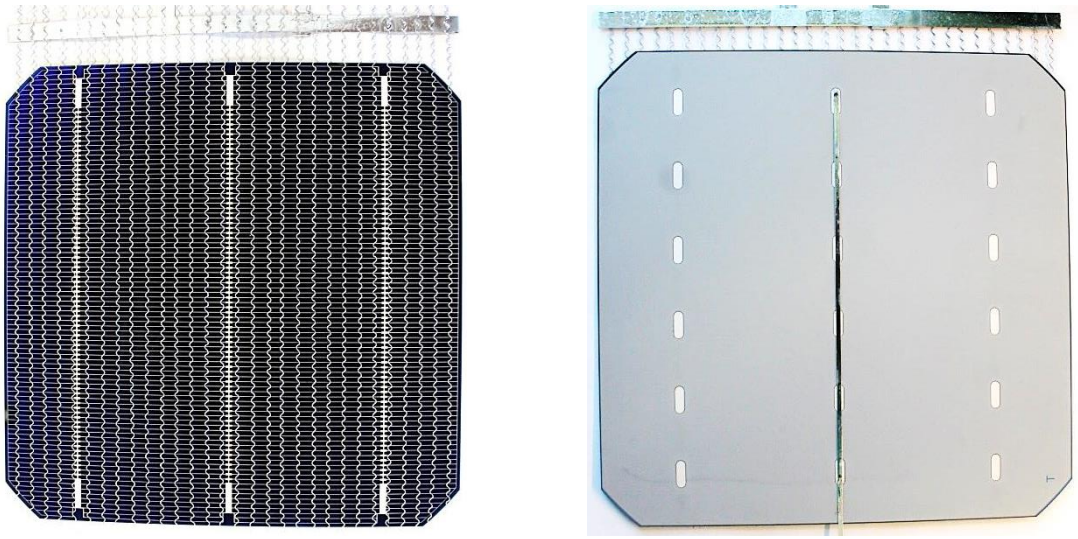

(a) (b)

Figure 6.7: 3BB solar cell (size: 156 mm × 156 mm) connected by (a) 30 wave-shaped wires on the front side and (b) one ribbon interconnector on the rear side. On the front side the wires were soldered on the finger grid, whereas on the rear side the contact pads of the middle pad row are connected by one ribbon interconnector [135].

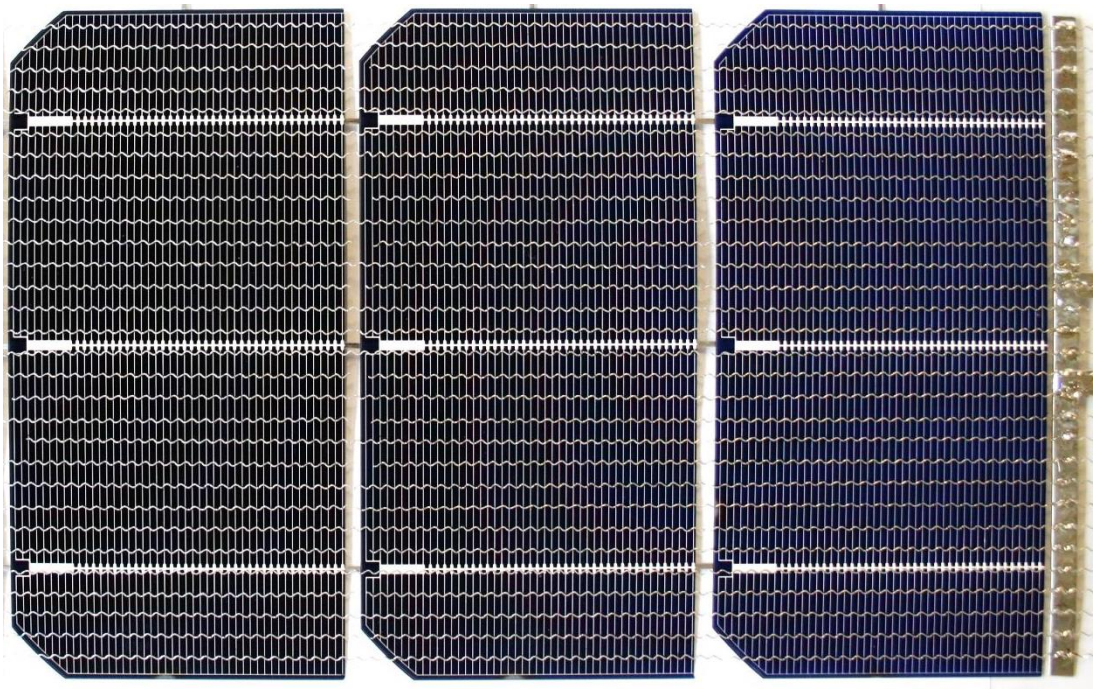

Figure 6.8: Solar cell string including three half solar cells (size: 156 mm × 78 mm), each connected by 30 wave-shaped wires on the front side and three ribbon interconnectors on the rear side. On the front side the wires were soldered on the finger grid, whereas on the rear side the contact pads are connected by ribbon interconnectors [135].

6.2.2 EL imaging and mini-module manufacturing

After soldering interconnectors on both sides EL imaging was performed to detect defects due to the interconnection process. Subsequently, mini-modules were manufactured with each connected solar cell, as well as with the string of three half solar cells. For these mini-modules a conventional module setup was used (see Figure 2.5). The module setup consists of a front glass (thickness: 3 mm), an encapsulation polymer (EVA, initial thickness: 460 µm), the connected solar cell (or string), another EVA layer, and a commercially available white backsheet. The encapsulation was performed with a conventional lamination process for PV modules. After the encapsulation EL imaging indicates potential defects due to the lamination process. Furthermore, electrical characteristics of the one-cell modules were measured with a

PV module flasher. Figure 6.9 shows EL images of the four full cells (M1-M4) and the four half cells (M5-M8) after soldering, as well as after encapsulation. Figure 6.10 indicates the string of three half solar cells after soldering and lamination process.

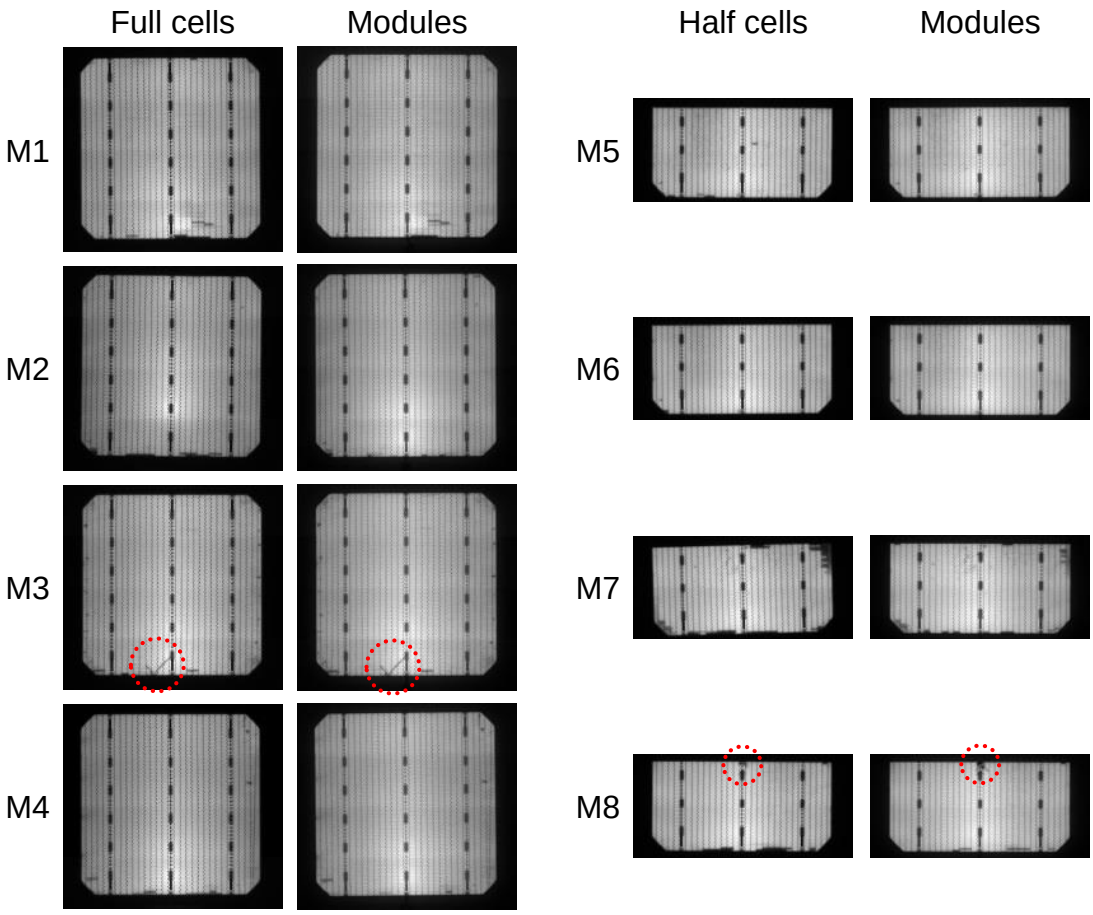

Figure 6.9: EL images of 8 solar cells after soldering of wave-shaped wires on the finger grid (Full cells and Half cells) and after the lamination process (Modules) [135]. Solar cell cracks are are marked with red dotted circles.

The EL images show homogeneous connection of the solar cells by soldering on the finger grid. However, one full-cell (M3) and one half-cell (M8) module show cracks, propagating from a crack origin located at the solar cells edge. Consequently, it can be assumed that the cracks occurred not in the soldering process, but due to manual solar cell handling. In addition, all eight solar cell samples show minor darker areas located at the sample edges, which result from finger defects, presumably caused by

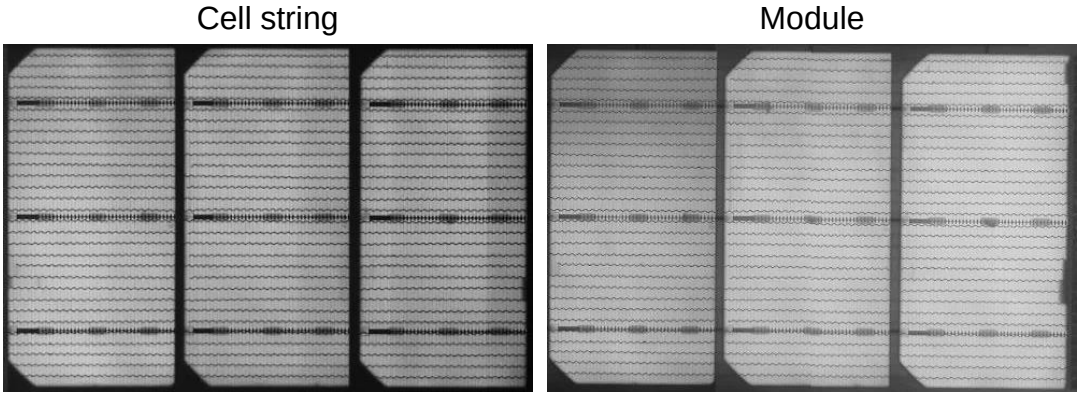

Figure 6.10: EL images of a solar cell string including three solar cells, each connected by wave-shaped wires on the front side and ribbon interconnectors on the rear side: (a) after soldering and (b) after the lamination process [135].

thermomechanical stress. The EL images of full cell sample M4 and half cell sample M6 show fewest defects. Full cell sample M3 with the cracks and half cell sample M7 show the most significant defects after soldering. The EL images of one-cell PV modules after the lamination process show less defects compared to solar cell samples after soldering, which is caused by an improved contact due to mechanical pressure. Finger disruptions due to thermomechanical stress after soldering were recovered by a pressing force between the wave-shaped wires and the solar cell surface caused by the encapsulation. In some areas, this reestablished the electrical current flow in the contact fingers. Near the solar cell edges of the string of three half solar cells only minor damages are visible (as for the one-cell samples), which demonstrates that it is possible to interconnect multiple solar cells to strings and to embed them to manufacture a PV module.

6.2.3 Temperature cycling

Temperature cycling according to the test standard for PV modules was performed to examine whether the module samples meet the requirement of less than -5% relative power loss after 200 thermal cycles [19]. Differing from the test standard, no electrical current was applied and the temperature gradient in the heating and cooling period

was increased from the standard value of 1.6 K/min to 8.0 K/min. This method was published in 2019 by Schiller *et al.* and is called aTC [137]. Preliminary tests were performed to determine appropriate aTC test parameters that result in sample temperatures in accordance with the test standard requirements. A test module with two temperature sensors inside (thermocouples) shows temperatures between 86.9 °C and 87.7 °C during the upper temperature holding period (nominal temperature: 85 °C) and between −41.4 °C and −44.0 °C during the lower temperature holding period (nominal temperature: −40 °C). EL imaging was performed and the IV-characteristics were measured initially, after 200, and 400 accelerated temperature cycles. Figure 6.11 and Figure 6.12 show the EL images of the four full-cell and the four half-cell modules.

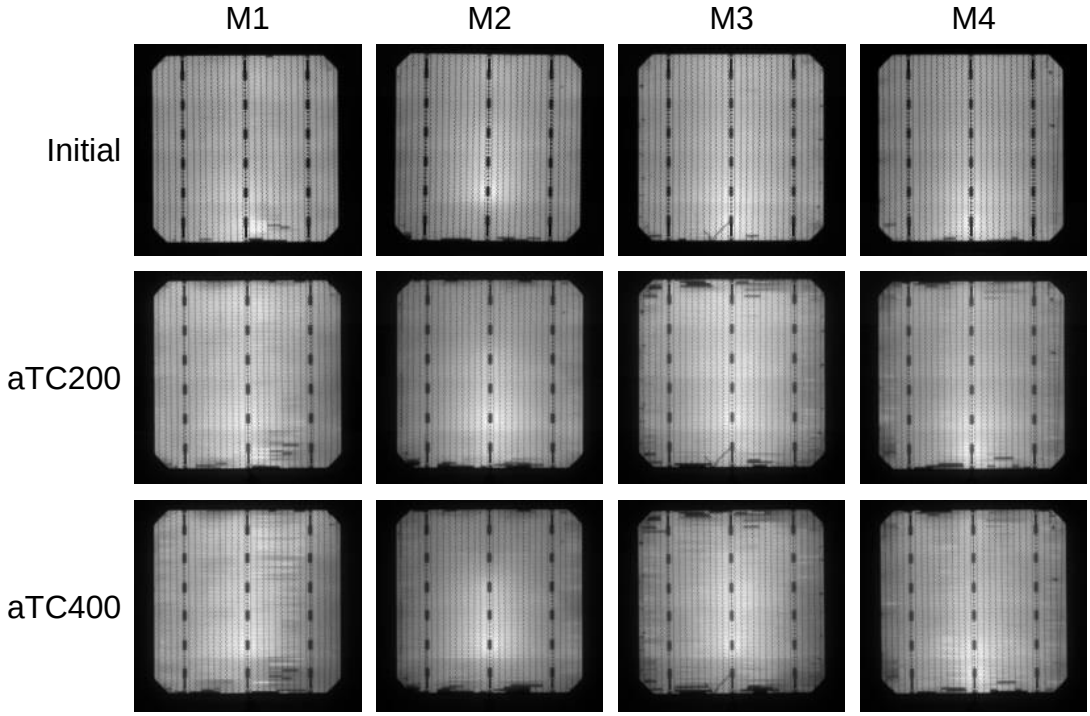

Figure 6.11: EL images of four PV modules each including one full solar cell (size: 156 mm × 156 mm) connected by wave-shaped wires on the finger grid (M1-M4). Measurements after the lamination process (Initial), after 200 (aTC200) and after 400 accelerated thermal cycles (aTC400) are shown. The EL images show initial finger defects (darker areas), and additional defects that were caused by thermomechanical stress due to temperature cycling [135].

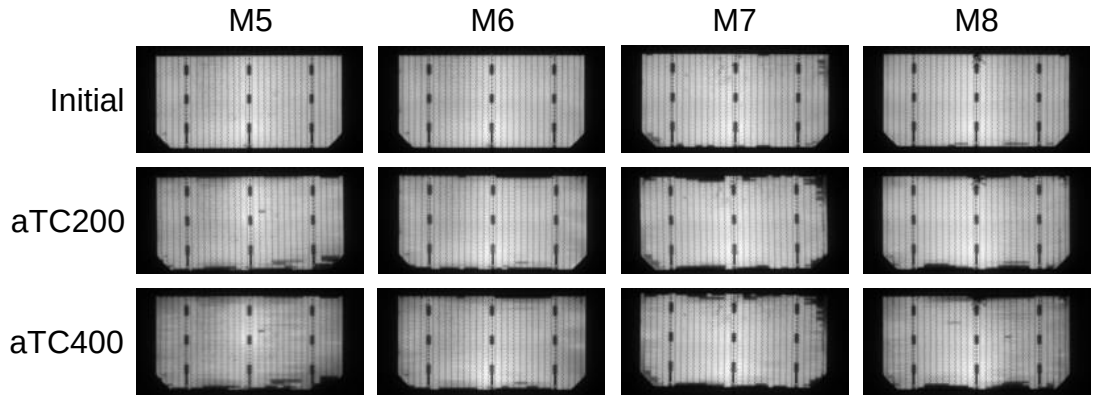

Figure 6.12: EL images of four PV modules each including one half solar cell (size: 156 mm × 78 mm) connected by wave-shaped wires on the finger grid (M5-M8). EL images after the lamination process (Initial), after 200 (aTC200), and after 400 accelerated thermal cycles (aTC400) are shown. Initial finger defects and additional defects caused by thermomechanical stress (darker areas) are shown [135].

The relative changes of the short-circuit current I_{SC}, the open-circuit voltage V_{OC}, the fill factor *FF*, and the power at the maximum power point P_{MPP} of the eight one-cell modules are shown by Figure 6.13. For all module samples, the I_{SC} and the V_{OC} remained constant (maximum deviation smaller than ±2%), which demonstrates that the solar cell themselves are not affected significantly by temperature cycling. In the group of the full-cell modules sample M4 shows the lowest relative degradation after 400 accelerated thermal cycles; the *FF* decreased by −1.3% and the P_{MPP} loss was −2.5%. Module sample M3 shows the strongest relative degradation of the full-cell modules with a *FF* decrease of −4.3% and a P_{MPP} loss of −4.8%. With a *FF* decrease of −2.2% and a P_{MPP} loss of −3.3% sample M6 shows the lowest relative degradation for the one-cell modules containing half cells. In this sample group M7 shows the strongest relative degradation with a *FF* decrease of −5.7% and a P_{MPP} loss of −5.7%. This confirms the optical impression determined by EL imaging of the connected solar cells after the soldering process.

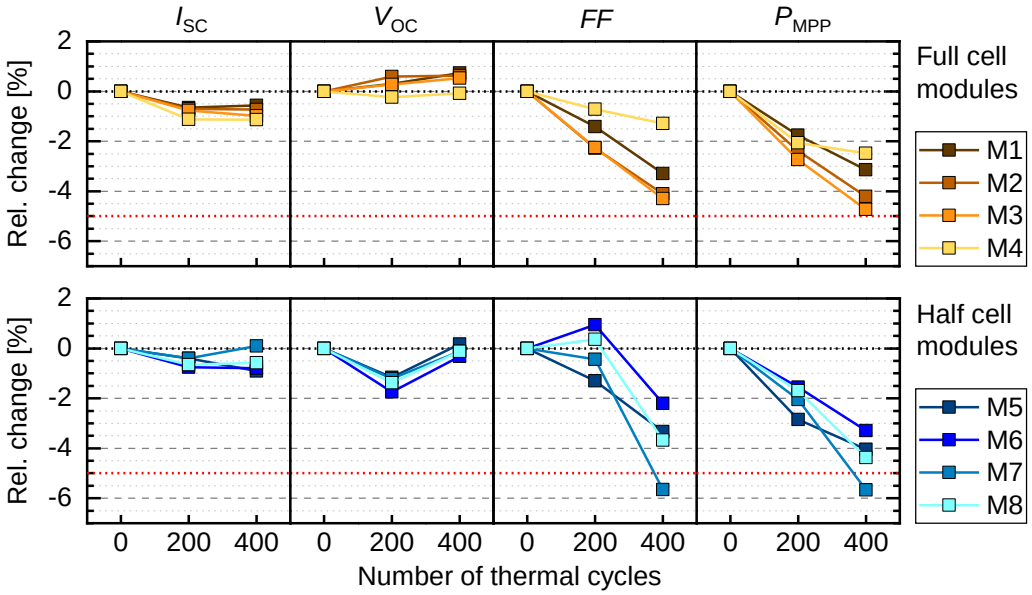

Figure 6.13: Development of the measured electrical parameters of eight PV modules, each including one solar cell (four full and four half solar cells) connected by wave-shaped wires. Shown is the relative change of the electrical parameters after the lamination process, and after 200 and 400 accelerated thermal cycles respectively [135].

6.3 Interconnection of back-contact solar cells

The interconnection of BC solar cells was tested by soldering 24 wave-shaped wires on the contact metallization of 12 half solar cells (first sample group) developed at Fraunhofer ISE [83]. Wave-shaped wires with a copper core diameter of 350 µm, a period of 3.0 mm, an amplitude of 1.1 mm (peak-to-peak), and a solder coating (5 to 20 µm Sn62Pb36Ag2) were used. Subsequently, the connected solar cells were encapsulated with a standard module setup (see Figure 2.5). Figure 6.14 shows the rear side of one BC solar cell (half solar cell) with the contact finger grid and the contact pads (a), as well as a BC solar cell connected by 24 wave-shaped wires soldered on the contact pads (b). Figure 6.15 shows the EL image of the solar cell with most (a) and the fewest interconnection failures (b) of the first soldering experiments with BC solar cells.

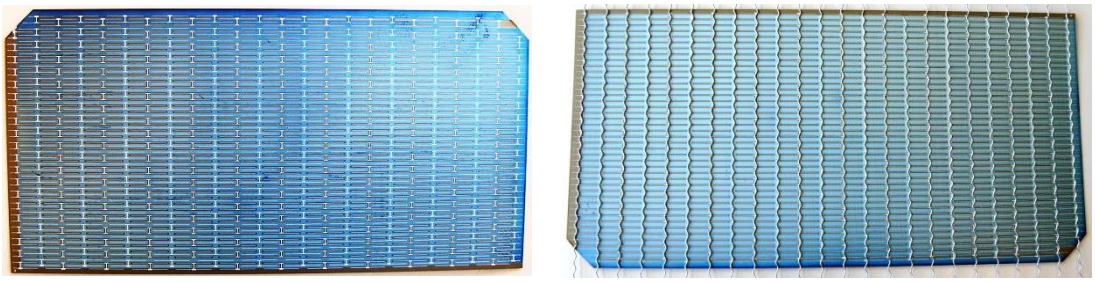

(a) (b)

Figure 6.14: (a) Rear side of a BC solar cell (size: 156 mm × 78 mm) that shows the contact finger grid and the contact pads, as well as (b) another BC solar cell (other half of a full solar cell) connected by 24 wave-shaped wires soldered on the contact pads.

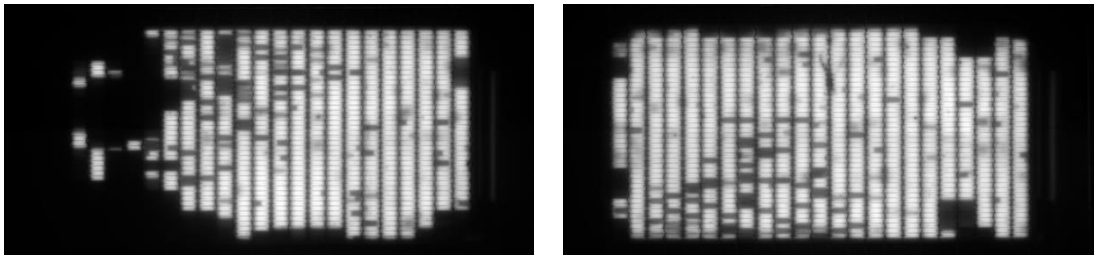

(a) (b)

Figure 6.15: EL images of BC solar cells connected by IR soldering of wave-shaped wires: solar cell showing (a) the most and (b) the fewest interconnection failures of the sample group.

Accelerated temperature cycling tests according to the IEC test standard for PV modules were performed on 5 one-cell module samples to test the long-term stability of the interconnections. Figure 6.16 shows EL images of one exemplary PV module including a BC solar cell connected by wave-shaped wires with initial defects. In addition, the development of the defects after 200 and 400 thermal cycles is shown.

The relative changes of the short-circuit current I_{SC}, the open-circuit voltage V_{OC}, the fill factor *FF* and the power at the maximum power point P_{MPP} of the one-cell modules after 50 and 400 accelerated thermal cycles are shown by Figure 6.17. IV measurements were performed after 200 accelerated thermal cycles, but unfortunately, wrong settings distorted the results, and it is not possible to compare the

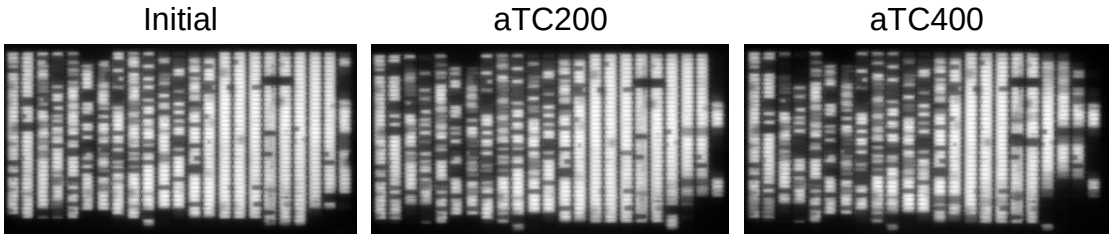

Figure 6.16: EL images of one exemplary PV module including a BC solar cell connected by IR soldering of wave-shaped wires. Initial defects, as well as defects after 200 and 400 accelerated thermal cycles (aTC200 and aTC400) are shown.

data with the results of the other measurements (initial, aTC50, and aTC400). After 50 accelerated thermal cycles the maximum decrease determined is −1.3% for the I_{SC}, −0.3% for the V_{OC}, −1.3% for the *FF*, and −2.8% for the P_{MPP}. After 400 accelerated thermal cycles the maximum relative I_{SC} decrease is −2.2% and the V_{OC} shows no significant degradation. However, a *FF* loss of between −2.4% and −4.3%, and a relative power degradation of between −4.1% and −6.2% was determined for the samples.

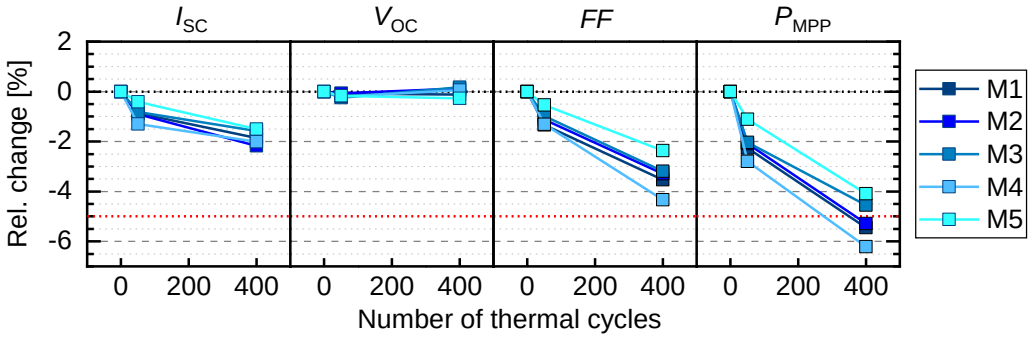

Figure 6.17: Development of the measured electrical parameters of five PV modules, each including one BC solar cell connected by 24 wave-shaped wires. The relative change of the electrical parameters after 50 and 400 accelerated thermal cycles is shown.

7 PV module power calculation

7.1 Description of the CTM analysis

The base value for the P_{MPP} of a PV module is the power of the solar cell matrix. However, the P_{MPP} is also significantly influenced by the module setup and the materials. In addition to optical gains and losses, the electrical interconnection determines the output power of a PV module. For a PV module including BC solar cells optical properties of the interconnectors can approximately be neglected and only the electrical properties influence the P_{MPP}. In Chapter 6, the potential for soldering on the front finger grid of standard solar cells is shown, which makes busbars dispensable. Omitting the busbars increases the solar cell power due to less shading, less recombination losses, et cetera. In addition, round wire interconnectors can reflect light to the solar cell surface, which decrease shading losses even further. This effect is described by the effective width (EW) [68, 69]. Nevertheless, when interconnecting standard solar cells with wave-shaped wires the additional shading due to the wavy wire shape causes increased optical losses. Furthermore, the electrical resistance is increased by the adapted shape (see Section 5.2.3), also resulting in an increase of the electrical losses. Simulations were performed to determine the influence of additional shading due to the wavy shape of the wire interconnector on the front side of a silicon solar cell and to calculate the potential power of a PV module including busbarless solar cells interconnected by wave-shaped wires.

The output power of a PV module with common solar cells without busbars and a front-to-back interconnection by wave-shaped wires is calculated by SmartCalc.CTM, which is a simulation tool developed at Fraunhofer ISE by Hädrich *et al.* [138, 139]. Starting with the nominal power (or efficiency) of the solar cells at standard test conditions (STC), the k-factors describe the geometrical, optical, and electrical gains and losses that determine the output power (or efficiency) of a PV module. The overall change of power (or efficiency) as a percentage value is called cell-to-module (CTM). Table 7.1 shows the k-factors that describe the gains and losses of a PV module.

Table 7.1: k-factors describing the losses and gains due to the PV module setup and the material composition starting from solar cell matrix power resulting in PV module power at standard test conditions (STC).

k-factor	Name	Explanation
k1	Module margin[1]	**Geometrical factors**: module margins and cell spacings influence the active area and efficiency of a PV module
k2	Cell spacing[1]	
k3	Cover reflection	**Optical factors**: gains and losses due to transmittance or absorption in materials, and reflection on surfaces
k4	Cover absorption	
k5	Cover/encaps. reflection	
k6	Encaps. absorption	
k7	Interconnection shading	
k8	Cell/encaps. coupling	
k9	Finger coupling	
k10	Interconnector couping	
k11	Cover coupling	
k12	Cell interconnection	**Electrical factors**: losses due to the electrical resistance of materials and the mismatch of the solar cells
k13	String interconnection	
k14	Electrical mismatch	
k15	Junction box and cabling	

[1]Only relevant for efficiency, not for power analysis

7.2 Full and half solar cells

Figure 7.1 shows the results of an exemplary calculation of the CTM of two PV modules; the first one containing 60 commercially available silicon solar cells, the other one with a matrix of 120 identical solar cells cut into half cells. For the simulation a common PV module setup, as shown by Figure 2.5, is used. The results reveal a lower total cell power of the half cells, which is caused by recombination losses at the laser-cut edge.

Since the module power is analyzed, the geometrical factors k1 and k2 are not taken into account. k3 to k10 simply scale with the total cell power, and k14 and k15

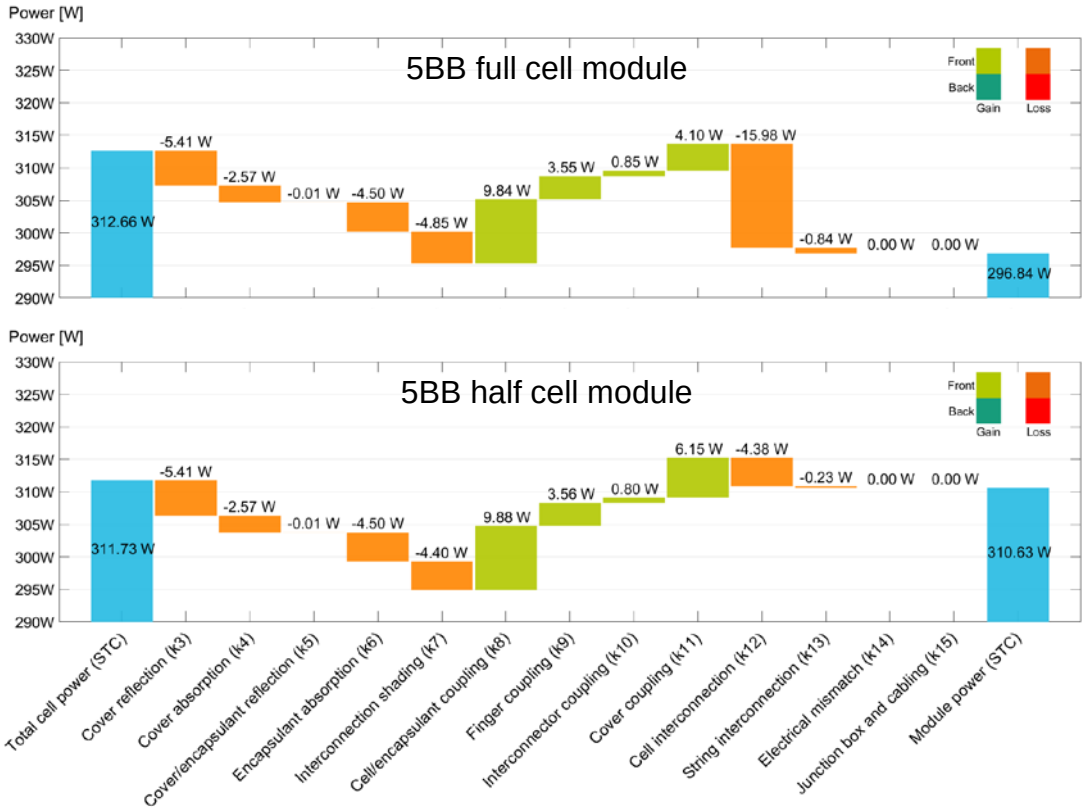

Figure 7.1: CTM gains and losses (k-factors) of a standard PV module including 60 full, or respectively 120 half solar cells with a 5BB contact layout and ribbon interconnection.

are zero, because an ideal cell matching and a perfect junction box was assumed. The largest difference shows the k12, with a nearly four times higher loss in the interconnectors for a PV module containing full solar cells (−15.98 W) compared to half solar cells (−4.38 W). This can be explained by an approximately halved elecrical current of the half solar cells. The k13, which describes the losses in the cross connectors between the strings of a PV module, also correlates with the current, and is higher for full solar cells. The larger cover coupling gain (k11) for the half solar cells (+6.15 W vs. +4.10 W) can be explained by the increased cell spacing area, which to some extent reflects light that can be re-reflected to a solar cells front surface.

7.3 Wave-shaped wires

Table 7.2 shows the electrical properties for different solar cell types that were used for the comparison of the estimated power of PV modules including solar cells with 5BB (ribbon cross section: 0.9 mm × 0.22 mm, EW: 0.9) and MBB layout (12 wires per side, copper core diameter: 350 µm, EW: 0.6), as well as solar cells without busbars interconnected by wave-shaped wires (EW: 0.6) soldered on the contact finger grid. The solar cell data of the MBB solar cells and the solar cells without pads or busbars are calculated based on the data of the 5BB solar cells but with adjusted electrical currents (I_{SC} and current at maximum power point (I_{MPP})) because of less shading by the contact metallization. In the CTM calculation the solder coating is not taken into account. The busbarless solar cells were assumed to be bifacial with a contactable finger grid on both sides, but no illumination on the rear side. The PV module power was simulated for full and half solar cells. An identical common PV module setup was assumed for all solar cell types.

Table 7.2: Solar cell characteristics to compare the module power for different metallization layouts.

Layout	**Solar cell properties**					
	I_{SC} [A]	I_{MPP} [A]	V_{OC} [V]	V_{MPP} [V]	P_{MPP} [W]	η [%]
5BB full cell[1]	9.707	9.158	0.670	0.569	5.211	21.333
5BB half cell[2]	4.857	4.577	0.669	0.568	2.598	21.273
MBB full cell[3]	9.706	9.157	0.670	0.569	5.211	21.331
MBB half cell[3]	4.852	4.572	0.669	0.568	2.595	21.250
0BB full cell[4]	9.826	9.270	0.670	0.569	5.275	21.594
0BB half cell[4]	4.916	4.633	0.669	0.568	2.630	21.533

[1]Commercially available silicon solar cell (mean values of IV measurements on three solar cells)

[2]Commercially available laser-cut half silicon solar cell (mean values of IV measurements on two half solar cells)

[3]Calculated cell data assuming same wafer material as 5BB solar cell but adapted MBB layout

[4]Calculated cell data assuming same wafer material as 5BB solar cell but adapted layout without pads or busbars

The potential output power of a PV module including solar cells (full and half solar cells) with a 5BB interconnection layout and ribbon interconnectors, as well as with a MBB interconnection layout and round wires, is shown by Figure 7.2. In addition, the power for busbarless interconnection by wave-shaped wires soldered on the contact fingers is shown for different wire types and numbers. The module power was simulated for wire interconnectors with a diameter of 300 and 350 µm, a period of 3.0 mm, and amplitudes of 1.0, 1.2, and 1.5 mm.

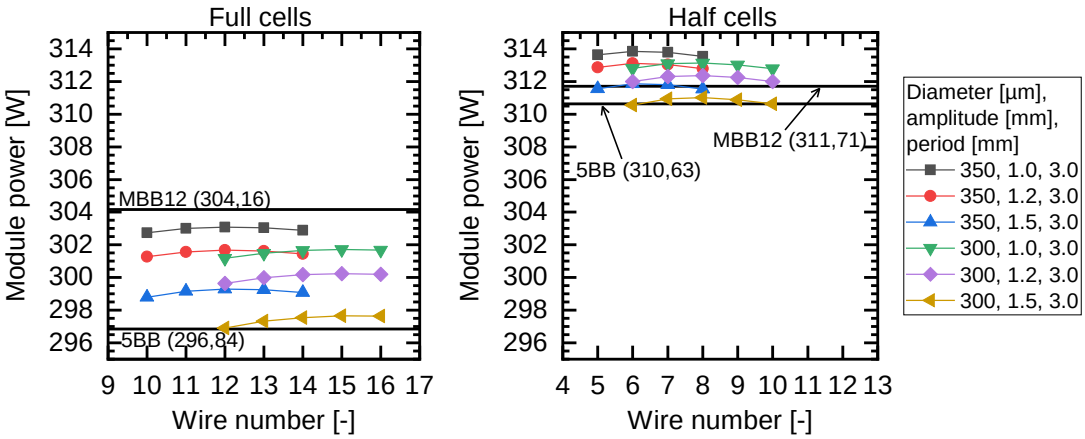

Figure 7.2: Calculated output power at the maximum power point for PV modules with a standard module setup including (a) full and (b) half solar cells with different interconnection concepts. Included are 5BB, MBB, and solar cells without busbars connected by various numbers of wave-shaped wires with different diameters and amplitudes soldered on the finger grid.

For the PV modules with 60 full solar cells the results reveal that the maximum power of 304.16 W can be reached with MBB interconnection, whereas the 5BB interconnection shows the lowest power of 296.84 W. This can be explained by comparable cell efficiencies of 21.331% for the MBB and 21.333% for the 5BB solar cells and, for the 5BB interconnection, a significantly larger power loss in the ribbon interconnectors of −15.98 W which is indicated by k12 in Figure 7.1. With an increased solar cell efficiency of 21.594% a module with solar cells without busbars interconnected by wave-shaped wires shows a power of between 296.90 W (12 wave-shaped wires, diameter: 300 µm, amplitude: 1.5 mm) and 303.09 W (12 wave-shaped wires, diameter: 350 µm, amplitude: 1.0 mm). A PV module with 120 half solar

cells shows a power of 311.71 W with MBB and 310.63 W for 5BB interconnection. The smaller difference can be explained by a significantly lower interconnector loss (k12) of −4.38 W caused by the lower I_{MPP} for a PV module with half solar cells. PV modules including half solar cells without busbars interconnected by wave-shaped wires have the potential for highest output power, reaching power values between 310.56 W (6 wave-shaped wires, diameter: 300 µm, amplitude: 1.5 mm) and 313.85 W (6 wave-shaped wires, diameter: 350 µm, amplitude: 1.0 mm).

8 Discussion

8.1 Brief summary of the key findings

In the past years, progress has been made in the development of solar cells enabling significant efficiency increases by using thinner wafers, layouts with smaller contacts, alternative solar cell architectures like back-contact back-junction solar cells, etc. Consequently, PV module manufacturers are confronted with new challenges when interconnecting solar cells for the production of efficient and reliable PV modules. After interconnecting solar cells by soldering thermomechanical stress caused by the CTE mismatch of copper and silicon is one major problem that is significantly influenced by

- the contact design of a solar cell and
- the mechanical properties of the interconnectors.

The main influence factors were identified by simulations of the distribution of thermomechanical stress after the interconnection process. The results indicate lower maximum stress levels for interconnectors with reduced yield limit. Furthermore, for single side interconnection of back-contact solar cells, a reduction of the bending deformation was simulated and experimentally confirmed by measurements (see Section 3.3).

This work focuses on changing the geometry of an interconnector, instead of its microstructure, to affect its mechanical properties substantially. Two methods for the deformation of copper interconnectors were identified and tools were implemented: one method puts a focus on easy, precise, and reproducible laboratory use, while the other method potentially enables an integration in automated solar cell interconnection machines. In longitudinal direction a reduction of the pseudo yield limit (introduced in Section 5.2.2) up to -88.5% was determined for wave-shaped interconnectors [133], whereas for enhanced annealing of the copper material a maximum yield limit reduction of -45% was published [38]. In addition, soldering experiments indicated a lower degradation rate of interconnections when using wave-shaped wires.

As a result, experiments demonstrated that wave-shaped wires enable to omit large contacts by soldering on contact fingers of commercially available solar cells and on small contact pads of BC solar cells, achieving a long-term stability in thermal cycling that is comparable to common busbar- and ribbon based approaches, and that agree with the requirements of the test standard for PV modules [19].

8.2 Assets and drawbacks of common interconnection technologies for solar cells

8.2.1 How current interconnection technologies influence important properties of PV modules

The contact layout and the interconnection of silicon solar cells significantly influence crucial properties of a PV module. Costs, efficiency, as well as the long-term stability of a PV module is affected by the interconnection technology. In the following, influence factors are explained and current technologies, as well as developing approaches for the interconnection of common front-to-back and BC solar cells are briefly reviewed.

The contact metallization and the interconnectors on the front side shade the solar cells and therefore reduce the electrical module efficiency. For this reason, in order to optimize the efficiency, the width of contact fingers, busbars, and of ribbon interconnectors has to be as small as possible. Furthermore, recombination losses can be reduced by a decrease of the metallization area on the silicon wafer. In contrast, a large cross section of contact fingers, busbars, and ribbons reduce ohmic losses. For these reasons, contact fingers and ribbon interconnectors with large aspect ratio are ideal for an optimized initial PV module efficiency. However, process limitations sometimes impede to further increase the aspect ratio of the commonly screen-printed metallization. In addition, narrower contact fingers and busbars with decreased contact area on the silicon wafer surface presumably result in a reduced mechanical stability. Additionally, ribbon interconnectors for high efficiencies with a smaller width and a larger height cause large mechanical stress maxima due to the CTE mismatch of copper and silicon (see Section 2.3). Mechanical stress maxima may

cause defects that result in lower efficiency of a PV module, either initially after module manufacturing or after a certain operating time period in the field, which both reduces the energy yield of a power plant. In summary, there is a large number of factors in solar cell and PV module production that influence the efficiency, as well as the long-term stability. For these reasons, an optimum is challenging to identify and has to be determined for a certain set of materials and processes, as well as for the planned use case.

In the last years, driven by rising solar cell efficiencies and the trend to larger wafer sizes, solar cell and PV module manufacturers increased the number of busbars of common solar cells from two busbars up to five, six or even seven busbars. To transport higher electrical currents without increasing shading losses, the aspect ratio of interconnectors was continuously increased. Furthermore, busbar shapes were adapted (e.g. tapered or segmented busbars) to reduce costs by lowering the amount of silver paste per solar cell. This also influences mechanical stress levels in the silicon wafer and in the interconnections.

8.2.2 Interconnection with round wires instead of ribbons

Alternative interconnection approaches based on a large number of round wire interconnectors have different advantages. For example, the effective optical width of a round wire is in the range of 0.6, whereas a rectangular ribbon with round edges has an EW of approximately 0.9. This shows that wire interconnectors can decrease shading significantly, depending on wire number and diameter. Furthermore, the current collection is more homogeneous and the current paths are shorter, which potentially reduces the series resistance. This enables a reduction of the contact fingers cross-section without increased ohmic losses compared to common ribbon-based interconnection, which reduces shading even further. In addition, using a high number of wire interconnectors improves the contact redundancy, which results in less power degradation in case of defect interconnections or solar cell breakage. According to several publications, the reliability of PV modules with wire-based interconnection approaches are at least comparable with common busbar- and ribbon-based interconnection [54, 70]. To change a production line from a busbar- and ribbon-based to a pad- and wire-based MBB interconnection technology (introduced

in 2012 by Schmid [53, 54]), the solar cell contact design has to be adapted because small contact pads instead of busbars are required. Additionally, a stringing machine that is able to handle thin sensitive round wires has to be used. In contrast, the SWCT by Meyer Burger (introduced in 2002 by Day4 Energy [55, 67]) is based on the idea of embedding an even larger number of thinner wire interconnectors in a polymer foil in the first step. In the second step, the polymer foil is laminated to the solar cells and the wires, which are coated with a special low-melting solder alloy, interconnect the solar cells electrically. This approach enables the interconnection of solar cells without pads or busbars. Furthermore, the maximum temperature the solar cells are exposed to is lower compared to typical solder processes, which is beneficial for solar cells that are prone to defects caused by high temperatures as highly efficient SHJ solar cells. However, special low-melting solder, for example In- or Bi-based solder alloys, which are more expensive and tend to be more brittle, have to be used instead of standard Sn60Pb40 or Sn62Pb36Ag2. Other experimental approaches use wire interconnectors that are woven into glass- or polymer-fabrics, but presumably such fabrics are more expensive compared to bare wires or SmartWire foil.

8.2.3 Interconnection of back contact solar cells

BC solar cells reach highest efficiencies of silicon wafer-based mono-junction devices [13]. However, the interconnection is asymmetric and therefore challenging, because the contacts of both polarities are located on the rear side. Using copper-based interconnectors leads to higher thermomechanical stress levels compared to common front-to-back interconnection technologies and significant deformation of the solar cells after the interconnection process due to the CTE mismatch. Sunpowers edge interconnection technology reduces stress and solar cell deformation by using smaller solar cells with an edge length of 125 mm, a thick metallization layer on the rear side, and edge-to-edge interconnectors [79]. Disadvantages are the higher solar cells costs due to the time- and material-consuming metallization process, and the limitation to small wafer sizes, which also increases the price of their solar cells and PV modules. Another approach uses conductive backsheets with a structured copper layer connected by an ECA [80]. This reduces thermomechanical stress, but

both, structured backsheets and ECAs, tend to be very expensive. Interconnecting BC solar cells with structured copper foil interconnectors has the potential to reduce thermomechanical stress significantly, but is also very expensive due to high manufacturing costs for the interconnectors. Approaches using ribbons and busbars for the interconnection are less costly, but the used solar cells (see Figure 2.12) are assumed to be expensive. Additional process steps and materials are mandatory to isolate each second contact with an isolating coating and to apply a low-temperature metallization paste that is required for the additional busbar print, which tends to be mechanically less stable. Furthermore, thermomechanical stress and solar cell bending is a problem. Using wire interconnectors, pad contacts, and finger interruptions instead of busbars and ribbon interconnectors reduces the solar cell costs significantly, but thermomechanical stress and solar cell bending remains an issue. The interconnection of BC solar cells with SmartWire foil should be possible, but requires adapted foils that are very long and include precisely positioned, interrupted wire interconnectors. This approach may reduce thermomechanical stress, due to the polymer foil that mechanically hold the wires, and possibly preventing large wire deformation when the temperature changes. However, low-temperature solder is more expensive than standard Pb-based solder alloys and further tests are needed to show whether the SWCT is applicable for BC solar cells.

8.3 Analysis of thermomechanical stress after the soldering process

8.3.1 Distribution of thermomechanical stress

Simulations were performed to gain a deeper understanding of thermomechanical stress in silicon solar cells due to the soldering process. For solar cells with busbars and with pad contacts the most critical areas with maximum stress levels are located at the outermost contacts. This is in accordance with findings published by Meier *et al.*, Kraemer *et al.*, and Beinert *et al.*, who also determined stress peaks located at the outermost contacts [31, 34, 38]. Figure 8.1 shows two characteristic distributions of the first principal stress (σ_{I}) after the soldering process on the front side, one for a

solar cell with three continuous busbars (a) and one with contacts pads (b) (both with symmetrical contact layout on both sides). Furthermore, simulation results published by Meier *et al.* and Beinert *et al.* indicating the stress distribution in a PV module are shown [34, 38]. The simulated stress distribution on the surface of a solar cell of the three simulations is comparable. However, Beinert *et al.* used a linear elastic material model for copper, included the lamination process, and plotted the mean value of σ_{XX} and σ_{YY} instead of σ_I, which explains the deviation of the absolute stress values. A simulation of the stress distribution for wire- and pad-based interconnection using thin wire interconnectors shows comparable stress levels and reveals that using wire interconnectors and pads instead of busbars and ribbons does not necessarily reduce thermomechanical stress in solar cells.

8.3.2 Influence of the contact layout

It was analyzed how the different segments of a copper interconnector soldered on a contact pad row, on pads and in between pads, influence tensile and compressive stress levels (see Figure 3.5 (a)). In addition, thermomechanical stress was analyzed for different metallization layouts to identify geometrical influence factors leading to layout guidelines for reduced stress in silicon solar cells. The results indicate that the stress curve for the uninterrupted connection of a pad row with a continuous interconnector (continuous configuration) is an interaction of the on pads and the between pads configuration. However, for continuous interconnection the silicon wafer has to withstand the highest thermomechanical tensile stress levels located at the outermost contact edge. Figure 8.2 compares the simulated longitudinal stress along the contacts with simulations performed by Kraemer *et al.* and reveals similar curve characteristics. Both curves show a tensile stress peak located at the outermost contact (as also indicated by surface plots), compressive stress below inner contacts, and very low stress levels between pads in areas without interconnector contact to the solar cell. The differences of the longitudinal stress curve can be explained by two different contact geometries and wafer materials, since one simulation assumes a symmetrical contact layout on a monocrystalline silicon wafer [95], whereas the other simulates a busbar on the front side and contact pads on the rear side of a polycrystalline silicon wafer [31]. Furthermore, Kraemer *et al.* included creep of the

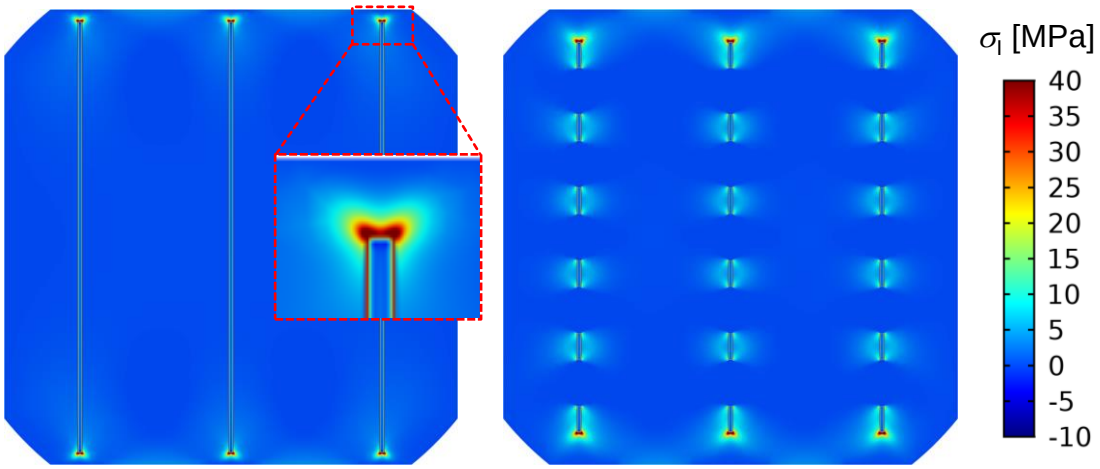

(a) Simulation Chapter 3 (b) Simulation Chapter 3

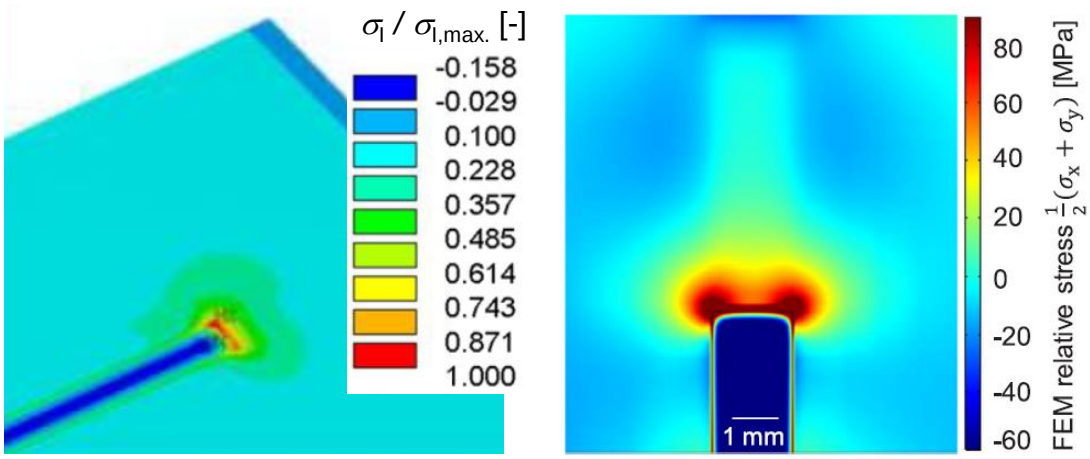

(c) Simulation by Meier *et al.* (d) Simulation by Beinert *et al.*

Figure 8.1: Stress distribution on the surface of solar cells after soldering (interconnectors hidden): simulation results (first principal stress (σ_I)) for (a) a busbar and (b) a pad contact layout (symmetrical contact layout on both sides). In addition, the stress distribution simulated by the FEM located at the end of a busbar is shown: (c) normalized stress by Meier *et al.* [38] and (d) mean value of σ_{XX} and σ_{YY} by Beinert *et al.* [34].

solder alloy material model and stated that after some time stress caused by soldering reduces substantially. However, both simulations deliver comparable initial results since characteristic stress values are determined to be in the same range. The total stress difference between maximum tensile and compressive stress at the outermost contacts is between 110 MPa and 130 MPa according to Kraemer *et al.*. The results of Simulation IV (see Section 3.3.4) revealed values between 125 MPa and 130 MPa. For the compressive stress below contact pads Kraemer *et al.* found stress levels between −120 MPa and −130 MPa, whereas Simulation IV showed values between −120 MPa and −125 MPa (exception: very small pads showed values between −105 MPa and −110 MPa).

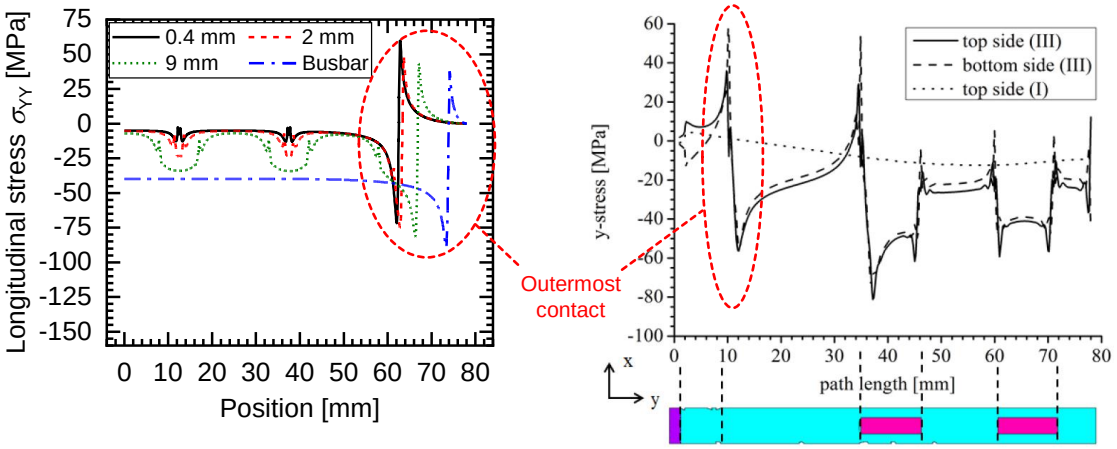

(a) Simulation Chapter 3 (b) Simulation by Kraemer *et al.*

Figure 8.2: Simulation results indicating longitudinal stress on the silicon surface along the contacts (pad rows or busbars) showing a tensile stress peak at the outermost contact and compressive stress located below inner contacts: (a) for different contact layouts (symmetrical layout on front and rear side) [95] and (b) for a busbar on the front side and contact pads on the rear side published by Kraemer *et al.* [31].

The results indicate that in order to reduce thermomechanical stress, most importantly tensile stress, it is beneficial to design a solar cell with a contact metallization consisting of large, protective pads at outermost positions and smaller inner pads. At present, many solar cell manufacturers take this into account. Furthermore, the results indicate that the distance between the outermost pads and the cell edges should be small. However, the simulation takes not into account that the

probability for cracks is substantially increased at solar cell surfaces and edges [94]. For this reason, depending on the material setup (silicon wafer, metallization paste, interconnectors, etc.) and the process flow (contact firing, soldering, half-cell cutting, etc.), which all affect the probability for cracks, an optimized layout has to be determined. On the one hand, if interconnection defects are the main problem after soldering or temperature cycling, the distance between outermost pad and solar cell edge should be reduced. On the other hand, this distance should be enlarged if the solar cells tend to crack near the outermost interconnection at the solar cell edges. Furthermore, a large number of inner pads with small distances in between results in reduced stress levels. Such a contact layout presumably leads to improved long-term stability of solar cells in PV modules [95]. An exemplary drawing of such a contact metallization for a solar cell with five pad rows on the front side is shown by Figure 8.3.

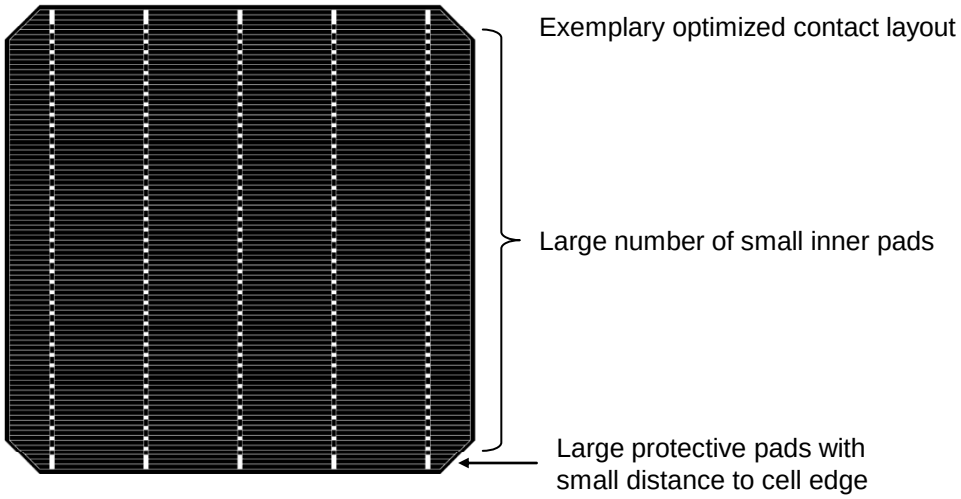

Figure 8.3: Exemplary drawing of a solar cell with a modified front contact metallization design (five pad rows) to minimize thermomechanical stress after the interconnection process.

In the last years, solar cell manufacturers changed the busbar geometry near the cell edges to shift the maximum stress away from the edges of a solar cell, which are more prone to cracks [94], and to locally increase the contact area of the outermost contact to improve the long-term stability. Examples are the busbars of a solar cell

manufactured by Hanwha Q Cells that narrow at the solar cell edge, as well as the special busbar design of Solarworld solar cells, both shown by Figure 8.4.

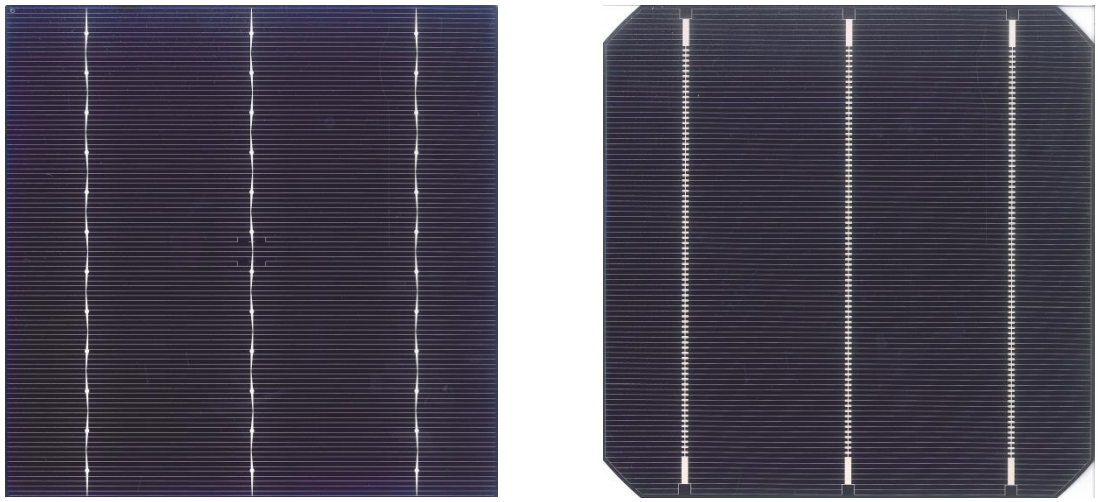

(a) (b)

Figure 8.4: Front side of two 3BB solar cells (size: 156 mm × 156 mm) with adapted contact layouts to prevent damaging at the solar cell and busbar edge: (a) Hanwha Q Cells solar cell with tapered busbars and (b) Solarworld solar cell with interrupted busbars, large, protective end pads, and increased distance to the solar cell edge.

8.3.3 Influence of the interconnector properties

The cross section, the Young's modulus, and the yield limit of an interconnector were determined as most important factors that influence thermomechanical stress after soldering significantly. This corresponds with Wiese *et al.*, who considers the mechanical properties and the geometry of interconnectors, as well as the creep properties of the used solder alloy as the most obvious influence factors that enable reduction of thermomechanical stress in solar cells [48].

Simulations of a solar cell section connected by a wire interconnector on one side indicate that a larger Young's modulus, yield limit, or diameter of a wire interconnector results in increased deformation (see Table 3.2), which is an indicator for the thermomechanical stress. Changing the diameter of a wire interconnector reference with

300 µm by 100 µm causes a relative displacement change of −72% (200 µm) or +42% (400 µm) respectively. Simulations performed by Wiese *et al.* also determined a large influence of the cross-section of an interconnector on thermomechanical stress in a solar cell. Additionally, a substantial influence of the aspect ratio of an interconnector (ratio of height and width) on thermomechanical stress was indicated. Furthermore, a reduction of the first principal stress of about 50% was found if the busbar width is larger than the width of the ribbon interconnectors [48]. An increase or decrease of a Young's modulus of 70 GPa by 30 GPa causes an relative displacement change of −37% (40 GPa) or +42% (100 GPa) respectively. This disagrees with simulation results published by Wiese *et al.* which indicate a minor influence of the Young's modulus of a ribbon interconnector on the thermomechanical stress in a solar cell after the soldering process [48]. Furthermore, a reduction of the wire interconnectors yield limit of 100 MPa by 50 MPa leads to a reduction of the deformation of a solar cell section of about −24%, whereas an increase by 50 MPa only causes a larger relative displacement of 1%.

The simulation of full solar cells connected on both sides show that ribbon and wire interconnectors undergo plastic deformation, which reduces thermomechanical stress in the interconnections and the silicon wafer after the soldering process. This is in accordance with findings by Zemen *et al.*, Wiese *et al.*, Meier *et al.*, and Kraemer *et al.*, who all determined plastic deformation of interconnectors and a resulting stress reduction for interconnectors with reduced yield limit [31, 38, 40, 48]. In addition, Zemen *et al.* measured less interconnection defects in full-size PV modules when using interconnectors with reduced yield limit [40].

8.4 Manufacturing processes and physical properties of wave-shaped wires

8.4.1 Motivation and approach

To change the mechanical properties of wire interconnectors a modification of their geometry was applied instead of modifying the microstructure by enhanced annealing. Two out of four tested methods for a deformation of straight into a wave-shaped

wire interconnectors delivered precise and reproducible shapes. One method is used for laboratory purposes, whereas the other potentially enables an integration into industrial stringing machines. Compared to straight wire interconnectors, the physical properties measured showed a substantial increase of the compliance in longitudinal direction and larger electrical resistance for wire interconnectors after the wave-shaping process.

8.4.2 Reshaping methods

For the most experiments a method based on two toothed wheels was used to manufacture wave-shaped wires with different wire shapes (see Section 5.1.3). This kind of method was also proposed by Storbeck and Hahn in a patent application [124]. An optimized reshaping method based on two synchronously self-rotating toothed wheels with an adapted shape was developed, which minimizes diameter change, grooves, pressure marks, non-symmetric wave-shapes, etc. as shown in Figure 5.11. Additionally, wave-shaped wires were manufactured by a second method using bending elements and feeding wheels (see Section 5.1.4). This method potentially reduces damaging even further, enables the reshaping of many wires in parallel, and can be integrated more easily into industrial stringing machines compared to approaches using toothed wheels (patent pending [136]). Krokoszinski and Amorim also proposed a method based on bending elements instead of toothed wheels, but in contrast they pre-position the wires on a solar cell surface and reshape the interconnector subsequently [125].

Wave-shaped wires with diameters of 300, 350, and 400 µm, periods of 1.5, 3.0, and 3.6 mm, and amplitudes between 0.603 and 2.125 mm were manufactured by Method 3 and 4 (described in Section 5.1.3 and 5.1.4) and characterized. A maximum amplitude deviation between −3% and +6.5% was determined. Figure 8.5 shows an exemplary wire interconnector in the wave-shaping process with two toothed wheels.

8.4.3 Physical properties of wave-shaped wires

Wave-shaping affects the mechanical properties of wire interconnectors significantly, resulting in more compliant wires with significantly reduced pseudo yield limits.

Figure 8.5: Wave-shaping of a wire interconnector by two toothed wheels (Method 3 by Machine 3 as described in Section 5.1.3).

Measurements of the force-rel. elongation curves by standard tensile tests revealed pseudo yield limits that are substantially reduced by up to −88.5%, depending on the wire diameter and shape. This is in accordance with Storbeck and Hahn who determined lower forces when elongating ribbon interconnectors with a wavy shape [124]. The measured data were analyzed by a new algorithm specifically developed to determine the gradient of the elastic part of the measured curve and the 0.2% (pseudo) yield force ($F_{\mathrm{p0.2}}$) automatically [133]. According to Kang *et al.* lubrication of rollers and copper material in the cold-rolling step during ribbon interconnector manufacturing results in up to −10% yield limit reduction [122]. The maximum relative yield limit reduction realized by enhanced thermal treatment of ribbon interconnectors published by Meier *et al.* is −45% [38]. Figure 8.6 shows the stress curve of a straight, an annealed straight, and a wave-shaped wire. The comparison of the three curves indicates the yield limit for all three methods and the potential of the pseudo yield limit of wave-shaped wires to significantly reduce thermomechanical stress in PV modules.

Changes of the electrical resistance caused by wire damaging and the change of the wire length were analyzed. The results reveal the quality of the process, as well as the unavoidable resistance change caused by the length change due to the adapted shape. Three influence factors were introduced to quantify the influence of damaging (f_{D}), length change (f_{L}), and the combination of both on the electrical resistance of a wave-shaped wire (f_{W}). Significant increase of the electrical resistance f_{W} between +3.5 and +82.7% caused by the reshaping process was identified.

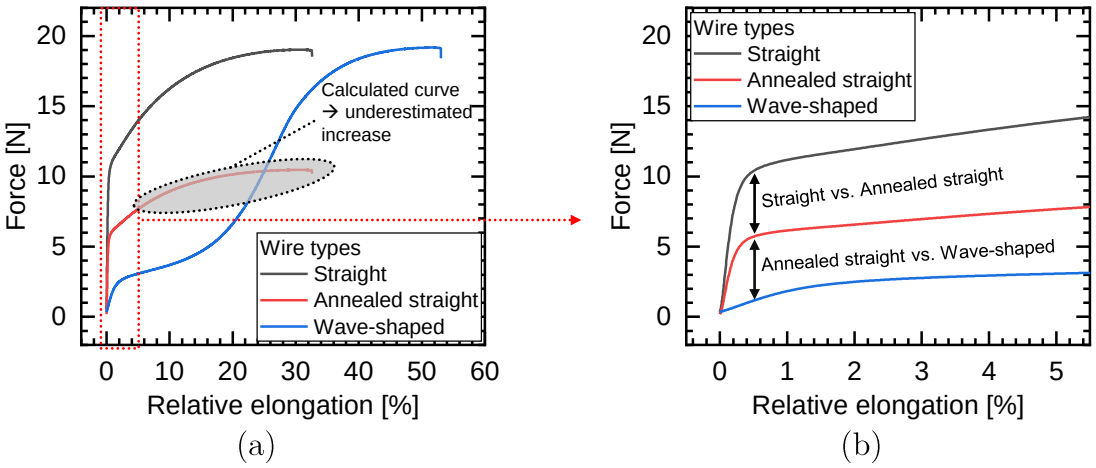

Figure 8.6: Comparison of the force-rel. elongation curves of a straight, an annealed straight, and a wave-shaped wire: (a) entire curves and (b) most relevant area below 5% relative elongation. The curves of the straight and the wave-shaped wire were measured by tensile tests. The hypothetical curve of an annealed straight wire is calculated by multiplication of the straight wire curve with 0.55, since the yield limit can be reduced by up to −45% using an enhanced thermal treatment according to Meier *et al.* [38].

8.4.4 Summary and outlook

On the one hand, the results demonstrate a significant yield limit reduction due to the pseudo yield limit of wave-shaped wires. This results in lower thermomechanical stress and presumably in an improved long-term stability of solar cell interconnections. On the other hand, the electrical resistance is increased by the adapted wire shape, which can be compensated by an increase of the number of wire interconnectors. Especially for BC solar cells this does not result in a reduced efficiency due to higher interconnector shading losses.

Another aspect is the challenging handling of wave-shaped wires in stringing machines. Wave-shaping of straight wires immediately before the soldering step to minimize handling effort is presumably the most promising approach. With Method 4 an approach based on bending elements and feeding wheels was already tested to potentially integrate the wave-shaping process for wire interconnectors in solar cell stringing machines. As next steps this process can be further optimized, and the parallel deformation of several wire interconnectors, as well as the integration into

stringing machines for wire interconnection should be tested. This approach also enables to reshape only parts of interconnectors, which may reduce thermomechanical stress in most crucial areas and, at the same time, reduce the increase of the series resistance, which is beneficial for the efficiency of a PV module.

8.5 Application and technological properties of wave-shaped wires

8.5.1 Motivation and approach

The potential output power of PV modules including solar cells interconnected by wave-shaped wires was simulated. Especially for half-solar cells the results indicate potential output power gains when using wave-shaped wires combined with solar cells without busbars or pads rows instead of common busbar- and ribbon-based or interconnection with pad rows and straight wires. Measurements of the deformation and the long-term stability of solar cell sections connected on one side reveal the potential of wave-shaped wires for substantial stress reduction. As a result, wave-shaped wires enable soldering directly on the finger grid (instead of pads or busbars) of commercial solar cells with comparable long-term stability. In contrast to the patent application of Storbeck and Hahn the wave-shaped wire meanders in the surface of a solar cell, not perpendicular [124]. Furthermore, first experiments indicate that an interconnection of BC solar cells using wave-shaped wires is possible.

8.5.2 Efficiency of PV modules with wave-shaped wires

A CTM analysis shows that PV modules with MBB interconnection (12 wires) have the potential for higher output powers compared to 5BB interconnection. A relative power gain of +2.47% for full solar cells and +0.35% for half solar cells was simulated. The potential efficiency gain in this simulation is +0.43% abs. for PV modules including full solar cells (17.68% vs. 18.08%) and +0.07% abs. for half solar cells (18.28% vs. 18.35%). Potential gains in the same range have also been determined by Braun *et al.*, who measured an absolute efficiency gain of +0.32%

for wire interconnection of full solar cells compared to three ribbons on busbars for PV modules with an efficiency of about 18.5% [69].

The results show that the interconnection of full solar cells by wave-shaped wires soldered on the contact finger grid has the potential for output powers nearly as high as for MBB interconnection (−0.4% rel.) and about +2.1% rel. compared to a PV module with 5BB interconnection. For half solar cells the interconnection by wave-shaped wires shows the potential for the highest output power of a PV module, exceeding 5BB by +1.0% rel. and MBB by +0.7% rel. for the most powerful wire configuration using 12 wires with a diameter of 350 µm and an amplitude of 1.0 mm. This demonstrates that front-to-back interconnection of standard solar cells by wave-shaped wires potentially results in higher output power of a PV module compared to established interconnection approaches. The simulated power for an exemplary PV module setup with 5BB and MBB interconnection, as well as with the wave-shaped wire configuration with the maximum output power is shown by Figure 8.7.

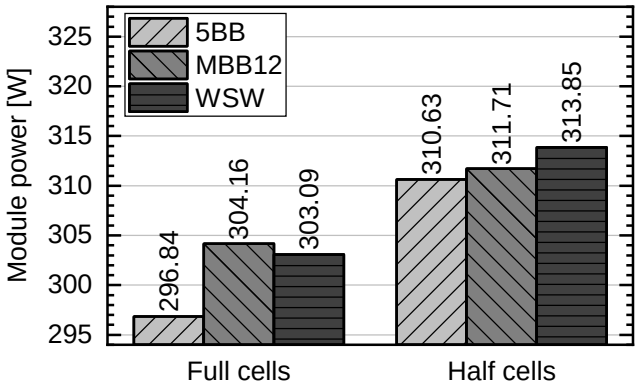

Figure 8.7: Simulation of the PV module power for 5BB, MBB (MBB12: 12 wires), and wave-shaped wires interconnection (WSW). For wave-shaped wires the configuration with the maximum power is shown (diameter: 350 µm, amplitude: 1.0 mm, period: 3.0 mm, wire number full cells: 12, wire number half cells: 6).

8.5.3 Thermomechanical stress and interconnection defects

Measurements of the maximum deformation of solar cell sections, connected by wave-shaped wires on one side, demonstrate that a reduced pseudo yield limit of an interconnector realized by changing its shape leads to lower thermomechanical stress after the soldering process (see Section 4.2.2). Zemen *et al.* also show a photograph of solar cell sections connected on one side only to visualize the impact of thermomechanical stress [40]. Lower deformation of solar cell sections with interconnectors with lower yield limit was also predicted by simulations, indicating a relative decrease of the deformation by -24% for an interconnector with a yield limit of 50 MPa instead of 100 MPa (see Section 3.3.1). The results are in agreement with findings of Meier *et al.* whose simulation indicates a decrease in first principal stress of about -30% for interconnectors with reduced yield limit (-45% reduction by optimized annealing) [38].

The long-term stability of solar cell sections connected by straight and wave-shaped wires was compared with soldering discrete wires on single pads. The results reveal that a serial interconnection of contact pads is more prone to defects in temperature cycling compared to single pad connection. Additionally, the results indicate that a reduction of thermomechanical stress by using wave-shaped wires results in an improved long-term stability of connected contact pad rows of solar cells. Presumably, there are two different mechanisms that cause defects of interconnections in temperature cycling:

- thermomechanical stress induced due to the serial interconnection of contact pads, which starts causing pad defects right from the start of temperature cycling, and
- deformation of joined materials due to different CTEs causing defects after a specific amount of thermal cycles.

Both failure mechanisms have to be taken into account for connected pad rows of silicon solar cells. Nevertheless, for serial interconnection of contact pads the weakest interconnections should fail at the beginning of temperature cycling because of the first failure mechanism (see Figure 4.8 (b)). However, these results demonstrate the potential of wave-shaped wires to improve the long-term stability of PV modules or to enable interconnection concepts based on fragile contacts.

8.5.4 Soldering on the contact finger grid

Since wave-shaped wire interconnectors enable a reduction of thermomechanical stress in solar cells soldering on very small contact pads or directly on the contact fingers is possible. Semi-automatic interconnection of commercially available solar cells by wave-shaped wires demonstrates the feasibility of an interconnection approach based on wave-shaped wires directly connecting the contact fingers of silicon solar cells. Interconnection of the finger grid leads to lower costs due to a significant reduction of the silver paste consumption, but is not possible with straight standard interconnectors (ribbons or wires). Additionally, less recombination losses at the metallization and solar cell interface potentially increase the efficiency of solar cells. Furthermore, with IR soldering and Pb-based solder an established interconnection process and a cost-efficient standard solder alloy can be used. In contrast, both alternatives that also enable the interconnection of solar cells without busbars or contact pads, the SWCT and concepts using ECAs, presumably lead to higher costs since ECAs or low-temperature solder alloys are more expensive compared to common solder alloys.

As expected, EL measurements on 8 mini-modules show that most interconnection defects occurred at the outermost pads, where the thermomechanical stress maxima are located according to FE analyses described in Section 3.3. In addition, EL measurements after accelerated temperature cycling indicate that initial defects, such as solar cell cracks, detachment of the metallization, etc., increase the probability for additional interconnection failures. Additional defects after temperature cycling are visible as darker areas and especially occur adjacent to areas where the mini-module samples already showed non-optimal established contacts or defects in the initial state. This indicates that the amount of initial defects has a strong influence on defects due to thermomechanical stress in temperature cycling. Particularly at the solar cell edges and near cell cracks the results show further damaging of the interconnections due to temperature cycling. Furthermore, the EL images indicate that the interconnections in the solar cell center are less affected by thermomechanical stress, which also proves the findings of FE analyses described in Chapter 3. Figure 8.8 shows EL images of two exemplary PV module samples after the lamination process (Initial), after 200 (aTC200), and after 400 accelerated thermal cycles (aTC400), one

with a full (M4) and one with a half solar cell (M7). The two PV module samples with maximum (M7) and minimum power degradation after 400 accelerated thermal cycles (M4) are shown.

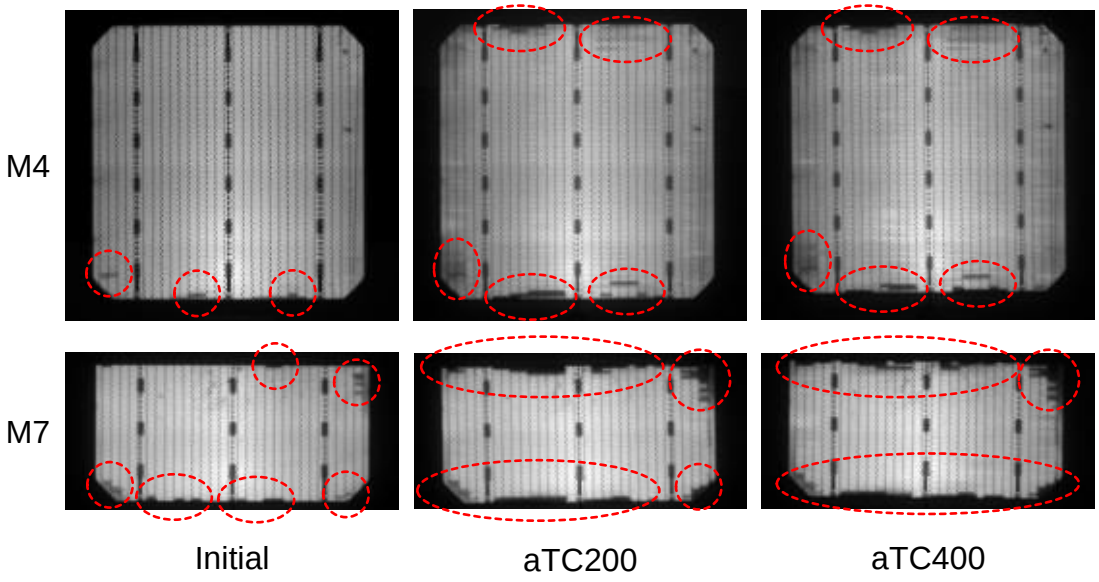

Figure 8.8: Two exemplary PV modules samples including one full (M4) and one half solar cell (M7) respectively. The solar cells are semi-automatically connected by wave-shaped wires on the finger grid. EL images after the lamination process (Initial), after 200 (aTC200), and after 400 accelerated thermal cycles (aTC400) are shown. Darker areas are indicated that show interconnection defects.

However, the electrical characterization after accelerated temperature cycling demonstrate that the reliability easily meets the requirements for PV modules with solar cell strings connected by conventional interconnection technologies. After 200 accelerated temperature cycles the power loss of all module samples (full and half solar cells) was below -3%. Only one module sample showed more than -5% power loss after 400 accelerated thermal cycles. The relative power of eight PV module samples after 200 (aTC200), and after 400 accelerated thermal cycles (aTC400) is shown by Figure 8.9.

8.5.5 Interconnection of BC solar cells

The interconnection of BC solar cells by wave-shaped wires was evaluated, which is also described by Krokoszinski and Amorim [125]. Initial EL images of first

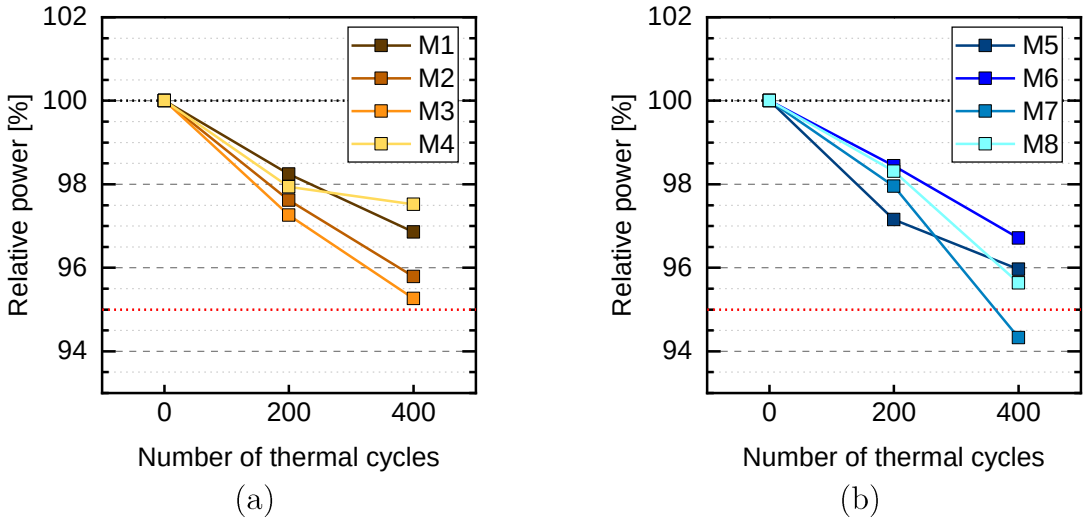

Figure 8.9: Relative power of eight PV module samples after 200 (aTC200) and after 400 accelerated thermal cycles (aTC400). Each PV module includes one solar cell semi-automatically connected by wave-shaped wires on the finger grid. The relative power is shown for (a) full, as well as (b) for half solar cells. The red dotted line indicates the maximum power loss after 200 thermal cycles of 5% according to the test standard for PV modules [19].

one-cell PV modules including BC solar cells connected by wave-shaped wires, four mini-modules with half and four mini-modules with full solar cells, show darker non-connected or defective areas, which indicate that some areas of the solar cells are not connected properly. This can be caused by several reasons, some possible explanations are the following:

- non-homogeneous heating by the IR lamps,
- insufficient or non-homogeneous vacuum suction, or
- detachment of the contact metallization due to low adhesion combined with (thermo-)mechanical stress caused by handling of the connected cells or temperature changes.

Further experiments are required to determine the major reasons for the interconnection problems. However, in some areas the EL images show no defects and the solar cells are connected properly. In addition, accelerated temperature cycling revealed a maximum relative power loss of -6.2% after 400 cycles. Unfortunately, there are no measurement results after 200 accelerated thermal cycles (due to wrong

measurement settings), but when assuming a linear degradation rate between 50 and 400 thermal cycles even these first samples meet the requirements of the test standard for PV modules of less than −5% relative power loss after 200 thermal cycles.

The results demonstrate that wave-shaped wires can potentially used for the interconnection of BC solar cells. Nevertheless, to manufacture high efficient and reliable PV modules further development of the solar cells, as well as of the IR-based interconnection process is needed to improve initial soldering results with a smaller number of pre-damaged interconnections. Presumably, the adhesion between contact metallization and silicon wafer surface and the homogeneity of vacuum suction and IR illumination are the main influence factors that could be improved.

8.5.6 Outlook

Several research and development aspects can be analyzed in future projects. First of all, the contact metallization of solar cells can be optimized for mechanical stability. Adapting the contact layout, choosing screen-printing pastes that lead to high adhesion forces, and parameter variations in the contact firing process are possible optimizations. An increase of the width of the outermost fingers or adding protective pads located near the solar cell edges potentially leads to further improvements of the mechanical long-term stability of the outermost interconnections. However, this work was focused on the interconnectors and their influence on the mechanical stability of the interconnections in a PV module. For this reason, important aspects can be further analyzed as a follow up. For wave-shaped wires with lower diameters, higher amplitudes, or when soldering of less than 30 wires an improved reliability can be expected. Furthermore, the Restriction of the use of certain hazardous substances in electrical and electronic equipment (RoHS) confines the use of Pb-based solders in electronic components in the European Union. Currently there exists a special permission for PV modules for the use of metallization pastes including Pb and Pb-based solder alloys with low melting points, but this may change in the future. Using metallization pastes and solder alloys without Pb potentially results in lower reliability and higher costs. For example, Bi-based solder alloys, which are nowadays the most promising candidates, tend to be more expensive and brittle. By using

wave-shaped wires reliability issues with Bi-based solders may be less crucial. In addition, manufacturing full format PV modules, including at least 60 full or 120 half solar cells, can be tested to determine the potential power gains of PV modules with solar cells interconnected by wave-shaped wires. Experiment results indicate that an interconnection of common solar cells (front-to-back interconnection) omitting busbars and contact pads by soldering wave-shaped wires on the finger grid is possible, also for full-size PV modules.

9 Summary

This work aimed to identify critical influence factors and to develop interconnection approaches for solar cells that substantially reduce (thermo-)mechanical stress in PV modules. To localize stress maxima and to identify major influence factors the stress distribution in interconnected solar cells was investigated by FE analyses. An approach based on compliant wave-shaped wire interconnectors was developed to interconnect silicon solar cells. The main goal was to reduce thermomechanical stress in order to improve the long-term stability and the energy yield of PV modules.

The standard interconnection technology uses copper ribbons soldered on both sides of silicon solar cells. Different CTEs of the silicon wafer and the copper interconnectors cause thermomechanical stress upon temperature changes. For single-side interconnection of back-contact solar cells with high efficiencies, additionally bending after the interconnection process is an issue. Consequently, defects can occur that significantly accelerate degradation and reduce the output power of PV modules. For two different interconnection concepts used in PV module production, one using busbars and ribbon interconnectors, another based on contact pad rows and round wires, the distribution of the thermomechanical stress after soldering was analyzed by simulations. For both concepts, the results reveal significant stress maxima located at the outermost contacts. Additionally, the influence of the contact metallization layout was analyzed, aiming to minimize thermomechanical stress. The following guidelines potentially result in improved long-term stability of PV modules: contact pad rows instead of continuous busbars, small contact pad length and distance, large protective outermost contacts pads, and an optimized distance between outermost contacts and the solar cell edge. However, also the mechanical properties of the interconnectors affect thermomechanical stress in solar cells.

Reshaping of copper-based wire interconnectors substantially influences their properties. Four different reshaping methods were evaluated using newly developed wave-shaping machines, of which two methods were selected for in detail analyses. One method works with two specially designed, synchronously rotating toothed wheels, resulting in negligible defects and well-controlled geometries of wave-shaped

wires. The second method uses bending elements and feeding wheels, which enables reshaping of many wire interconnectors in parallel. Furthermore, it enables an integration of the reshaping process in industrial stringing machines. Microscopic imaging revealed a maximum relative amplitude deviation of 6.5% compared to the target values. A relative yield limit reduction up to −88.5% was shown by standard tensile tests of wave-shaped wires with a pseudo yield limit, which demonstrates a substantially increased compliance. The measured length change indicates the additional amount of interconnector material. Electrical resistance measurements show a relative increase up to +82.7%.

The simulation of the output power of PV modules with solar cells interconnected by wave-shaped wires shows a relative output power increase up to 2.1% compared to the standard approaches. Wave-shaped wires were semi-automatically soldered on two types of solar cells; on the finger grid of commercially available solar cells and on newly developed BC solar cells with contact pads. Only few defective areas near the solar cell edges were detected by EL imaging after soldering and after module encapsulation of the first type of solar cells. This is in accordance with the simulation results, showing maximum stress at the outermost contacts. EL images reveal further damaging at the solar cell edges after temperature cycling, but IV measurements show a power degradation of less than −3% after 200 cycles for all module samples, which meets the requirement of the test standard for PV modules (less than −5% after 200 thermal cycles). After 400 cycles, only one test-module exceeded −5% power degradation, which proves that soldering of wave-shaped wires on solar cells with small contacts is possible. EL images of first back-contact solar cells connected by wave-shaped wires show more significant damaging. Although the damages after interconnection are more severe, the results of these pilot experiments are very promising, since first test-modules show relative power degradation levels after temperature cycling that meet the requirements of the test standard for PV modules.

Based on the identification of major influence factors causing thermomechanical stress, a novel, promising approach to interconnect silicon solar cells by wave-shaped wires was developed. Compared to current standard technologies, interconnection by wave-shaped wires enables substantial reductions of (thermo-)mechanical stress and potentially improves the initial efficiency and energy yield of PV modules.

Bibliography

[1] J. Rogelj, M. den Elzen, N. Höhne, T. Fransen, H. Fekete, H. Winkler, R. Schaeffer, F. Sha, K. Riahi, and M. Meinshausen, "Paris Agreement climate proposals need a boost to keep warming well below 2 °C," *Nature*, vol. 534, pp. 631–639, 2016. DOI: 10.1038/nature18307.

[2] *Adoption of the paris agreement*, United Nations: Framework Convention on Climate Change, Paris, France, FCCC/CP/2015/L.9/Rev.1, 30 November to 11 December 2015, Accessed: December 4, 2018. [Online]. Available: http://unfccc.int/resource/docs/2015/cop21/eng/l09r01.pdf.

[3] T. R. Anderson, E. Hawkins, and P. D. Jones, "CO_2, the greenhouse effect and global warming: From the pioneering work of Arrhenius and Callendar to today's Earth System Models," *Endeavour*, vol. 40, pp. 178–187, 2016. DOI: 10.1016/j.endeavour.2016.07.002.

[4] A. A. Lacis, G. A. Schmidt, D. Rind, and R. A. Ruedy, "Atmospheric CO2: Principal control knob governing earth's temperature," *Science*, vol. 330, pp. 356–359, 2010. DOI: 10.1126/science.1190653.

[5] *Key world energy statistics: 2019*, International Energy Agency, 2019, Accessed: January 17, 2020. [Online]. Available: https://webstore.iea.org/key-world-energy-statistics-2019.

[6] *Renewables 2018 global status report*, REN21, 2018, Accessed: April 23, 2021. [Online]. Available: https://www.ren21.net/gsr-2018/.

[7] G. A. Marrero, "Greenhouse gases emissions, growth and the energy mix in Europe," *Energy Economics*, vol. 32, pp. 1356–1363, 2010. DOI: 10.1016/j.eneco.2010.09.007.

[8] N. Abas, A. Kalair, and N. Khan, "Review of fossil fuels and future energy technologies," *Futures*, vol. 69, pp. 31–49, 2015. DOI: 10.1016/j.futures.2015.03.003.

[9] *Shell scenarios Sky: Meeting the goals of the Paris Agreement*, Shell International B.V. 2018, Accessed: June 2, 2019. [Online]. Available: www.shell.com/skyscenario.

[10] C. Binz, T. Tang, and J. Huenteler, "Spatial lifecycles of cleantech industries – the global development history of solar photovoltaics," *Energy Policy*, vol. 101, pp. 386–402, 2017. DOI: 10.1016/j.enpol.2016.10.034.

[11] S. Philipps and W. Warmuth, *Photovoltaics report*, Fraunhofer Institute for Solar Energy Systems ISE with support of PSE GmbH, 2019, Accessed: Jan. 17, 2020. [Online]. Available: https://www.ise.fraunhofer.de/de/veroeffentlichungen/studien/photovoltaics-report.html.

[12] *International Technology Roadmap for Photovoltaic (ITRPV): Results 2017, 9th edition*, VDMA Photovoltaic Equipment, 2018, Accessed: Feb 5, 2019. [Online]. Available: https://itrpv.vdma.org/viewer/-/v2article/render/29775594.

[13] M. A. Green, Y. Hishikawa, E. D. Dunlop, D. H. Levi, J. Hohl-Ebinger, and A. W. Ho-Baillie, "Solar cell efficiency tables (version 52)," *Progress in Photovoltaics*, vol. 26, p. 10, 2018. DOI: 10.1002/pip.3040.

[14] X. F. Brun and S. N. Melkote, "Analysis of stresses and breakage of crystalline silicon wafers during handling and transport," *Solar Energy Materials and Solar Cells*, vol. 93, pp. 1238–1247, 2009. DOI: 10.1016/j.solmat.2009.01.016.

[15] A. M. Gabor, M. Ralli, S. Montminy, L. Alegria, C. Bordonaro, J. Woods, and L. Felton, "Soldering induced damage to thin Si solar cells and detection of cracked cells in modules," in *Proceedings of the 21st European Photovoltaic Solar Energy Conference and Exhibition*, 2006, pp. 2042–2047.

[16] S. Wiese, R. Meier, F. Kraemer, and J. Bagdahn, "Constitutive behaviour of copper ribbons used in solar cell assembly processes," in *Proceedings of the 10th IEEE International Conference on Thermal, Mechanical and Multi-Physics Simulation and Experiments in Microelectronics and Microsystems*, 2009, p. 8. DOI: 10.1109/esime.2009.4938464.

[17] D. L. King, M. A. Quintana, J. A. Kratochvil, D. E. Ellibee, and B. R. Hansen, "Photovoltaic module performance and durability following long-term field exposure," *Progress in Photovoltaics*, vol. 8, pp. 241–256, 2000. DOI: 10.1063/1.58001.

[18] M. Köntges, S. Kurtz, C. Packard, U. Jahn, K. A. Berger, K. Kato, T. Friesen, H. Liu, and M. van Iseghem, *Review of failures of photovoltaic modules*,

IEA International Energy Agency, 2014, Accessed: April 26, 2021. [Online]. Available: https://iea-pvps.org/key-topics/review-of-failures-of-photovoltaic-modules-final/.

[19] *Terrestrial photovoltaic (PV) modules – design qualification and type approval – part 2: Test procedures: IEC 61215-2:2016*, 2016.

[20] J. H. Wohlgemuth, "Reliability testing of pv modules," in *Proceedings of 1994 IEEE 1st World Conference on Photovoltaic Energy Conversion - WCPEC (A Joint Conference of PVSC, PVSEC and PSEC)*, 1994, pp. 889–892. DOI: 10.1109/WCPEC.1994.520104.

[21] C. R. Osterwald and T. J. McMahon, "History of accelerated and qualification testing of terrestrial photovoltaic modules: A literature review," *Progress in Photovoltaics*, vol. 17, pp. 11–33, 2009. DOI: 10.1002/pip.861.

[22] C. Ferrara and D. Philipp, "Why do PV modules fail?" *Energy Procedia*, vol. 15, pp. 379–387, 2012. DOI: 10.1016/j.egypro.2012.02.046.

[23] J. Wendt, M. Traeger, M. Mette, A. Pfennig, and B. Jaeckel, "The link between mechanical stress induced by soldering and micro damages in silicon solar cells," in *Proceedings of the 24th European Photovoltaic Solar Energy Conference and Exhibition*, 2009, pp. 3420–3423. DOI: 10.4229/24thEUPVSEC2009-4AV.3.40.

[24] M. Sander, S. Dietrich, M. Pander, M. Ebert, M. Karrass, R. Lippmann, M. Broddack, and D. Wald, "Influence of manufacturing processes and subsequent weathering on the occurrence of cell cracks in PV modules," in *Proceedings of the 28th European Photovoltaic Solar Energy Conference and Exhibition*, 2013, pp. 3275–3279. DOI: 10.4229/28thEUPVSEC2013-4AV.5.30.

[25] W. Carroll, E. Cuddihy, and M. Salama, "Material and design considerations of encapsulants for photovoltaic arrays in terrestrial applications," in *Proceedings of the 12th IEEE photovoltaic specialists' conference*, 1976, p. 8.

[26] G. Mesch, *High temperature - low mass solar blanket*, Jet Propulsion Laboratory, Redondo Beach, CA, USA, JPL Contract No. 955139, 1979.

[27] U. Eitner, "Thermomechanics of photovoltaic modules," Ph.D. dissertation, Martin-Luther-Universität, Halle-Wittenberg, Germany, 2011.

[28] A. J. Beinert, M. Ebert, U. Eitner, and J. Aktaa, "Influence of photovoltaic module mounting systems on the thermo-mechanical stresses in solar cells

by FEM modelling," in *Proceedings of the 32nd European Photovoltaic Solar Energy Conference and Exhibition*, 2016, pp. 1833–1836. DOI: 10.4229/EUPVSEC20162016-5BV.1.14.

[29] A. J. Beinert, R. Leidl, P. Sommeling, U. Eitner, and J. Aktaa, "FEM-based development of novel back-contact PV modules with ultra-thin solar cells," in *Proceedings of the 33rd European Photovoltaic Solar Energy Conference and Exhibition*, 2017, pp. 42–47. DOI: 10.4229/EUPVSEC20172017-1CO.1.2.

[30] F. Kraemer, S. Wiese, E. Peter, and J. Seib, "Mechanical problems of novel back contact solar modules," *Microelectronics Reliability*, vol. 53, pp. 1095–1100, 2013. DOI: 10.1016/j.microrel.2013.02.019.

[31] F. Kraemer, J. Seib, E. Peter, and S. Wiese, "Mechanical stress analysis in photovoltaic cells during the string-ribbon interconnection process: 17th international conference on thermal, mechanical and multi-physics simulation and experiments in microelectronics," in *15th International Conference on Thermal, Mechanical and Mulit-Physics Simulation and Experiments in Microelectronics and Microsystems*, 2014, p. 7. DOI: 10.1109/EuroSimE.2014.6813853.

[32] F. Kraemer and S. Wiese, "Assessment of long term reliability of photovoltaic glass–glass modules vs. glass-back sheet modules subjected to temperature cycles by FE-analysis," *Microelectronics Reliability*, vol. 55, pp. 716–721, 2015. DOI: 10.1016/j.microrel.2015.02.007.

[33] A. J. Beinert, P. Romer, A. Büchler, V. Haueisen, J. Aktaa, and U. Eitner, "Thermomechanical stress analysis of PV module production processes by Raman spectroscopy and FEM simulation," *Energy Procedia*, vol. 124, pp. 464–469, 2017. DOI: 10.1016/j.egypro.2017.09.282.

[34] A. J. Beinert, A. Büchler, P. Romer, V. Haueisen, L. C. Rendler, M. C. Schubert, M. Heinrich, J. Aktaa, and U. Eitner, "Enabling the measurement of thermomechanical stress in solar cells and PV modules by confocal micro-Raman spectroscopy," *Solar Energy Materials and Solar Cells*, vol. 193, pp. 351–360, 2019. DOI: 10.1016/j.solmat.2019.01.028.

[35] C.-M. Lai, K.-M. Lin, and C.-H. Su, "The effects of cracks on the thermal stress induced by soldering in monocrystalline silicon cells," *Proceedings of the*

Institution of Mechanical Engineers, Part E: Journal of Process Mechanical Engineering, vol. 228, pp. 127–135, 2013. DOI: 10.1177/0954408913487285.

[36] R. E. Patterson, *Development of technologies for welding interconnects to fifty-micron thick silicon solar cells*, Jet Propulsion Laboratory, Redondo Beach, CA, USA, JPL Contract 956042, 1982.

[37] R. E. Patterson, *NASA welding assessment program*, Jet Propulsion Laboratory, Redondo Beach, CA, USA, JPL Contract 956042, 1985.

[38] R. Meier, M. Pander, R. Klengel, S. Dietrich, S. Klengel, M. Ebert, and J. Bagdahn, "Reduction of soldering induced stresses in solar cells by microstructural optimization of copper-ribbons," in *Proceedings SPIE 8112*, p. 13. DOI: 10.1117/12.893519.

[39] J. Walter, L. C. Rendler, A. Halm, V. Mihailetchi, A. Kraft, and U. Eitner, "Ribbon interconnection of 6" BC-BJ solar cells," *Energy Procedia*, vol. 124, pp. 504–514, 2017. DOI: 10.1016/j.egypro.2017.09.287.

[40] Y. Zemen, Prewitz T., T. Geipel, S. Pingel, and J. Berghold, "The impact of yield strength of the interconnector on the internal stress of the solar cell within a module," in *Proceedings of the 25th European Photovoltaic Solar Energy Conference and Exhibition/5th World Conference on Energy Conversion*, 2010, pp. 4073–4078. DOI: 10.4229/25thEUPVSEC2010-4AV.3.38.

[41] U. Eitner, D. Eberlein, and M. Tranitz, "Interconnector-based module technology for thin MWT cells," in *Proceedings of the 27th European Photovoltaic Solar Energy Conference and Exhibition*, 2012, pp. 3461–3464. DOI: 10.4229/27thEUPVSEC2012-4BV.3.14.

[42] W. Song, S. K. Tippabhotla, A. Tay, and A. S. Budiman, "Effect of interconnect geometry on the evolution of stresses in a solar photovoltaic laminate during and after lamination," *Solar Energy Materials and Solar Cells*, vol. 187, pp. 241–248, 2018. DOI: 10.1016/j.solmat.2018.07.026.

[43] W. Luft, "Solar cell interconnector design," *IEEE Transactions on Aerospace and Electronic Systems*, vol. AES-7, pp. 781–791, 1971. DOI: 10.1109/TAES.1971.310318.

[44] W. Luft and E. Maiden, "Temperature cycling effects on solar panels," *IEEE Transactions on Aerospace and Electronic Systems*, vol. AES-5, pp. 943–950, 1969. DOI: 10.1109/TAES.1969.309970.

[45] S. Dietrich, M. Pander, M. Sander, and M. Ebert, "Mechanical investigations on metallization layouts of solar cells with respect to module reliability," *Energy Procedia*, vol. 38, pp. 488–497, 2013. DOI: 10.1016/j.egypro.2013.07.308.

[46] C. Kohn, R. Kübler, M. Krappitz, G. Kleer, I. Reis, M. Retzlaff, D. Erath, and D. Biro, "Influence of the metallization process on the strength of silicon solar cells," in *Proceedings of the 24th European Photovoltaic Solar Energy Conference and Exhibition*, 2009, pp. 1419–1423. DOI: 10.4229/24thEUPVSEC2009-2CV.2.4.

[47] J. Moyer, W. Zhang, E. Kurtz, R. Tavares, D. Buzby, and S. Kleinbach, "The role of silver contact paste on reliable connectivity systems," in *Proceedings of the 25th European Photovoltaic Solar Energy Conference and Exhibition/5th World Conference on Energy Conversion*, 2010, pp. 2624–2630. DOI: 10.4229/25thEUPVSEC2010-2DV.1.68.

[48] S. Wiese, F. Kraemer, N. Betzl, and D. Wald, "Interconnection technologies for photovoltaic modules - analysis of technological and mechanical problems," in *Proceedings of the 11th IEEE International Conference on Thermal, Mechanical and Multi-Physics Simulation and Experiments in Microelectronics and Microsystems*, 2010, p. 6. DOI: 10.1109/esime.2010.5464518.

[49] K. Yoshikawa, H. Kawasaki, W. Yoshida, T. Irie, K. Konishi, K. Nakano, T. Uto, D. Adachi, M. Kanematsu, H. Uzu, and K. Yamamoto, "Silicon heterojunction solar cell with interdigitated back contacts for a photoconversion efficiency over 26%," *Nature Energy*, vol. 2, p. 8, 2017. DOI: 10.1038/nenergy.2017.32.

[50] U. Gangopadhyay, K.-H. Kim, P. K. Basu, S. K. Dhungel, S.-W. Jung, and J.-S. Yia, "Front surface grid design for high efficiency solar cells," *Transactions on Electrical and Electronic Materials*, vol. 6, pp. 78–84, 2005. DOI: 10.4313/TEEM.2005.6.2.078.

[51] A. R. Burgers, "New metallisation patterns and analysis of light trapping for silicon solar cells," Ph.D. dissertation, Utrecht University, Utrecht, Netherlands, 2005.

[52] M. A. Green, *Solar Cells: Operating Principles, Technology and System Applications*. Englewood Cliffs, N.J., USA: Prentice-Hall Inc., 1998, ISBN: 0-13-82270.

[53] S. Schindler, J. Schneider, C. Poenisch, R. Nissler, and D. Habermann, "Soldering process and material characterization of miniaturized contact structures of a newly developed multi busbar cell metallization concept," in *Proceedings of the 28th European Photovoltaic Solar Energy Conference and Exhibition*, 2013, pp. 480–483. DOI: 10.4229/28thEUPVSEC2013-1CV.2.13.

[54] J. Walter, M. Tranitz, M. Volk, M. Ebert, and U. Eitner, "Multi-wire interconnection of busbar-free solar cells," *Energy Procedia*, vol. 55, pp. 380–388, 2014. DOI: 10.1016/j.egypro.2014.08.109.

[55] A. Schneider, L. Rubin, and G. Rubin, "Solar cell efficiency improvement by new metallization techniques - the day4™ electrode concept," in *Proceedings of the 4th IEEE World Conference on Photovoltaic Energy Conversion*, 2006, pp. 1095–1098. DOI: 10.1109/wcpec.2006.279333.

[56] T. Soederstroem, P. Papet, and J. Ufheil, "Smart wire connection technology," in *Proceedings of the 28th European Photovoltaic Solar Energy Conference and Exhibition*, 2013, pp. 495–499. DOI: 10.4229/28thEUPVSEC2013-1CV.2.17.

[57] S. S. Hegedus and A. Luque, *Handbook of Photovoltaic Science and Engineering*. Chichester, England: John Wiley & Sons Ltd, 2003, ISBN: 0-471-49196-9.

[58] G. Masson and I. Kaizuka, *Trends 2018 in photovoltaic applications: Survey report of selected IEA countries between 1992 and 2017*, IEA International Energy Agency, 2018, Accessed: April 2, 2019. [Online]. Available: http://www.iea-pvps.org/.

[59] S. Guo, J. P. Singh, I. M. Peters, A. G. Aberle, and T. M. Walsh, "A quantitative analysis of photovoltaic modules using halved cells," *International Journal of Photoenergy*, vol. 2013, p. 8, 2013. DOI: 10.1155/2013/739374.

[60] S. Krauter, *Solar Electric Power Generation*, 1st ed. Berlin, Heidelberg, New York: Springer-Verlag, 2006, ISBN: 3-540-31345-1.

[61] T. Geipel, M. Moeller, J. Walter, A. Kraft, and U. Eitner, "Intermetallic compounds in solar cell interconnections: Microstructure and growth kinetics," *Solar Energy Materials and Solar Cells*, vol. 159, pp. 370–388, 2017. DOI: 10.1016/j.solmat.2016.08.039.

[62] S. Chunduri and M. Schmela, *Market survey cell interconnection equipment 2017*, TaiyangNews, 2017, Accessed: February 25, 2020. [Online]. Available: http://taiyangnews.info/reports/market-survey-on-cell-interconnection-equipment/.

[63] *Preisverdächtig nach München: LG Electronics mit neuem NeON 2 und Cello-Technologie Anwärter auf Intersolar Award 2015*, LG Electronics, Press Release: May 11, 2015, Accessed: June 21, 2017. [Online]. Available: http://presse.lge.de/2015/05/11/preisverdaechtig-nach-muenchen-lg-electronics-mit-neuem-neon-2-und-cello-technologie-anwaerter-auf-intersolar-award-2015/.

[64] B. A. Korevaar, J. A. Fronheiser, X. Zhang, L. M. Fedor, and T. R. Tolliver, "Influence of annealing on performance for hetero-junction a-Si/c-Si devices," in *Proceedings of the 23rd European Photovoltaic Solar Energy Conference and Exhibition*, 2008, pp. 1859–1862. DOI: 10.4229/23rdEUPVSEC2008-2DV.1.7.

[65] P. Papet, R. Efinger, B. Sadlik, Y. Andrault, D. Bätzner, D. Lachenal, B. Strahm, G. Wahli, F. Wuensch, W. Frammelsberger, W. Stein, L. Rubin, W. Schmutz, A. Buechel, and B. Rau, "19% efficiency module based on Roth & Rau heterojunction solar cells and Day4Energy module concept," in *Proceedings of the 26th European Photovoltaic Solar Energy Conference and Exhibition*, 2011, pp. 3336–3339. DOI: 10.4229/26thEUPVSEC2011-4AV.1.13.

[66] S. De Wolf and M. Kondo, "Nature of doped a-Si:H/c-Si interface recombination," *Journal of Applied Physics*, vol. 105, p. 6, 2009. DOI: 10.1063/1.3129578.

[67] L. B. Rubin and G. L. Rubin, "Elektrode für fotovoltaische Zellen, fotovoltaische Zelle und fotovoltaischer Modul," German Patent 10239845, 2003.

[68] S. Braun, G. Micard, and G. Hahn, "Solar cell improvement by using a multi busbar design as front electrode," *Energy Procedia*, vol. 27, pp. 227–233, 2012. DOI: 10.1016/j.egypro.2012.07.056.

[69] S. Braun, G. Hahn, R. Nissler, C. Pönisch, and D. Habermann, "Multi-busbar solar cells and modules: High efficiencies and low silver consumption," *Energy Procedia*, vol. 38, pp. 334–339, 2013. DOI: 10.1016/j.egypro.2013.07.286.

[70] A. F. Dethlefsen, M. Volk, K. Ramspeck, and C. Buchner, "Reliability testing of multi-busbar modules," in *Proceedings of the 29th European Photovoltaic*

Solar Energy Conference and Exhibition, 2014, pp. 3323–3326. DOI: 10.4229/EUPVSEC20142014-5CV.2.38.

[71] T. L. Young, K. Hee, A. J. Lennon, R. J. Egan, O. Wilkie, and Y. Yao, "Design and characterization of an adhesion strength tester for evaluating metal contacts on silicon solar cells," in *40th IEEE Photovoltaic Specialists Conference*, 2014, pp. 2550–2553. DOI: 10.1109/PVSC.2014.6925450.

[72] P. Chaturvedi, B. Hoex, and T. M. Walsh, "Broken metal fingers in silicon wafer solar cells and pv modules," *Solar Energy Materials and Solar Cells*, vol. 108, pp. 78–81, 2013. DOI: 10.1016/j.solmat.2012.09.013.

[73] A. Schneider, R. Harney, S. Aulehla, S. Hummel, E. Lemp, S. Koch, and K. Schröder, "Conductive gluing as interconnection technique towards solar cells without front busbars and rear pads," in *Proceedings of the 27th European Photovoltaic Solar Energy Conference and Exhibition*, 2012, pp. 335–339. DOI: 10.4229/27thEUPVSEC2012-1BV.7.33.

[74] T. Geipel, M. Z. Huq, and U. Eitner, "Reliable interconnection of the front side grid fingers using silver-reduced conductive adhesives," *Energy Procedia*, vol. 55, p. 6, 2014. DOI: 10.1016/j.egypro.2014.08.098.

[75] P. Papet, L. Andreetta, D. Lachenal, G. Wahli, J. Meixenberger, B. Legradic, W. Frammelsberger, D. Bätzner, B. Strahm, Y. Yao, and T. Söderström, "New cell metallization patterns for heterojunction solar cells interconnected by the smart wire connection technology," *Energy Procedia*, vol. 67, pp. 203–209, 2015. DOI: 10.1016/j.egypro.2015.03.039.

[76] F. Clement, "Die Metal Wrap Through Solarzelle - Entwicklung und Charakterisierung," Ph.D. dissertation, Albert-Ludwigs-Universität, Freiburg, Germany, 2009.

[77] M. Hendrichs, "Industrielle Metallisierungskonzepte für siliziumbasierte Rückkontaktsolarzellen," Ph.D. dissertation, Technische Universität Berlin, Berlin, Germany, 2016.

[78] A. Halm, V. D. Mihailetchi, G. Galbiati, L. J. Koduvelikulathu, R. Roescu, C. Comparotto, R. Kopecek, K. Peter, and J. Libal, "The Zebra cell concept-large area n-type interdigitated back contact solar cells and one-cell modules fabricated using standard industrial processing equipment," in *Proceedings*

of the 27th European Photovoltaic Solar Energy Conference and Exhibition, 2012, pp. 567–570. DOI: 10.4229/27thEUPVSEC2012-2AO.2.1.

[79] Z. Campeau, M. Anderson, E. Hasselbrink, D. Kavulak, Y.-C. Shen, R. Lacerda, A. Terao, S. Caldwell, Z. Defreitas, L. Leonard, M. Mikofski, D. DeGraaff, and A. Budiman, *Sunpower module degradation rate*, SunPower Corporation, 2013, Accessed: June 21, 2017. [Online]. Available: https://us.sunpower.com/sites/sunpower/files/media-library/white-papers/wp-sunpower-module-degradation-rate.pdf.

[80] J. Bultman, M. Brieko, A. Burgers, J. Hoornstra, A. Tip, and A. Weeber, "Interconnection through vias for improved efficiency and easy module manufacturing of crystalline silicon solar cells," *Solar Energy Materials and Solar Cells*, vol. 65, pp. 339–345, 2001. DOI: 10.1016/S0927-0248(00)00111-2.

[81] M. Spath, P. C. de Jong, I. J. Bennett, T. P. Visser, and J. Bakker, "A novel module assembly line using back contact solar cells," in *Proceedings of the 33rd IEEE Photovoltaic Specialists Conference*, 2008, p. 6. DOI: 10.1109/PVSC.2008.4922528.

[82] A. Halm, B. de Gier, A. Schneider, v.d. Mihailetchi, L. J. Koduvelikulathu, G. Galbiati, H. Chu, R. Roescu, J. Libal, N. van Ommen, and R. Kopecek, "Results on module integration of ibc solar cells based on the conductive backsheet approach," in *Proceedings of the 32nd European Photovoltaic Solar Energy Conference and Exhibition*, 2016, pp. 53–55. DOI: 10.4229/EUPVSEC20162016-1BO.12.4.

[83] A. Spribille, J. D. Huyeng, T. Schweigstill, I. Franzetti, L. C. Rendler, and F. Clement, "Electrode design for wire interconnected back contact solar cells," in *Proceedings of the 36th European Photovoltaic Solar Energy Conference and Exhibition*, 2019, pp. 196–200. DOI: 10.4229/EUPVSEC20192019-2BO.4.2.

[84] T. Borgers, J. Govaerts, E. Voroshazi, S. Jambaldinni, B. O'Sullivan, S. Singh, M. Debucquoy, J. Szlufcik, and J. Poortmans, "A woven fabric for interconnecting back-contact solar cells," *Progress in Photovoltaics: Research and Applications*, vol. 25, pp. 569–582, 2017. DOI: 10.1002/pip.2851.

[85] W. Kylberg, F. A. Castro, P. Chabrecek, T. Geiger, J. Heier, P. G. Nicholson, F. Nüesch, E. Theocharous, U. Sonderegger, and R. Hany, "Spatially resolved photocurrent mapping of efficient organic solar cells fabricated on a woven

mesh electrode," *Progress in Photovoltaics: Research and Applications*, vol. 21, pp. 652–657, 2013. DOI: 10.1002/pip.1242.

[86] S. Wiese, R. Meier, and F. Kraemer, "Mechanical behaviour and fatigue of copper ribbons used as solar cell interconnectors," in *Proceedings of the 11th IEEE International Conference on Thermal, Mechanical and Multi-Physics Simulation and Experiments in Microelectronics and Microsystems*, 2010, p. 5. DOI: 10.1109/esime.2010.5464551.

[87] K. G. Lyon, G. L. Salinger, C. A. Swenson, and G. K. White, "Linear thermal expansion measurements on silicon from 6 to 340 K," *Journal of Applied Physics*, vol. 48, pp. 865–868, 1977. DOI: 10.1063/1.323747.

[88] U. Eitner, S. Kajari-Schroeder, M. Koentges, and H. Altenbach, "Thermal stress and strain of solar cells in photovoltaic modules," in *Shell-like Structures*, Berlin / Heidelberg, Germany: Springer, 2011, pp. 453–468. DOI: 10.1007/978-3-642-21855-2.

[89] J.-S. Jeong, N. Park, and C. Han, "Field failure mechanism study of solder interconnection for crystalline silicon photovoltaic module," *Microelectronics Reliability*, vol. 52, pp. 2326–2330, 2012. DOI: 10.1016/j.microrel.2012.06.027.

[90] J. Käsewieter, F. Haase, M. H. Larrodé, and M. Köntges, "Cracks in solar cell metallization leading to module power loss under mechanical loads," *Energy Procedia*, vol. 55, pp. 469–477, 2014. DOI: 10.1016/j.egypro.2014.08.011.

[91] J. Käsewieter, F. Haase, and M. Köntges, "Model of cracked solar cell metallization leading to permanent module power loss," *IEEE Journal of Photovoltaics*, vol. 6, pp. 28–33, 2016. DOI: 10.1109/JPHOTOV.2015.2487829.

[92] M. Köntges, G. Oreski, U. Jahn, M. Herz, P. Hacke, K.-A. Weiß, G. Razongles, M. Paggi, D. Parlevliet, T. Tanahashi, and R. H. French, *Assessment of photovoltaic module failures in the field*, International Energy Agency, 2017, Accessed: April 23, 2021. [Online]. Available: http://iea-pvps.org/index.php?id=435.

[93] E. J. Schneller, R. P. Brooker, N. S. Shiradkar, M. P. Rodgers, N. G. Dhere, K. O. Davis, H. P. Seigneur, N. Mohajeri, J. Wohlgemuth, G. Scardera, A. C. Rudack, and W. V. Schoenfeld, "Manufacturing metrology for c-Si module reliability and durability part III: Module manufacturing," *Renewable*

and Sustainable Energy Reviews, vol. 59, pp. 992–1016, 2016. DOI: 10.1016/j.rser.2015.12.215.

[94] B. Sopori, P. Sheldon, and P. Rupnowski, "Wafer breakage mechanism(s) and a method for screening "problem wafers"," in *Proceedings of the 16th Workshop on Crystalline Silicon Solar Cells and Modules*, 2006, pp. 129–138.

[95] L. C. Rendler, P. Romer, A. J. Beinert, J. Walter, S. Stecklum, A. Kraft, U. Eitner, and S. Wiese, "Thermomechanical stress in solar cells: Contact pad modeling and reliability analysis," *Solar Energy Materials and Solar Cells*, vol. 196, pp. 167–177, 2019. DOI: 10.1016/j.solmat.2019.03.041.

[96] P. G. Ifju, "Composite materials," in *Springer Handbook of Experimental Solid Mechanics*, New York, USA: Springer, 2008, pp. 97–124.

[97] C. Hirschl, M. Granitzer, L. Neumaier, M. Spielberger, W. Mühleisen, M. Kraft, G. Kroupa, and J. Schicker, "Combined experimental and simulatory evaluation of thermal and mechanical loads on pv modules," in *Proceedings of the 27th European Photovoltaic Solar Energy Conference and Exhibition*, 2012, pp. 3561–3565. DOI: 10.4229/27thEUPVSEC2012-4BV.3.55.

[98] A. J. Beinert, M. Imm, J. Benick, F. Becker, S. Seitz, M. Heinrich, O. Paul, S. W. Glunz, J. Aktaa, U. Eitner, and H. Neuhaus, "Silicon solar cell-integrated stress and temperature sensors for photovoltaic modules," *Progress in Photovoltaics: Research and Applications*, pp. 717–724, 2020. DOI: 10.1002/pip.3263.

[99] S. P. Wong, W. Y. Cheung, N. Ke, M. R. Sajan, W. S. Guo, L. Huang, and S. Zhao, "IR photoelasticity study of stress distribution in silicon under thin film structures," *Materials Chemistry and Physics*, vol. 51, pp. 157–162, 1997. DOI: 10.1016/S0254-0584(97)80286-6.

[100] T. Zheng and S. Danyluk, "Study of stresses in thin silicon wafers with near-infraredphase stepping photoelasticity," *Journal of Materials Research*, vol. 17, pp. 36–42, 2002. DOI: 10.1557/JMR.2002.0008.

[101] A. S. Budiman, G. Illya, V. Handara, W. A. Caldwell, C. Bonelli, M. Kunz, N. Tamura, and D. Verstraeten, "Enabling thin silicon technologies for next generation c-si solar pv renewable energy systems using synchrotron x-ray microdiffraction as stress and crack mechanism probe," *Solar Energy Materials*

and Solar Cells, vol. 130, pp. 303–308, 2014. DOI: 10.1016/j.solmat.2014.07.029.

[102] S. K. Tippabhotla, I. Radchenko, W. Song, G. Illya, V. Handara, M. Kunz, N. Tamura, A. A. Tay, and A. S. Budiman, "From cells to laminate: Probing and modeling residual stress evolution in thin silicon photovoltaic modules using synchrotron x-ray micro-diffraction experiments and finite element simulations," *Progress in Photovoltaics: Research and Applications*, vol. 25, pp. 791–809, 2017. DOI: 10.1002/pip.2891.

[103] R. Loudon, "The raman effect in crystals," *Advances in Physics*, vol. 13, pp. 423–482, 1964. DOI: 10.1080/00018736400101051.

[104] W. Muehleisen, J. Schicker, L. Neumaier, C. Hirschl, N. Vollert, S. Seufzer, R. Battistutti, M. Pedevilla, J. Scheurer, M. Schwark, and T. Fischer, "Stress measurements in interconnected solar cells with raman spectroscopy," in *Proceedings of the 31st European Photovoltaic Solar Energy Conference and Exhibition*, 2015, pp. 160–163. DOI: 10.4229/EUPVSEC20152015-1BV.6.38.

[105] L. Neumaier, W. Mühleisen, T. Fischer, J. Scheurer, W. Pranger, and C. Hirschl, "Contact-free raman spectroscopic measurement of residual stress in silicon solar cells caused by stringing," in *Proceedings of the 32nd European Photovoltaic Solar Energy Conference and Exhibition*, 2016, pp. 123–126. DOI: 10.4229/EUPVSEC20162016-1BV.5.4.

[106] F. Hartmann and C. Katz, *Structural Analysis with Finite Elements*. Berlin / Heidelberg, Germany: Springer, 2007, ISBN: 3-540-49698-x.

[107] B. Klein, *FEM - Grundlagen und Anwendungen der Finite-Element-Methode im Maschinen- und Fahrzeugbau*, 9th ed. Wiesbaden, Germany: Springer Vieweg, 2012, ISBN: 978-3-8348-2134-8.

[108] M. Wagner, *Lineare und nichtlineare FEM: Eine Einführung mit Anwendungen in der Umformsimulation mit LS-DYNA*. Wiesbaden, Germany: Springer Vieweg, 2017, ISBN: 978-3-658-17865-9.

[109] L. Zhou and H.-M. Qu, "Mechanical research and development of a monocrystalline silicon neutron beam window for CSNS," *Chinese Physics C*, vol. 39, p. 5, 2015. DOI: 10.1088/1674-1137/39/9/096001.

[110] P. Rupnowski and B. Sopori, "Strength of silicon wafers: Fracture mechanics approach," *International Journal of Fracture*, vol. 155, pp. 67–74, 2009. DOI: 10.1007/s10704-009-9324-9.

[111] H. J. Möller, C. Funke, M. Rinio, and S. Scholz, "Multicrystalline silicon for solar cells," *Thin Solid Films*, vol. 487, pp. 179–187, 2005. DOI: 10.1016/j.tsf.2005.01.061.

[112] M. Abdelhamid, R. Singh, and M. Omar, "Review of microcrack detection techniques for silicon solar cells," *IEEE Journal of Photovoltaics*, vol. 4, pp. 514–524, 2014. DOI: 10.1109/JPHOTOV.2013.2285622.

[113] M. Koentges, I. Kunze, S. Kajari-Schroeder, X. Breitenmoser, and B. Bjørneklett, "The risk of power loss in crystalline silicon based photovoltaic modules due to micro-cracks," *Solar Energy Materials and Solar Cells*, vol. 95, pp. 1131–1137, 2011. DOI: 10.1016/j.solmat.2010.10.034.

[114] S. Kajari-Schroeder, I. Kunze, and M. Koentges, "Criticality of cracks in PV modules," *Energy Procedia*, vol. 27, pp. 658–663, 2012. DOI: 10.1016/j.egypro.2012.07.125.

[115] H. Wu, S. N. Melkote, and S. Danyluk, "Mechanical strength of silicon wafers cut by loose abrasive slurry and fixed abrasive diamond wire sawing," *Advanced Engineering Materials*, vol. 14, pp. 342–348, 2012. DOI: 10.1002/adem.201100263.

[116] S. Schoenfelder, A. Bohne, and J. Bagdahn, "Comparison of test methods for strength characterization of thin solar wafer," in *Proceedings of the 22nd European Photovolatic Solar Energy Conference and Exhibition*, 2007, pp. 1636–1640.

[117] M. Oswald, T. Loewenstein, O. Anspach, J. Hirsch, D. Lausch, and S. Schoenfelder, "On the correlation of surface roughness to mechanical strength and reflectivity of silicon wafers," in *Proceedings of the 29th European Photovoltaic Solar Energy Conference and Exhibition*, 2014, pp. 764–768. DOI: 10.4229/EUPVSEC20142014-2AV.1.38.

[118] F. Kaule, W. Wang, and S. Schoenfelder, "Modeling and testing the mechanical strength of solar cells," *Solar Energy Materials and Solar Cells*, vol. 120, pp. 441–447, 2014. DOI: 10.1016/j.solmat.2013.06.048.

[119] L. C. Rendler, J. Walter, T. Geipel, M. Volk, C. Ebert, and U. Eitner, "Modelling and verification of mechanical stress induced by soldering of wires for multi busbar interconnection," in *Proceedings of the 31st European Photovoltaic Solar Energy Conference and Exhibition*, 2015, pp. 84–88. DOI: 10.4229/EUPVSEC20152015-1CO.11.2.

[120] L. C. Rendler, A. Kraft, C. Ebert, U. Eitner, and S. Wiese, "Mechanical stress in solar cells with multi busbar interconnection - parameter study by FEM simulation," in *Proceedings of the 17th IEEE International Conference on Thermal, Mechanical and Multi-Physics Simulation and Experiments in Microelectronics and Microsystems*, 2016, p. 5. DOI: 10.1109/EuroSimE.2016.7463325.

[121] L. C. Rendler, A. Kraft, C. Ebert, S. Wiese, and U. Eitner, "Investigation of thermomechanical stress in solar cells with multi busbar interconnection by finite element modeling," in *Proceedings of the 32nd European Photovoltaic Solar Energy Conference and Exhibition*, 2016, pp. 94–98. DOI: 10.4229/EUPVSEC20162016-1CO.11.2.

[122] B. Kang, N. Park, S. J. Tark, W. W. Oh, S. Park, Y. D. Kim, H.-S. Lee, and D. Kim, "Advanced yield strength of interconnector ribbon for photovoltaic module using crystallographic texture control," *Metals and Materials International*, vol. 20, pp. 229–232, 2014. DOI: 10.1007/s12540-014-2005-x.

[123] H. Wirth, M. Tranitz, C. Malchow, and F. Clement, "New technologies for back contact module assembly," in *Proceedings of the 25th European Photovoltaic Solar Energy Conference and Exhibition/5th World Conference on Energy Conversion*, 2010, pp. 3846–3849. DOI: 10.4229/25thEUPVSEC2010-4CO.19.3.

[124] O. Storbeck and H. Hahn, "Tabbing ribbon, photovoltaic solar panel, method for manufacturing a solar cell tabbing ribbon," European Patent Application 2466648 A1, 2011.

[125] H. J. Krokoszinski and T. Amorim, "Solarzellenanordnung und Verfahren zu deren Herstellung," German Patent Application 102011078371, 2013.

[126] H. Wehr, "Vorrichtung zum Biegen eines Metallbandes," German Patent 19915488, 2000.

[127] *Metallic materials – tensile testing – part 1: Method of test at room temperature: EN ISO 6892-1*, 2017.

[128] J. Rösler, H. Harders, and M. Bäker, *Mechanisches Verhalten der Werkstoffe*, 4th ed. Wiesbaden, Germany: Springer, 2012, ISBN: 978-3-8348-1818-8.

[129] C. Kohn, T. Faber, R. Kübler, J. Beinert, G. Kleer, F. Clement, D. Erath, I. Reis, F. Martin, and A. Müller, "Analyses of warpage effects induced by passivation and electrode coatings in silicon solar cells," in *Proceedings of the 22nd European Photovoltaic Solar Energy Conference and Exhibition*, 2007, pp. 1270–1273. DOI: 10.1016/j.applthermaleng.2013.02.028.

[130] Qian Zhang, "Isothermal mechanical and thermomechanical durability characterization of selected Pb-free solders," Ph.D. dissertation, University of Maryland, College Park, MD, USA, 2004.

[131] M. A. Hopcroft, W. D. Nix, and T. W. Kenny, "What is the young's modulus of silicon?" *Journal of Microelectromechanical Systems*, vol. 19, pp. 229–238, 2010. DOI: 10.1109/JMEMS.2009.2039697.

[132] L. C. Rendler, J. Walter, A. Kraft, C. Ebert, S. Wiese, and U. Eitner, "Ultrasoft wires for direct soldering on finger grids of solar cells," *Energy Procedia*, vol. 124, pp. 478–483, 2017. DOI: 10.1016/j.egypro.2017.09.284.

[133] L. C. Rendler, J. Walter, S. Goldenberg, A. J. Beinert, S. Wiese, and U. Eitner, "Mechanical and electrical properties of wave-shaped wires for low-stress interconnection of solar cells," *Solar Energy Materials and Solar Cells*, vol. 176, pp. 204–211, 2018. DOI: 10.1016/j.solmat.2017.11.022.

[134] George Vander Voort, *Table i - selected tint etchants*, 1985, Accessed: March 02, 2020. [Online]. Available: http://www.metallography.com/etching/table.htm.

[135] L. C. Rendler, A. P. Haryantho, J. Walter, J. Huyeng, A. Kraft, S. Wiese, and U. Eitner, "Wave-shaped wires soldered on the finger grid of solar cells: Solder joint stability under thermal cycling," *AIP Conference Proceedings*, vol. 1999, p. 8, 2018. DOI: 10.1063/1.5049303.

[136] L. C. Rendler, "Processing device and method for forming connection conductors for semiconductor components," World Patent Application 2018/178292, 2018.

[137] C. H. Schiller, L. C. Rendler, D. Eberlein, G. Mülhöfer, A. Kraft, and D. H. Neuhaus, "Accelerated tc test in comparison with standard tc test for pv modules with ribbon, wire and shingle interconnection," in *Proceedings of the 36th European Photovoltaic Solar Energy Conference and Exhibition*, 2019, pp. 995–999. DOI: 10.4229/EUPVSEC20192019-4AV.1.8.

[138] I. Hädrich, U. Eitner, M. Wiese, and H. Wirth, "Unified methodology for determining CTM ratios: Systematic prediction of module power," *Solar Energy Materials and Solar Cells*, vol. 131, pp. 14–23, 2014. DOI: 10.1016/j.solmat.2014.06.025.

[139] M. Mittag and M. Ebert, "Systematic PV module optimization with the cell-to-module (CTM) analysis software," *Photovoltaics International*, vol. 36, p. 6, 2017.

List of publications

First author

- L. C. Rendler, J. Walter, T. Geipel, M. Volk, C. Ebert, and U. Eitner, "Modelling and verification of mechanical stress induced by soldering of wires for multi busbar interconnection," in *Proceedings of the 31st European Photovoltaic Solar Energy Conference and Exhibition*, 2015, pp. 84–88. DOI: 10.4229/EUPVSEC20152015-1CO.11.2.
- L. C. Rendler, A. Kraft, C. Ebert, U. Eitner, S. Wiese, "Mechanical stress in solar cells with multi busbar interconnection - Parameter study by FEM simulation," in *Proceedings of the 17th IEEE International Conference on Thermal, Mechanical and Multi-Physics Simulation and Experiments in Microelectronics and Microsystems*, 2016, p. 5. DOI: 10.1109/EuroSimE.2016.7463325.
- L. C. Rendler, A. Kraft, C. Ebert, S. Wiese, and U. Eitner, "Investigation of thermomechanical stress in solar cells with multi busbar interconnection by finite element modeling," in *Proceedings of the 32nd European Photovoltaic Solar Energy Conference and Exhibition*, 2016, pp. 94–98. DOI: 10.4229/EUPVSEC20162016-1CO.11.2.
- L. C. Rendler, J. Walter, A. Kraft, C. Ebert, S. Wiese, and U. Eitner, "Ultrasoft wires for direct soldering on finger grids of solar cells," *Energy Procedia*, vol. 124, pp. 478–483, 2017. DOI: 10.1016/j.egypro.2017.09.284.
- L. C. Rendler, "Processing device and method for forming connection conductors for semiconductor components," World Patent Application 2018/178292, 2018.
- L. C. Rendler, A. P. Haryantho, J. Walter, J. Huyeng, A. Kraft, S. Wiese, and U. Eitner, "Wave-shaped wires soldered on the finger grid of solar cells: Solder joint stability under thermal cycling," *AIP Conference Proceedings*, vol. 1999, p. 8, 2018. DOI: 10.1063/1.5049303.
- L. C. Rendler, J. Walter, S. Goldenberg, A. J. Beinert, S. Wiese, and U. Eitner, "Mechanical and electrical properties of wave-shaped wires for

low-stress interconnection of solar cells," *Solar Energy Materials and Solar Cells*, vol. 176, pp. 204–211, 2018. DOI: 10.1016/j.solmat.2017.11.022.

- L. C. Rendler, P. Romer, A. J. Beinert, J. Walter, S. Stecklum, A. Kraft, U. Eitner, and S. Wiese, "Thermomechanical stress in solar cells: Contact pad modeling and reliability analysis," *Solar Energy Materials and Solar Cells*, vol. 196, pp. 167–177, 2019. DOI: 10.1016/j.solmat.2019.03.041.
- L. C. Rendler, M. Mittag, D. H. Neuhaus, "Solarzellenmodul," German Patent Application 102020128080.7, 2020.

Co-author

- A. Moser, L. C. Rendler, M. Kratschmer, and P. Woias, "Transient model for thermoelectric generator systems harvesting from the natural ambient temperature cycle," in *Proceedings Power MEMS*, 2010, pp. 431-434.
- U. Eitner and L. C. Rendler, "The mechanical theory behind the peel test," *Energy Procedia*, vol. 55, pp. 331–335, 2014. DOI: 10.1016/j.egypro.2014.08.096.
- U. Eitner and L. C. Rendler, "Peel testing of ribbons on solar cells at different angles: Consistent comparison by using adhesive fracture energies," in *Proceedings of the 29th European Photovoltaic Solar Energy Conference and Exhibition*, 2014, pp. 3406–3408. DOI: 10.4229/EUPVSEC20142014-5DV.3.40.
- T. Geipel, L. C. Rendler, M. Stompe, U. Eitner, and L. Rissing, "Reduction of thermomechanical stress using electrically conductive adhesives," *Energy Procedia*, vol. 77, pp. 346–355, 2015. DOI: 10.1016/j.egypro.2015.07.049.
- U. Eitner and L. C. Rendler, "The impact of ribbon properties on measured peel forces," *Energy Procedia*, vol. 92, pp. 500–504, 2016. DOI: 10.1016/j.egypro.2016.07.133.
- M. Mittag, A. J. Beinert, L. C. Rendler, M. Ebert, and U. Eitner, "Triangular ribbons for improved module efficiency," in *Proceedings of the 32nd European Photovoltaic Solar Energy Conference and Exhibition*, 2016, pp. 169–172. DOI: 10.4229/EUPVSEC20162016-1BV.5.32.
- J. Walter, L. C. Rendler, C. Ebert, A. Kraft, and U. Eitner, "Solder joint stability study of wire-based interconnection compared to ribbon interconnection," *Energy Procedia*, vol. 124, pp. 515–525, 2017. DOI: 10.1016/j.egypro.2017.09.288.

- J. Walter, L. C. Rendler, A. Halm, V. Mihailetchi, A. Kraft, and U. Eitner, "Ribbon interconnection of 6" BC-BJ solar cells," *Energy Procedia*, vol. 124, pp. 504–514, 2017. DOI: 10.1016/j.egypro.2017.09.287.
- J. D. Huyeng, A. Spribille, L. C. Rendler, C. Ebert, U. Eitner, and R. Keding, "Influence of interconnection concepts for IBC solar cell performance by simulation," *AIP Conference Proceedings*, vol. 1999, p. 6, 2018. DOI: 10.1063/1.5049250.
- A. Spribille, J. Huyeng, L. C. Rendler, "Zuverlässig verschaltbare Rückkontaktsolarzelle ohne isolierende Schichten," German Patent Application 102019122222.2, 2019.
- A. J. Beinert, A. Büchler, P. Romer, V. Haueisen, L. C. Rendler, M. C. Schubert, M. Heinrich, J. Aktaa, and U. Eitner, "Enabling the measurement of thermomechanical stress in solar cells and PV modules by confocal micro-Raman spectroscopy," *Solar Energy Materials and Solar Cells*, vol. 193, pp. 351–360, 2019. DOI: 10.1016/j.solmat.2019.01.028.
- A. Spribille, J. D. Huyeng, T. Schweigstill, I. Franzetti, L. C. Rendler, and F. Clement, "Electrode Design for Wire Interconnected Back Contact Solar Cells," in *Proceedings of the 36th European Photovoltaic Solar Energy Conference and Exhibition*, 2019, pp. 196–200. DOI: 10.4229/EUPVSEC20192019-2BO.4.2.
- C. H. Schiller, L. C. Rendler, D. Eberlein, G. Mülhöfer, A. Kraft, and D. H. Neuhaus, "Accelerated TC test in comparison with standard TC test for PV modules with ribbon, wire and shingle interconnection," in *Proceedings of the 36th European Photovoltaic Solar Energy Conference and Exhibition*, 2019, pp. 995–999. DOI: 10.4229/EUPVSEC20192019-4AV.1.8.

Curriculum Vitae

Personal information

Name:	Li Carlos Rendler
Date of birth:	1984-09-30
Place of birth:	Friesenheim-Schuttern, Germany

Academic and professional background

2013 – 2022	Scientist and PhD student Fraunhofer ISE, Freiburg, Germany
2012	Embedded system developer Reputation-Engineering, Wörth/Wifling, Germany
2011	External employee University of Freiburg, Germany
2010	University degree: Dipl.-Ing. Thesis on thermoelectrical energy harvesting in tunnels University of Freiburg, Germany
2008 – 2009	Internship Sulfurcell (later Soltecture), Berlin, Germany
2004 – 2010	Study of microsystems engineering University of Freiburg, Germany

Appendix

A.1 Simulation details

A.1.0.1 Geometries and mesh

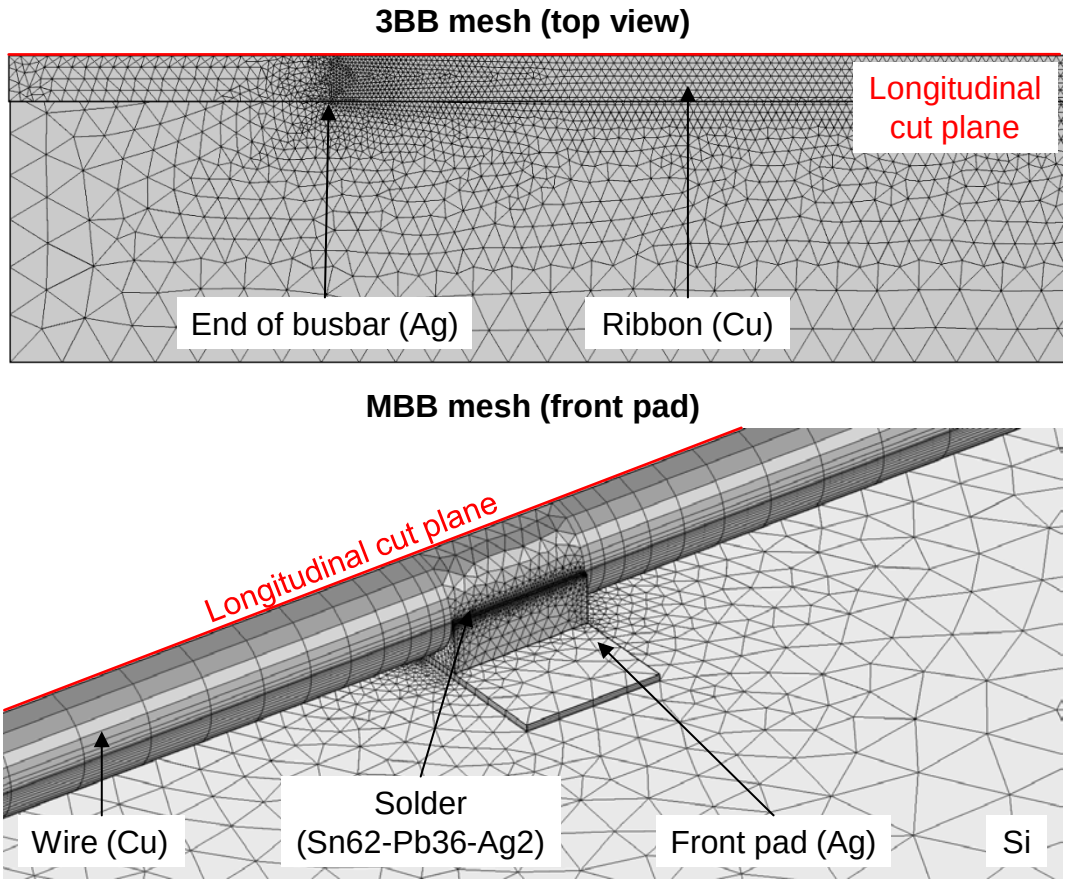

Figure A.1: Geometry detail and meshes used for Simulation I (3BB solar cell) and Simulation III (MBB solar cell) described in Section 3.2 [121].

In Section 3.2 the geometry for Simulation II (3BB solar cell) and Simulation III (MBB solar cell) is shown (see Figure 3.1). The main important areas of the used meshes for both simulations, the end of a busbar (Simulation II) and one contact

pad (Simulation III), are shown by Figure A.1 [121]. Furthermore, Figure A.2 shows the three configurations as described in Section 3.3.4, as well as the ignored mesh elements for Simulation IV where singularities are expected [95].

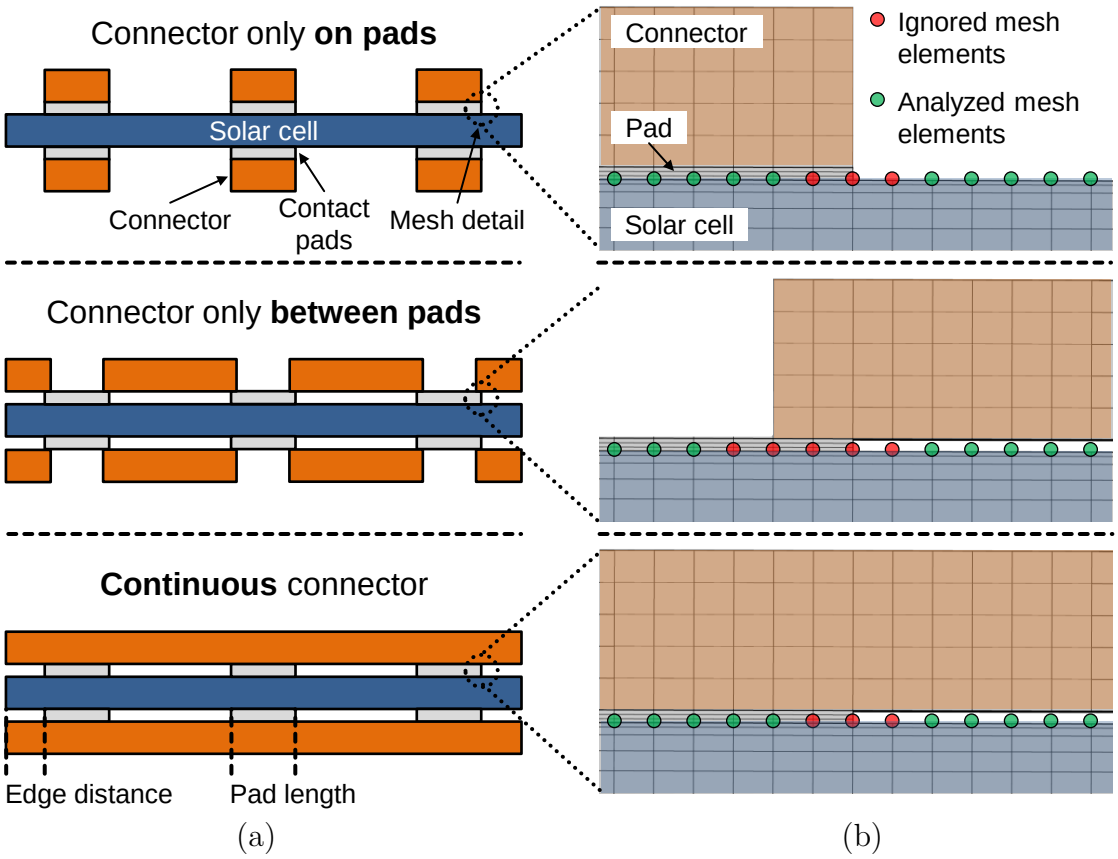

Figure A.2: (a) Schematic drawing of the different contact configurations analyzed by Simulation IV and (b) for each configuration the ignored mesh elements [95].

A.1.0.2 Additional results of Simulation IV

In the following, additional diagrams showing thermomechanical stress (transversal and longitudinal) after soldering calculated by Simulation IV (see Section 3.3.4) are shown. Figure A.3 shows the transversal and longitudinal stress on the silicon surface for contact pads with a length of 9 mm (2 mm pads shown by Figure 3.6) for the three different contact configurations (see Figure 3.5) [95].

Thermomechanical stress in pad rows with constant pad center positions, but different pad sizes (pad length of 0.4 mm, 2 mm, and 9 mm, as well as for continuous busbar) connected by continuous interconnectors (continuous configuration) is shown by Figure A.4. Figure A.5 indicates thermomechanical stress for different pad sizes (between 2 mm and 23 mm) and constant edge distance (different pad positions). In addition, the thermomechanical stress for different pad distances and numbers per pad row (6, 12, and 50 pads, as well as for a continuous busbar) are shown by Figure A.6 [95].

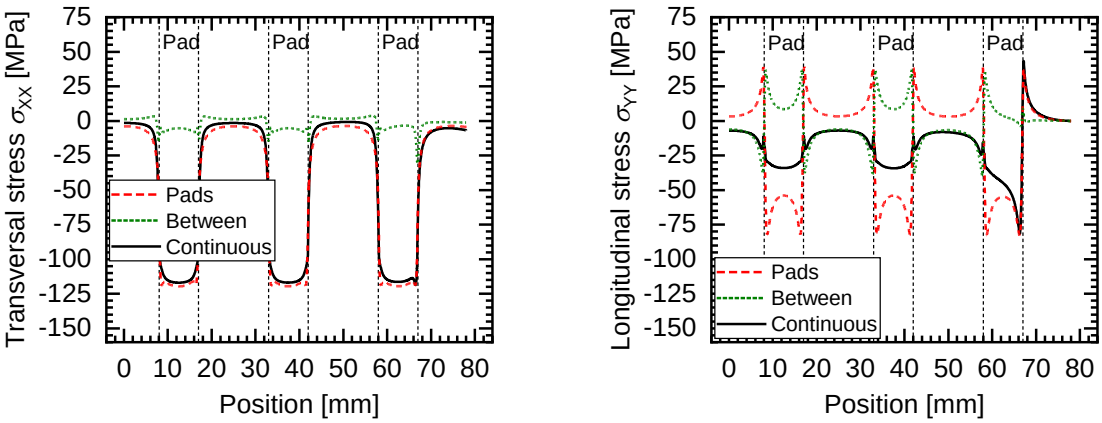

Figure A.3: Comparison of the thermomechanical stress in a silicon solar cell for different contact configurations: on pads only (Pads), in between pads (Between) and for continuous interconnectors (Continuous). For a pad length of 9 mm (a) the transversal stress σ_{XX} and (b) the longitudinal stress σ_{YY} on the silicon solar cell surface under half of a pad row are shown [95].

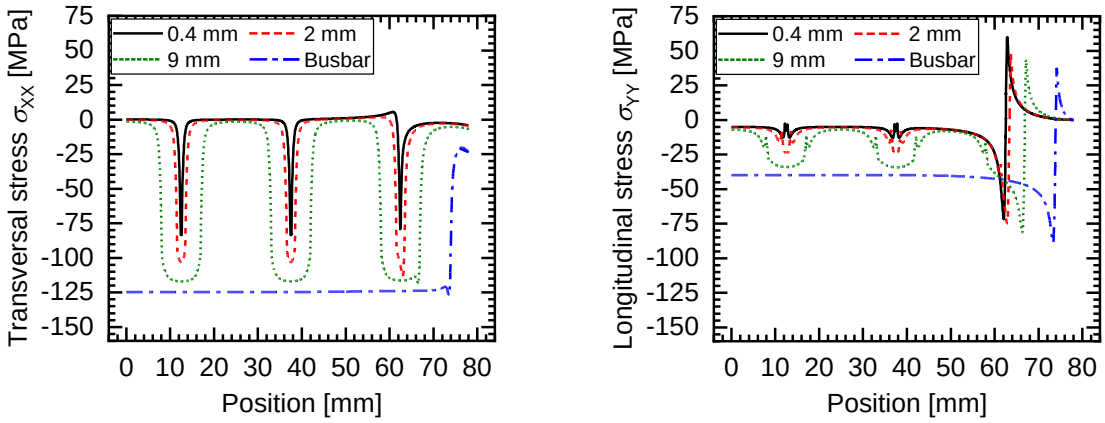

Figure A.4: Comparison of the thermomechanical stress for solar cells with pad rows with different pad length and constant pad center positions connected by continuous interconnectors: (a) the transversal stress σ_{XX} and (b) the longitudinal stress σ_{YY} on the silicon solar cell surface under half of a pad row for pad length between 0.4 mm and 9 mm, as well as for a continuous busbar are shown [95].

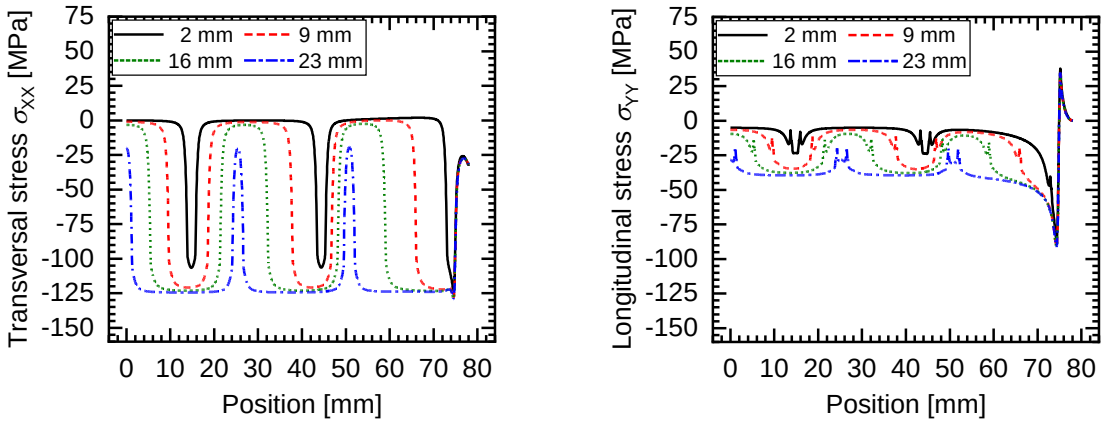

Figure A.5: Comparison of the thermomechanical stress for solar cells with different pad lengths and constant distance of the outermost contact to the cell edge connected by continuous interconnectors: (a) the transversal stress σ_{XX} and (b) the longitudinal stress σ_{YY} on the silicon solar cell surface under half of a pad row for pad length between 2 mm and 23 mm, as well as for a continuous busbar are shown [95].

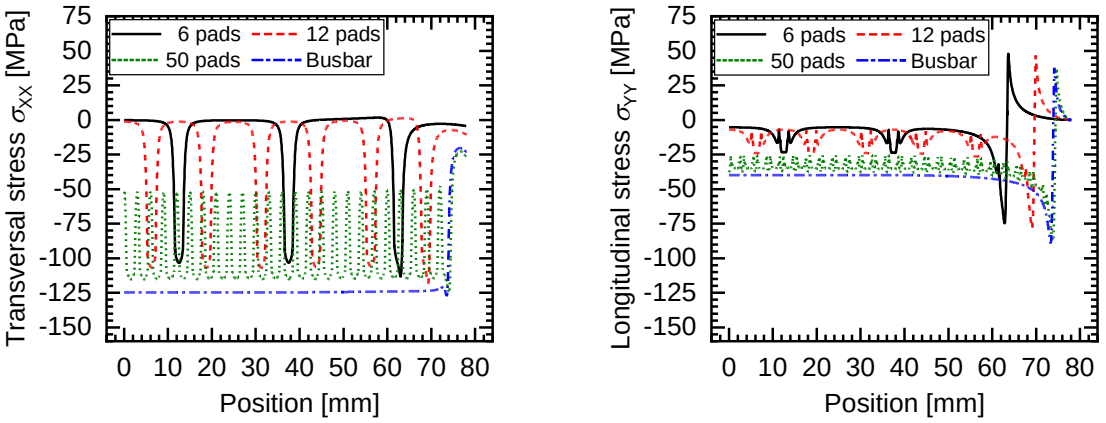

Figure A.6: Comparison of the thermomechanical stress for different pad distances and numbers (6, 12, and 50 pads per row): (a) transversal stress σ_{XX} and (b) the longitudinal stress σ_{YY} on the silicon solar cell surface under half of a pad row connected by a continuous interconnector [95].

A.2 Matlab code for yield limit or pseudo yield limit detection

In this section the code of the MATLAB-based software tool to automatically determine the pseudo yield limit of wave-shaped wires in Section 5.2 is included.

```
1  %% Initialize script
2  clear();
3  close all;
4
5  %% Initialize result file
6  results = {'filename', 'x_F0.2/Rp0.2[%]', 'F0.2/Rp0.2[N or ...
       MPa]', 'x_F0.315/sigma0.315[%]', 'F0.315/sigma0.315[N or MPa]'};
7  mean1 = 0;
8  mean2 = 0;
9
10 %% load txt-files in the folder
11 data = dir('*.TXT');
```

```
12
13 %% Initialize result folder
14 FolderTarget = pwd;
15 MyDate = datestr(now,'yymmdd');
16 MyTime = datestr(now,'HHMMSS');
17
18 if  exist('results','dir')==7
19     mkdir([FolderTarget '\' 'results'], [MyDate '_' MyTime])
20 else
21     mkdir(FolderTarget, 'results')
22     mkdir([FolderTarget '\' 'results'], [MyDate '_' MyTime])
23 end
24
25 %% Loop through data files
26 for i = 1:length(data)
27     %% import data
28     filename = data(i).name;
29     [fid] = fopen(filename, 'rt'); %open txt file of interest
30     startRow = 9; %start at line 9 to read data (without 8 ...
           header lines)
31     formatSpec = '%21s%s%[^\n\r]';
32     dataArray = textscan(fid, formatSpec, 'Delimiter', '', ...
           'WhiteSpace', '', 'HeaderLines' ,startRow-1, ...
           'ReturnOnError', false);
33
34     %% Allocate imported array to column variable names
35     strain = str2double(dataArray{:,1});
36     stress = str2double(dataArray{:,2});
37
38     %% F0.2 DETECTION %%
39
40     %% first derivation
41     df1 = diff(stress)./diff(strain); %y-data of derivation
42     xd1 = strain(2:length(strain)); %x-data of derivation
43     df1(df1==Inf)=0; %overwrite Inf
44     df1(df1==-Inf)=0; %overwrite -Inf
45
46     %moving average filter smoothing of the first derivation
```

```
47      smoothpoints = 35; %number of smoothpoints (between 25-50 ...
           should be fine)
48      smooth = ones(1, smoothpoints)/smoothpoints;
49      avg_df1 = filter(smooth, 1, df1); %y-data of smoothed derivation
50      [max_value, max_index] = max(avg_df1); %find the maximum of ...
           the smoothed derivation
51
52      %determine polynomial fitting area
53      det_coeff = 0; %initialize determination coefficient
54      fit_points = 1000; %start number of data points adjacent to ...
           maximum of derivation
55      target_det = 0.999; %target value for determination coefficient
56      dec_num = 2;
57
58      %decrease area until determination coefficient reaches ...
           target value
59      while det_coeff < target_det
60
61          %find index values of the fit area
62          A=[];
63          for k=(max_index-(fit_points/2)):(max_index+(fit_points/2))
64             if k>0
65                 A=[A,k];
66             end
67          end
68          strain_fit = strain(A); %x-values for fitting
69          stress_fit = stress(A); %y-values for fitting
70
71          %polynomial fitting: line
72          fit_coeff = polyfit(strain_fit, stress_fit, 1);
73          fit_curve = polyval(fit_coeff, strain_fit);
74
75          %calculate coefficient of determination
76          sumStrain = sum(strain_fit);
77          sumStrain2 = sum(strain_fit.^2);
78          sumStress = sum(stress_fit);
79          sumStress2 = sum(stress_fit.^2);
80          sizeStrain = size(strain_fit,1);
81          mulSS = sum(strain_fit.*stress_fit);
```

```
82          corr_coeff = (mulSS-(1/sizeStrain)*sumStrain*sumStress)...
83              /sqrt((sumStrain2-(1/sizeStrain)*sumStrain^2)*...
84              (sumStress2-(1/sizeStrain)*sumStress^2));
85          det_coeff = corr_coeff^2;
86
87          %decrease number of fit values
88          fit_points = fit_points-dec_num;
89
90      end
91
92      %x-axis crossing
93      x_fit_zero = -fit_coeff(2)/fit_coeff(1);
94      x_fit = [0:0.001:5];
95      y_fit = fit_coeff(1)*x_fit+fit_coeff(2);
96
97
98      %shift of fitting line
99      strain_fit_shift = strain_fit + 0.2;
100     fit_coeff_shift = polyfit(strain_fit_shift, stress_fit, 1);
101     fit_curve_shift = polyval(fit_coeff_shift, strain_fit_shift);
102
103     x_rp02 = [0:0.001:5];
104     y_rp02 = fit_coeff_shift(1)*x_rp02+fit_coeff_shift(2);
105
106     %find the intersection value - bad mode
107     diff_bad =(fit_coeff_shift(1)*strain+fit_coeff_shift(2))-stress;
108     abs_diff_bad = abs(diff_bad);
109     [y_bad_intersect, x_bad_intersect]  = min(abs_diff_bad);
110
111     %find the intersection value - good mode (approximization)
112     if diff_bad(x_bad_intersect)>0
113
114         x1 = strain(x_bad_intersect-1);
115         y1 = stress(x_bad_intersect-1);
116         x2 = strain(x_bad_intersect);
117         y2 = stress(x_bad_intersect);
118
119         %x and y values of approximization array
120         x_approx = [x1:((x2-x1)/1000):x2];
```

```
121         y_approx = ((y2-y1)/(x2-x1))*(x_approx-x1)+y1;
122
123         abs_diff_good = ...
               abs((fit_coeff_shift(1)*x_approx+fit_coeff_shift(2))...
124             -y_approx);
125         [y_good_intersect, x_good_intersect] = min(abs_diff_good);
126
127     else
128         x1 = strain(x_bad_intersect);
129         y1 = stress(x_bad_intersect);
130         x2 = strain(x_bad_intersect+1);
131         y2 = stress(x_bad_intersect+1);
132
133         %x and y values of approximization array
134         x_approx = [x1:((x2-x1)/1000):x2];
135         y_approx = ((y2-y1)/(x2-x1))*(x_approx-x1)+y1;
136
137
138         abs_diff_good = ...
               abs((fit_coeff_shift(1)*x_approx+fit_coeff_shift(2))...
139             -y_approx);
140         [y_good_intersect, x_good_intersect]  = min(abs_diff_good);
141     end
142
143     %%%SIGMA(0.315%STRAIN)DETECTION%%%
144
145     strain_val = 0.315;
146     strain_new = strain-x_fit_zero;
147
148     if strain_new(min(A)) < strain_val
149
150         [y_s0315_bad, xind_s0315_bad]  = ...
               min(abs(strain_new-strain_val));
151
152         diff_bad2 = stress(xind_s0315_bad)-y_s0315_bad;
153
154         if diff_bad2 > 0
155
156             x1 = strain_new(xind_s0315_bad);
```

```
157             y1 = stress(xind_s0315_bad);
158             x2 = strain_new(xind_s0315_bad+1);
159             y2 = stress(xind_s0315_bad+1);
160 
161             %x and y values of approximization array
162             x_approx2 = [x1:((x2-x1)/1000):x2];
163             y_approx2 = ((y2-y1)/(x2-x1))*(x_approx2-x1)+y1;
164 
165             [dumb, indx_s0315]  = min(abs(x_approx2-strain_val));
166             x_s0315 = x_approx2(indx_s0315);
167             y_s0315 = y_approx2(indx_s0315);
168 
169         elseif diff_bad2 < 0
170 
171             x1 = strain_new(xind_s0315_bad-1);
172             y1 = stress(xind_s0315_bad-1);
173             x2 = strain_new(xind_s0315_bad);
174             y2 = stress(xind_s0315_bad);
175 
176             %x and y values of approximization array
177             x_approx2 = [x1:((x2-x1)/1000):x2];
178             y_approx2 = ((y2-y1)/(x2-x1))*(x_approx2-x1)+y1;
179 
180             [dumb, indx_s0315]  = min(abs(x_approx2-strain_val));
181             x_s0315 = x_approx2(indx_s0315);
182             y_s0315 = y_s0315;
183 
184             %results
185 
186         end
187 
188     else
189         x_s0315 = strain_val;
190         y_s0315 = fit_coeff_shift(1)*(strain_val);
191     end
192 
193     fclose(fid);
194 
195     results{i+1,1} = filename;
```

```
196     results{i+1,2} = ...
            num2str(x_approx(x_good_intersect)-x_fit_zero,'%.6f');
197     results{i+1,3} = num2str(y_approx(x_good_intersect),'%.6f');
198     results{i+1,4} = num2str(x_s0315,'%.6f');
199     results{i+1,5} = num2str(y_s0315,'%.6f');
200
201     mean1 = mean1 + y_approx(x_good_intersect);
202     mean2 = mean2 + y_s0315;
203
204     %% Save shifted curve
205
206     fid = fopen([FolderTarget '\' 'results' '\' MyDate '_' ...
            MyTime '\' filename(1:end-4) '_' 'results.txt'],'w');
207     formatSpec = '%s\t%s\r\n';
208
209     new_stress_strain = horzcat(strain_new, stress);
210     [nrows,ncols] = size(new_stress_strain);
211     for row = 1:nrows
212         fprintf(fid,formatSpec,new_stress_strain(row,:));
213     end
214     fclose(fid);
215
216     %% Plot curves
217     figure;
218     plot(strain_new, stress, 'k'); hold on;
219     plot((x_approx(x_good_intersect)-x_fit_zero),...
220         (y_approx(x_good_intersect)), 'xr','MarkerSize', 16, ...
                'linewidth', 2);
221     plot(x_s0315, y_s0315, '+b','MarkerSize', 16, 'linewidth', 2);
222
223     x_fit_line = [0:0.1:5];
224     y_fit_line = fit_coeff(1).*x_fit_line+fit_coeff(2);
225     plot(x_fit_line-x_fit_zero,y_fit_line,'-r');
226
227     fid2 = [FolderTarget '\' 'results' '\' MyDate '_' MyTime '\' ...
            filename(1:end-4) '_' 'figure.png'];
228     saveas(gcf, fid2, 'png')
229
230 end
```

```
231
232 %% Save Data
233
234 r_size = size(results,1);
235
236 mean1 = mean1/(size(results,1)-1);
237 mean2 = mean2/(size(results,1)-1);
238
239 results{r_size+1,1} = 'mean value';
240 results{r_size+1,2} = '-';
241 results{r_size+1,3} = num2str(mean1,'%.6f');
242 results{r_size+1,4} = '-';
243 results{r_size+1,5} = num2str(mean2,'%.6f');
244
245 fid = fopen([FolderTarget '\' 'results' '\' MyDate '_' MyTime ...
       '\' 'results.txt'],'w');
246 formatSpec = '%s\t%s\t%s\t%s\t%s\r\n';
247
248 [nrows,ncols] = size(results);
249 for row = 1:nrows
250     fprintf(fid,formatSpec,results{row,:});
251 end
252
253 fclose(fid);
254
255 hold off;
```

A.3 LabView software for the tool using wave-shaping Method 4

By Figure A.7 the working principle of wave-shaping machine using Method 4 (described in Section 5.1.4) is explained in detail showing the individual steps of the process in a schematic drawing.

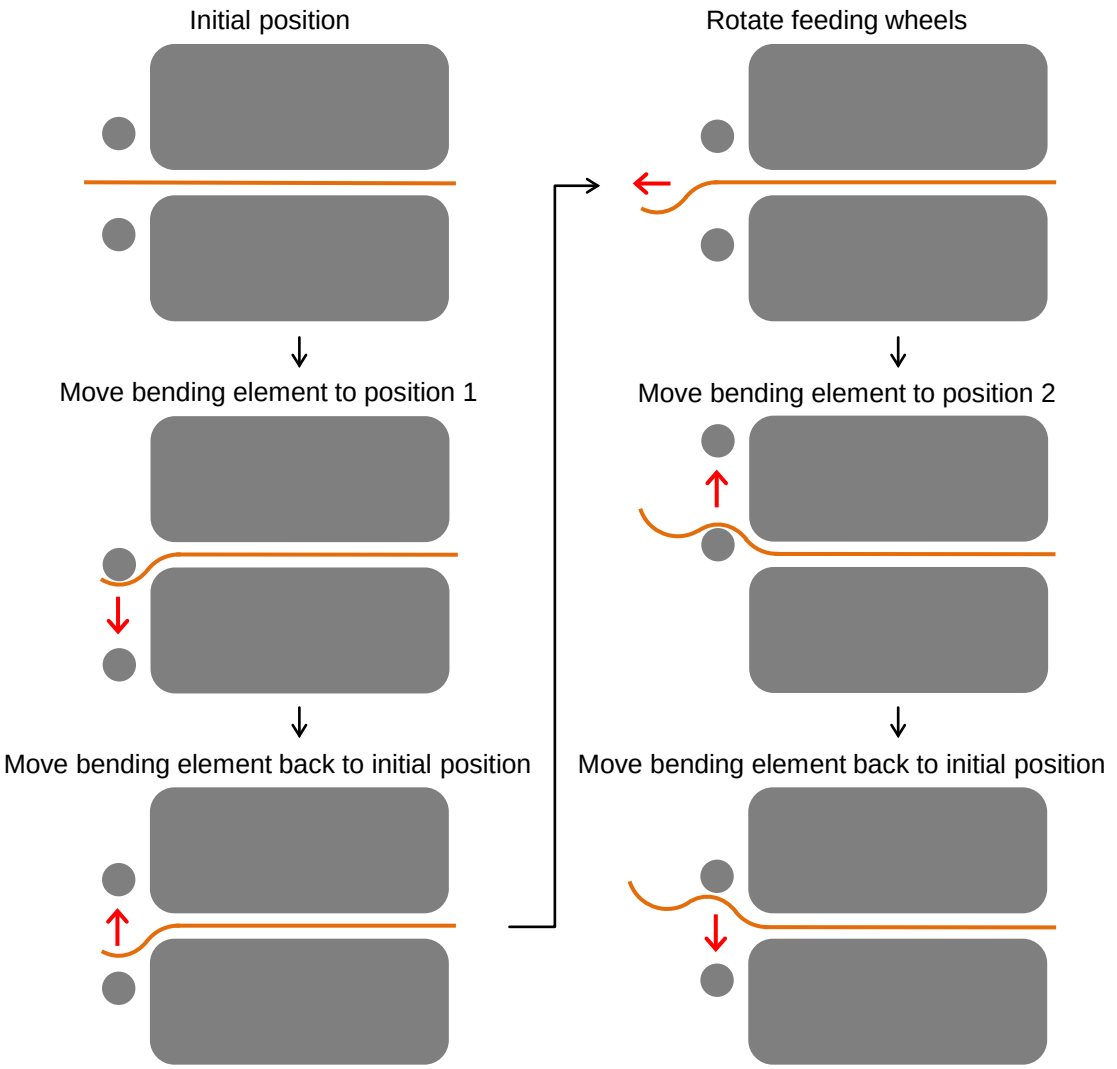

Figure A.7: Schematic drawing of the deformation sequence when using Method 4. The wire channel and the bending elements (both in gray), as well as the copper wire (orange) are shown. The red arrows indicate the movement of the bending elements for each step of the sequence.

Figure A.8 shows the most important steps of the LabView software which controls the electrical parts of the wave-shaping machine using Method 4 (see Section 5.1.4 and Figure 5.13).

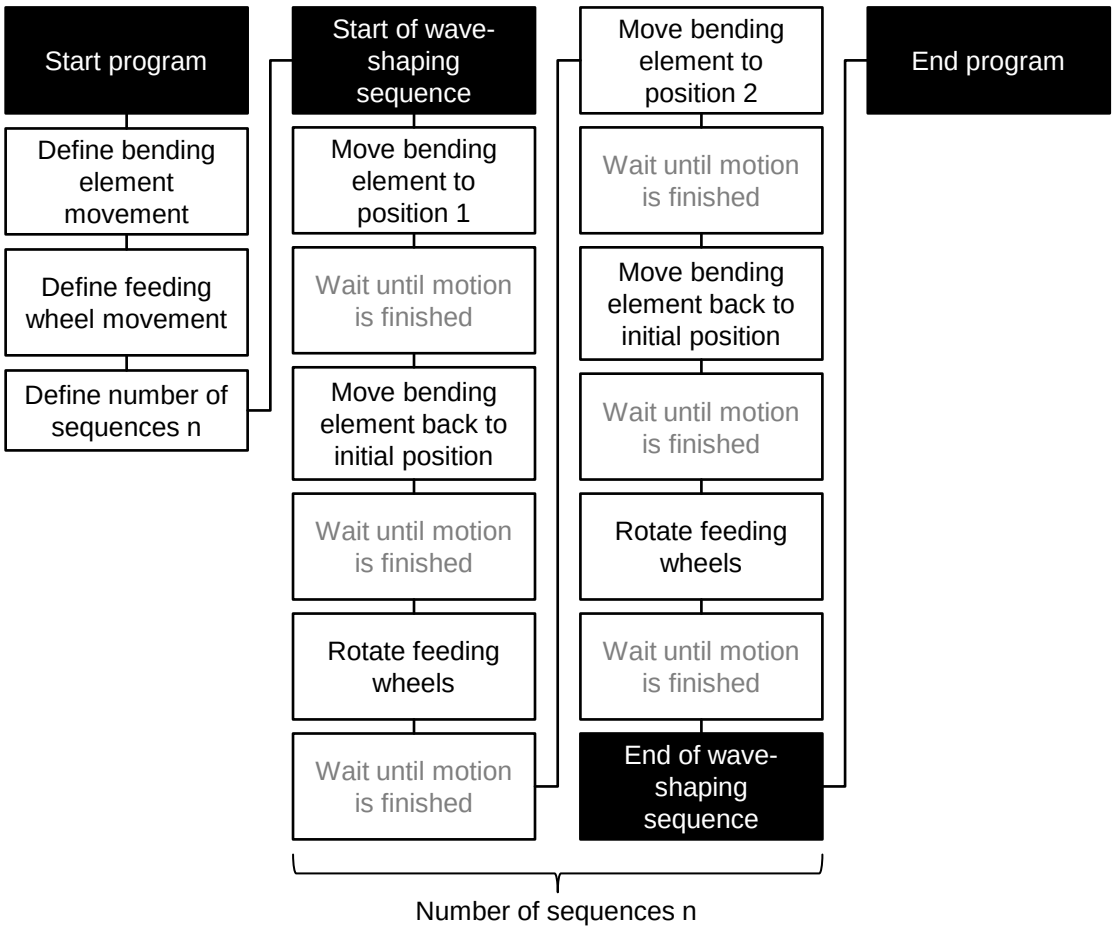

Figure A.8: Process diagramm of the operating principle of the developed LabView software to control the feeding wheel (rotated by electrical motor) and the bending elements (mounted on electrical axis). First, the movement of the bending elements and the feeding wheels defines the resulting shape of the wire (amplitude and period). Subsequently, the number of sequences defines the length of the resulting wave-shaped wire.